THE CATHOLIC UNIVERSITY OF AMERICA

Modeling Solar Flare Hard X-ray Images and Spectra Observed with RHESSI

A DISSERTATION

Submitted to the Faculty of the

Department of Physics

School of Arts and Sciences

Of The Catholic University of America

In Partial Fulfillment of the Requirements

For the Degree

Doctor of Philosophy

by

Linhui Sui

Washington, D.C.

2005

Abstract

Observations obtained with the Reuven Ramaty High Energy Solar Spectroscopic Imager (RHESSI) of a flare on February 20, 2002 indicate a hard X-ray (HXR) coronal source at or near the top of a flare loop (called a HXR looptop source). The existence of the HXR looptop source suggests that magnetic reconnection, which is believed to power flares, occurs above the loop. In order to explain this HXR looptop source, I created a steady-state particle transport model, in which high-energy electrons are continuously injected at the top of a semicircular flare loop. Based on the simulation results, I find that the model predictions are consistent with the RHESSI observations in many respects, but the spectrum of the looptop source obtained from the model is steeper than that from the RHESSI data. This suggests that, instead of being accelerated above the loop as generally believed, the particles might be accelerated in the looptop itself.

RHESSI observations of three other homologous flares that occurred between April 14 and 16, 2002, provide strong evidence for the presence of a large-scale current sheet above a flare loop, which is the basis of standard flare models. The most convincing finding is the presence of the temperature distribution of a separate coronal source above the flare loops: the hotter part of the coronal source was located lower in altitude than the cooler part. Together with the fact that the hotter flare loops are higher than the cooler loops, the observations support the existence of a large-scale current sheet between the top of the flare loops and the coronal source above. Blob-like sources along a line above the loop in the decay phase of the April 15, 2002, flare, which are suggestive of magnetic islands initiated by the tearing-mode instability, and the observation of a cusp structure in microwaves, further support the presence of the current sheet.

The observations of the three homologous flares reveal two other features which are beyond the predictions of the standard flare models: the downward motion of flare loops in the early impulsive phase of each flare, and an initially stationary coronal source above the loops. These features are believed to be related to the formation and development of a current sheet. In particular, the downward loop motion seems to be a common phenomenon in flares, suggesting the necessity for modifications to the existing standard flare models.

Finally, thanks to the broad energy coverage of the RHESSI spectra, a low-energy cutoff of 28 (± 2) keV in the nonthermal electron distribution was determined for the April 15, 2002, flare. As a result, the energy carried by the nonthermal electrons is found to be comparable to the thermal energy of the flare, but one order of magnitude larger than the kinetic energy of the associated coronal mass ejection. The method used to deduce the electron low-energy cutoff will be useful in the analyses of similar events.

Acknowledgements

I express my deep appreciation to Dr. Gordon D. Holman, who provided inspirations for all the work, guided me through the intricacies of the research, and offered tremendous help with my daily access to Goddard. I am deeply appreciative to Dr. Brian R. Dennis, for enrolling me to do my graduate student research with RHESSI data, sharing stimulating and insightful views, and educating me on how to write scientific papers in English. I am also particularly grateful to Dr. Carol Jo. Crannell. She made my study in America possible, brought me to Goddard, and cleared the obstacles for me to work at Goddard.

I am indebted to the whole RHESSI team for their help in different aspects. My special thanks to Kim Tolbert, Richard Schwartz and Paul Bilodeau for their great help on RHESSI software and data processing, to Sam Krucker, Gordon Hurford, Markus Aschwanden, Jim McTiernan, and Edward Schmahl for their professional help on understanding RHESSI. I also want to thank Peter Gallagher and Dominic Zarro for their help on Solar Software and SOHO data analysis. I thank Merrick Berg for his generous help. I was supported by the RHESSI PI funding. I want to thank everyone who made this possible, and especially the RHESSI principal investigator, Dr. Robert P. Lin. I am deeply grateful to Dr. Stephen White for his extensive help on analyzing Nobeyama radio data and Dr. Jie Zhang for his assistance in analyzing SOHO/LASCO data. I am thankful to Leah Haga for her careful proofreading the manuscript.

Finally, I would like to thank my wife, Meijing, and my daughter, Annie, for their remarkable support.

Related Publications

Sui, L., Holman, G. D., Dennis, B. R., Determinations of Low-energy Cutoffs of Nonthermal Electrons in a Flare on 2002 April 15, 2005, ApJ, in preparation.

Sui, L., Holman, G. D., Dennis, B. R., Evidence for Magnetic Reconnection in Three Homologous Solar Flares Observed by RHESSI, 2004, ApJ, 612, 546.

Sui, L., Holman, G. D., Evidence of the Formation of a Large-scale Current Sheet in a Solar Flare, 2003, ApJ, 596, L251.

Sui, L., Holman, G. D., Dennis, B. R., Sam K., Schwartz, R. A., Tolbert K, Modeling Images and Spectra of a Solar Flares Observed by RHESSI on Feb 20, 2002, 2002, Solar Physics, 210, 245.

Contents

Abstract **ii**

Acknowledgements **iii**

1 Introduction **1**
1.1 Overview of Solar Flares 1
1.2 Overview of Flare Models 4
1.3 RHESSI 7
1.4 Motivation and Introduction to the Thesis 8

2 Modeling Images and Spectra of a Solar Flare **14**
2.1 Overview of HXR Looptop Source Studies 14
2.1.1 Discovery of HXR Looptop Sources 14
2.1.2 Interpretation of HXR Looptop Sources 16
2.2 Motivation for the Modeling 17
2.3 RHESSI Observations of the Flare 17
2.4 Modeling the Flare 26
2.4.1 Modeling and Simulation of the Flare 26
2.4.2 Modeling Results 28
2.5 Summary and Discussion 33

3 Evidence for the Existence of a Current Sheet **36**
3.1 Review of the Standard Flare Model 36
3.1.1 Magnetic Reconnection in a Current Sheet 36
3.1.2 Tearing-Mode Instability 38
3.1.3 Flare Loop with a Cusp Structure 41
3.2 Evidence for Current Sheets in RHESSI Observations 42
3.2.1 RHESSI Observations of the 2002 April 15 Flare 44
3.2.2 RHESSI Observations of the 2002 April 16 Flare 52
3.3 Cusp Structure Observed in Microwaves 56
3.4 Summary 60

4 New Features in the Impulsive Phase of Flares **62**
4.1 Loop Motions in Flares 62
4.2 New Features in Loop Motions 64

4.2.1 Loop Motions in the 2002 April 14-15 Flare 64
4.2.2 Loop Motions in the 2002 April 15 Flare 69
4.2.3 Loop Motions in the 2002 April 16 Flare 72
4.3 Summary and Discussions 75

5 Low-Energy Cutoff of Nonthermal Electrons 80
5.1 Overview of Studies of the Low-Energy Cutoff 80
5.1.1 Difficulties in Determining the Low-Energy Cutoff 80
5.1.2 Flare Energetics 81
5.1.3 Comparison of CME and Flare Energies 82
5.2 Determination of the Low-Energy Cutoff 83
5.3 Thermal and Nonthermal Energies 87
5.4 Kinetic Energy of Associated CME 89
5.5 Summary and Discussion 89

6 Conclusions and Future work 91
6.1 Conclusions 91
6.2 Future work 92
6.2.1 Future Study on Modeling Flares 92
6.2.2 Future study of Magnetic Reconnection 93
6.2.3 Future Studies of the Low-Energy Cutoff and Flare Energetics . . . 96

References 99

Chapter 1

Introduction

1.1 Overview of Solar Flares

A solar flare is an enormous explosion in the solar atmosphere, involving sudden bursts of particle acceleration, plasma heating, and bulk mass motion (for overviews see Tandberg-Hanssen, & Emsilie, 1988; Zirin, 1988; Phillips, 1992; Aschwanden, 2004). In the largest flares, 10^{32} ergs or more (equivalent to 25 million 100-megaton hydrogen bombs) can be released in a few minutes to a few tens of minutes. Radiation is emitted across virtually the entire electromagnetic spectrum: γ-rays, X-rays, ultraviolet, white light, H-α line, infrared, microwave and radio. Various phenomena accompanying flares may last for as little as a few minutes, or as long as a few days. The first solar flare recorded was on September 1, 1859. Two scientists, Richard C. Carrington and Richard Hodgson, were independently observing sunspots at the time, when they viewed a large flare in white light. Figure 1.1 shows a H-α image of a flare on August 7, 1972.

Flares invariably occur in "active regions" on the Sun where several sunspots and complicated magnetic field configurations are under development (see Fig. 1.2). Because of the association with active regions, the frequency of flares follows the eleven-year sunspot cycle. Classification of flares is usually based on their extent and brightness in specific wavelengths. Using the maximum soft X-ray (1–8 Å) emission measured with the GOES satellites, flares are classified into (from weak to strong): A, B, C, M, and X.

Big flares often are accompanied by coronal mass ejections (CMEs). A CME is a huge ($> 10^{12}$ kg) cloud of hot plasma expelled from the Sun (see Fig. 1.3). Both flares and CMEs can accelerate ions and electrons. These accelerated particles may travel through interplanetary space as far as the Earth's orbit and beyond. The CME is often preceded by a shock front. When the shock reaches the Earth, a magnetic storm may result. Therefore, big flares and CMEs can profoundly affect human activities, posing life-threatening hazards to astronauts, disrupting communications both in space and on the ground, damaging satellites, and even knocking out entire metropolitan power grids as happened in Toronto, Canada in March of 1989.

Typical flare images in soft X-rays (SXRs) show a flare loop or an arcade of loops, and two footpoints or two ribbons in hard X-rays (HXRs). As described in Figure 1.4, a general interpretation of the observations is that particles are somehow accelerated by

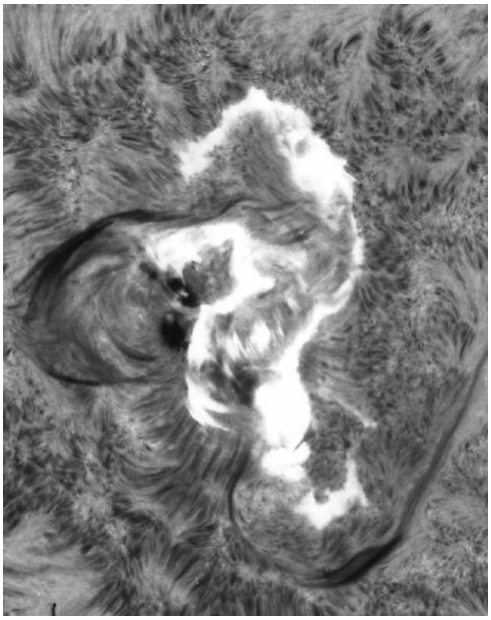

Figure 1.1: H-α image of the flare on August 7, 1972, observed with the Big Bear Solar Observatory. This image shows the two-ribbon structure (white), with bright H-alpha loops connecting the ribbons.

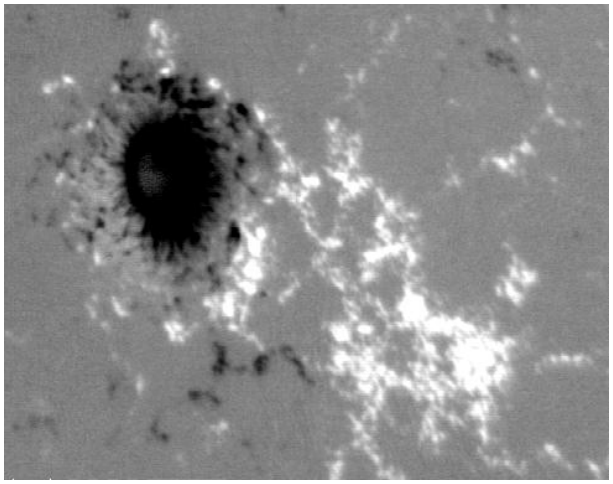

Figure 1.2: An "active region" (NOAA region 7912) seen in a Magnetogram, observed with the 26″ vacuum reflector of the Big Bear Solar Observatory on October 25th, 1995. The black and white regions indicate negative and positive magnetic polarities, respectively. This active region produced several flares.

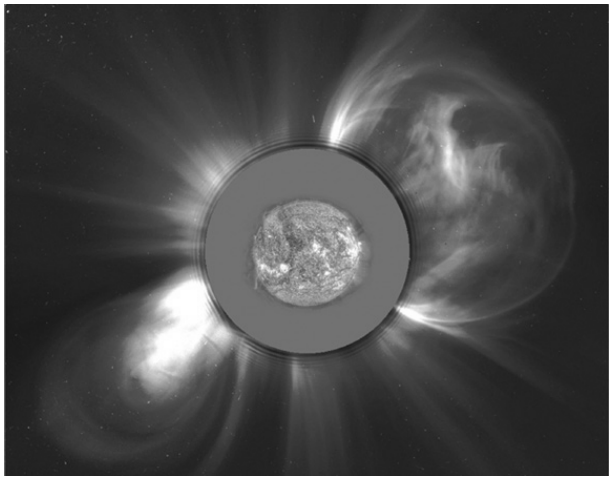

Figure 1.3: A CME observed with the Large Angle and Spectrometric COronagraph (LASCO) on board the Solar and Heliospheric Observatory (SOHO) on November 8, 2000. It looks like a balloon expanding outwards.

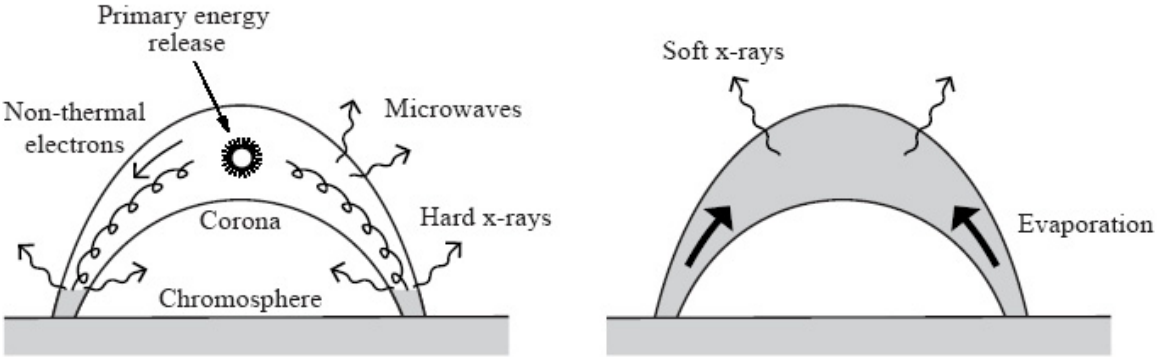

Figure 1.4: Illustration of the production of hard X-rays and soft X-rays in flares (from Priest & Forbes, 2002).

the energy released in the corona and transported down to the footpoints of the magnetic tube where they lose all their energy in Coulomb collisions with dense, ambient plasma and emit HXR bremsstrahlung, referred to as thick-target, nonthermal bremsstrahlung (Brown, 1971; Hudson, 1972; Lin & Hudson, 1976). The cooler plasma is then heated and evaporated to fill the magnetic tube, emitting thermal bremsstrahlung to form the flare loops seen in SXRs. The nonthermal thick-target model has explained successfully the observed radiative signatures of flares at a number of wavelengths (Miller et al., 1997, and references therein). Striking support also comes from the observation of simultaneous with a fraction of a second impulsive HXR emissions from two footpoints of a flare loop (e.g., Sakao, 1994), as would be expected from the interaction of electron beams with the chromosphere.

1.2 Overview of Flare Models

It is now widely accepted that magnetic reconnection occurs in the corona to power eruptive solar events such as flares and CMEs (for an overview see Aschwanden, 2002). By the term "magnetic reconnection", I am referring to a process by which magnetic flux is swept into a small area where oppositely directed components annihilate each other, and the residual magnetic tension in the newly-reconnected field causes the field and plasma to be expelled from the reconnection region (McKenzie, 2002). The magnetic energy is converted into the thermal and kinetic energies of energetic particles in the flare.

Based on the number of magnetic poles (or footpoints) involved in a flare, three classes of models are defined by Aschwanden (2002): (1) bipolar, (2) tripolar, and (3) quadrupolar models. The **bipolar flare models**, or the so called Carmichael-Sturrock-Hirayama-Kopp-Pneuman (CSHKP) reconnection models (Carmichael, 1964; Sturrock, 1966; Hirayama, 1974; Kopp & Pneuman, 1976), have become the standard flare scenario (see Fig. 1.5). They have continuously evolved over the last several decades into more complex versions, one of which is shown in Fig. 1.6 [1]. In these models, oppositely directed magnetic fields in the corona reconnect in a current sheet, and the tension that exists in the resulting non-potential field causes the expulsion of two oppositely directed jets. A large, helical magnetic loop, or plasmoid, with two ends anchored on the Sun moves upwards, while the downward directed material piles up to form an arcade of loops.

The **tripolar flare model** was created to explain the reconnection between an open field line and a closed field line. The tripolar reconnection appeared in the context of emerging-flux models (e.g., Heyvaerts, Priest, & Rust, 1977) and the discovery of soft X-ray jets with Yohkoh (e.g., Shibata et al., 1992; Yokoyama, & Shibata, 1995; Canfield et al., 1996). Observations of long, straight, soft X-ray jets were taken as evidence of plasma flows along open field lines produced by the magnetic reconnection between an emerging or canceling small-scale loop and an open field line of the ambient corona. One of the modern versions of the tripolar model is described in Figure 1.7.

The **quadrupolar flare model** involves the interaction of two closed field lines. The cartoon in figure 1.8 describes the formation of a current sheet when two magnetic dipoles approach each other. A classic scenario describes the formation of a current sheet between the anti-parallel magnetic fields of an emerging flux tube and a pre-existing, overlying larger-scale loop (e.g., Heyvaerts, Priest, & Rust, 1977). The observations indicate that magnetic flux could emerge either inside or outside a pre-existing long loop (e.g., Sakai & de Jager, 1991; Shibata et al., 1992; Strong et al., 1992; Shimojo et al., 1996). Because the overlying large-scale loop usually has one of its footpoints close to a footpoint of the reconnecting small-scale loop, most of the observations supporting this model show only three footpoints (Nishio et al., 1997).

In addition to a favorable magnetic topology, a solar flare requires a trigger or driver before the magnetic field configuration loses its equilibrium and evolves into a new equilibrium in a lower energy state. The study of the initiating mechanism is one of the most important tasks for us in understanding solar flares because it determines the currents

[1] All the flare cartoons are obtained from the "Grand Archive of Flare and CME Cartoons" collected by Hugh Hudson (http://solarmuri.ssl.berkeley.edu/~hhudson/cartoons/overview.html)

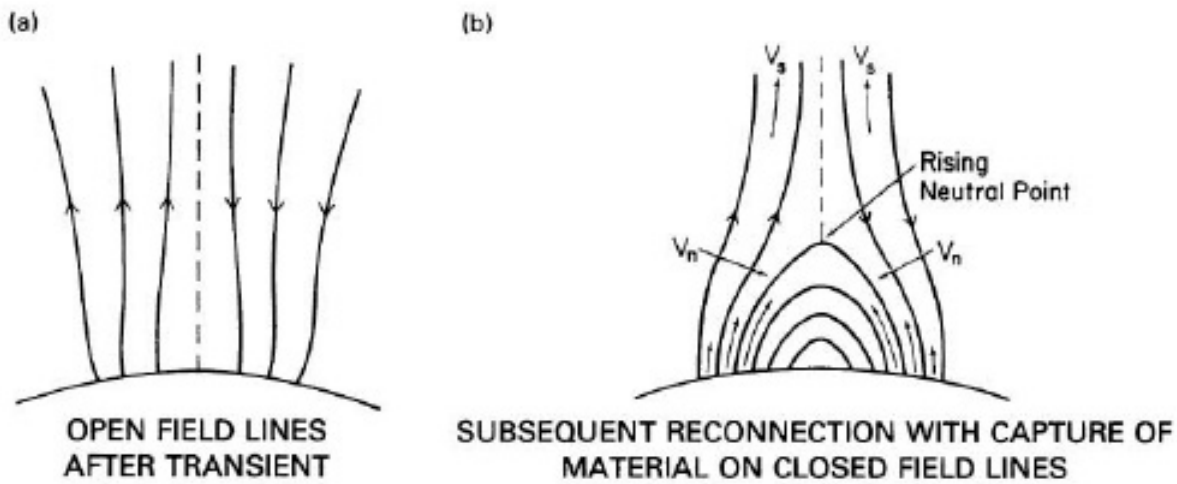

Figure 1.5: Flare model by Kopp & Pneuman (1976). (a) The magnetic field is pushed open, and a current sheet is formed. (b) The magnetic reconnection forms two separating ribbons and a continuous rising loop system.

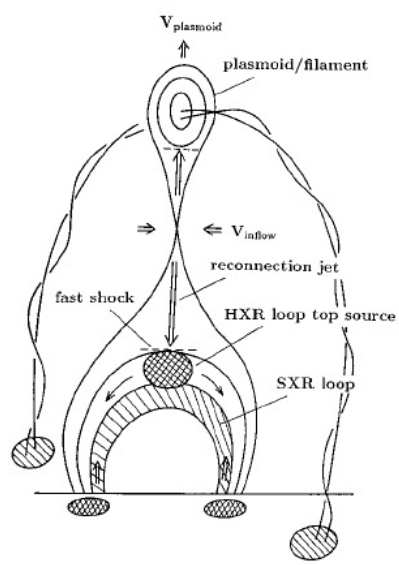

Figure 1.6: A compact flare loop model developed from the standard CSHKP flare models (from Shibata et al., 1995).

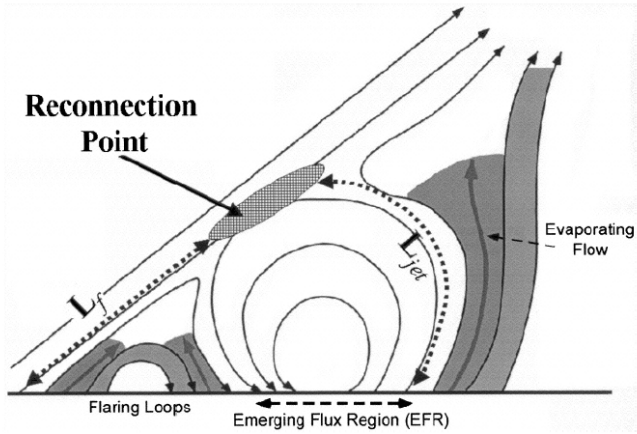

Figure 1.7: A modern version of the tripolar flare model (from Shimojo, & Shibata, 2000). The magnetic reconnection occurs between an overlying coronal magnetic field and emerging flux.

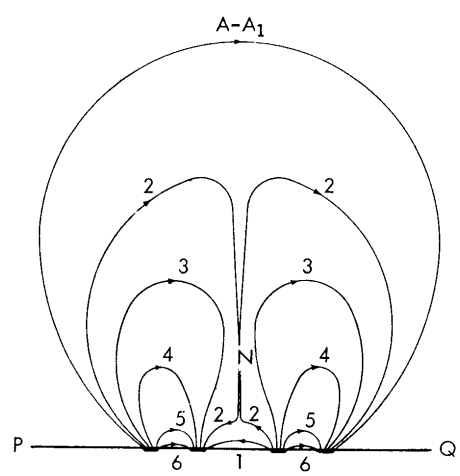

Figure 1.8: A classic quadrupolar flare model (from Sweet, 1958). Two magnetic dipoles approach each other to produce a current sheet with " neutral line" N.

and electromagnetic fields that are required in the pre-flare phase for energy release and particle acceleration during the impulsive phase (Aschwanden, 2002).

There have been many possible driver models proposed in the literature. For example, Hirayama (1974) proposed that the rising prominence (a strand of relatively cool gas in the solar corona) above a magnetic neutral line, which carries an electric current parallel to the neutral line, induces a magnetic collapse on both sides of the current sheet to form a bipolar flare topology. Forbes & Priest (1995) proposed that converging photospheric flow or flux emergence leads to the formation of a sheared arcade field containing a flux rope (a flux tube with twisted magnetic field lines). Two photospheric field sources of opposite polarity approach each other until a catastrophe point is reached and the flux rope erupts. The eruption drives reconnection in a current sheet below the flux rope. The break-out model (Antiochos, 1998; Antiochos, Devore, & Klimchuk, 1999) is a driver model for flares with quadrupolar magnetic topology. In this model, reconnection between the sheared arcade and the adjacent arcade removes the unsheared field above the low-lying primary arcade and allows the core flux to burst open, leading to a filament eruption, a flare, and a CME. Uchida et al. (1999) and Hirose et al. (2001) proposed another scenario for the quadrupolar model in which a dark filament containing longitudinal magnetic field is supported in a thin current sheet between two magnetic loop systems. The filament acts to prevent the energy release while the energy of the system builds up. Magnetic reconnection occurs as the dark filament is squeezed out.

1.3 RHESSI

The Reuven Ramaty High Energy Solar Spectroscopy Imager (RHESSI, Lin et al., 2002), launched on February 5, 2002, is designed to investigate particle acceleration and energy release in solar flares through imaging and spectroscopy of the hard X-ray/γ-ray continua emitted by energetic electrons, and of γ-ray lines produced by energetic ions. It covers a broad energy range from 3 keV to 17 MeV, with an energy resolution as fine as 1 keV FWHM. The spatial resolution is as fine as 2.3 arcsec in the X-ray range, with source centroids located to even higher, subarcsecond accuracy. The single instrument (see Fig. 1.9) consists of an imager, made up of 9 bi-grid collimators, in front of a spectrometer with 9 germanium detectors (Smith et al., 2002), one behind each collimator. The images are reconstructed from the incident fluxes which are time-modulated by the 9 modulation collimators as the spacecraft rotates at $\sim$15 rpm (Hurford et al., 2002). RHESSI provides the first high-resolution HXR imaging spectroscopy, the first high-resolution γ-ray line spectroscopy, and the first imaging above 100 keV, including the first imaging in γ-ray lines. Saturation from intense soft X-ray fluxes is generally avoided with the aluminum (thin and thick) attenuators that automatically move into the detectors' fields of view when the count rates exceed predetermined thresholds.

With these unprecedented capabilities, RHESSI can determine the location, temperature, and emission measure of the hottest plasma, i.e., the plasma that is closest to the point in time and space where the heating takes place. The HXR observations provide the location, spectrum, and temporal evolution of the accelerated electrons that contain a large fraction of the total energy released in a flare. The combination of the two capa-

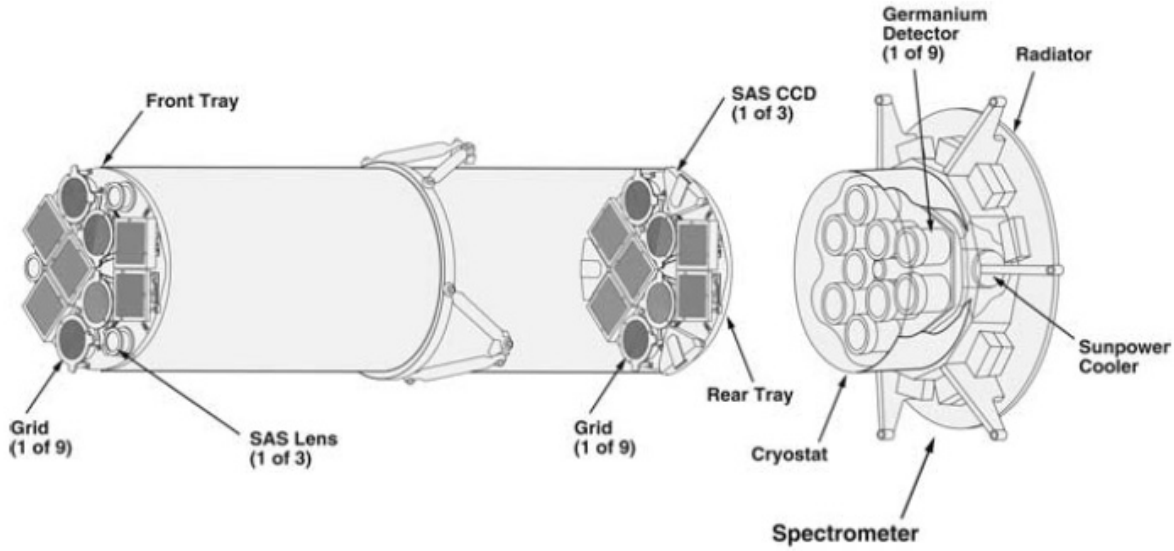

Figure 1.9: Schematic of the RHESSI instrument (from Hurford et al., 2002).

bilities in the same instrument allows these two flare components – the thermal and the nonthermal – to be studied together in ways that have not previously been possible.

1.4 Motivation and Introduction to the Thesis

After more than two decades of studies, we have a better understanding of solar flares. As pointed out by McKenzie (2002), solar flares are defined by magnetism. The flare energy is stored, transferred, and released in and by the magnetic field of the Sun. The structures in which flares occur are wholly dependent on the configuration of magnetic connections. It is the rearrangement of these connections that we believe plays a large and important role in many of the processes observed in flares. Despite all the progress, there are many fundamental questions yet to be answered, such as: How is the flare energy stored and released? What is the trigger of the energy release? When do current sheets form in flares and how do they evolve? How and where are electrons and ions accelerated? Do the high energy particles carry a significant fraction of the released energy? In this thesis, I focus on the following specific questions by analyzing flares mainly with the RHESSI observations.

Where are particles accelerated in flares? The Sun is the most powerful particle accelerator in the solar system. It accelerates ions up to tens of GeV and electrons to hundreds of MeV in solar flares and in fast CMEs. It is not clear how the Sun rapidly accelerates electrons and ions with such high efficiency. Several particle acceleration models have been proposed (see a review by Miller et al., 1997). I have not studied how these particles are accelerated. Instead, I investigate where the acceleration sites are located.

From the HXR and radio observations, it is known that electron acceleration occurs in

a wide range of heights in the solar atmosphere (see the review by Vilmer & MacKinnon, 2002). Different studies have indicated that electron beam acceleration arises from a medium with a plasma density ranging from 10^9 to 10^{11} cm^{-3}, located at a height of a few 10^4 km above the photosphere (e.g., Benz & Aschwanden, 1991; Aschwanden et al., 1995). Before RHESSI, no direct information was available on the location of the ion acceleration sites. Ions were formerly considered to be accelerated in the same region as electrons, given the simultaneity of radiation from electrons and ions generally observed (Vilmer & MacKinnon, 2002, and references therein). RHESSI has provided the first direct information on the location and spatial extent of the energetic ion interaction region in a solar flare. In the X4.8 flare of 2002 July 23, the 2.223-MeV line emission centroid was found to be displaced by $\sim 20''(\pm 6'')$ from the centroid of the 0.3-0.5 MeV and 0.7-1.4 MeV electron bremsstrahlung sources (Hurford et al., 2003, , see Fig. 1.10). Lin et al. (2003a) also found that the 2.223-MeV line emission centroid lies very close to the footpoints of large post-flare loops, while the HXR emission corresponds to the ends of a much shorter loop. The separation of the centroids clearly implies a difference in acceleration and/or propagation between the accelerated electron and ion populations (Lin et al., 2003a).

One surprising discovery of the Yohkoh Hard X-ray Telescope (HXT) was an impulsive HXR source ($\geq$20–50 keV) above the top of flare loops (Masuda et al., 1994, 1995), besides the well-known (usually double) footpoint sources predicted by the thick-target bremsstrahlung model. This discovery suggested that magnetic reconnection occurs above the flare loop, and that the particle acceleration site may be located at or above the site where the HXR looptop source is located. It was not clear how electrons can emit collisional bremsstrahlung in such low plasma densities. An interpretation in terms of thermal HXR emission (Masuda et al., 1994) was ruled out based on the required temperatures, $T \approx 200\ MK$, for which there was no evidence from any other X-ray instrument (Aschwanden, 2002). Also, the time variability of the looptop HXR emission was too rapid to be consistent with a thermal interpretation (Hudson & Ryan, 1995). Therefore, a plausible explanation has to be collisional bremsstrahlung from nonthermal electrons.

In Chapter 2, I present RHESSI observations of a flare, which also show a HXR looptop source. In order to quantitatively interpret the looptop source, I create a particle transport model, in which the nonthermal electrons with a power-law energy distribution are assumed to be accelerated above the flare loop, and continuously injected into the flare loop. Taking into consideration of the particle transport effects, the model-predicted images are obtained. The model-predicted results are then compared with the RHESSI observations to determine whether or not such a simple model can explain the HXR looptop source.

Does a large-scale current sheet exist in flares? Although magnetic reconnection mechanisms have only been studied theoretically, decades of observations have provided many indirect pieces of evidence for the reconnection scenario: cusp-shaped soft X-ray flare loops (Tsuneta et al., 1992; Tsuneta, 1996), increase of loop height and footpoint separation with time (Bruzek, 1964; Švestka et al., 1987; Tsuneta et al., 1992; Švestka, 1996; Gallagher et al., 2002; Qiu et al., 2004), high temperature plasma along the field lines mapping to the tip of the cusp (Moore et al., 1980; Švestka et al., 1987; Tsuneta, 1996), a HXR source located above the soft X-ray loops (Masuda et al., 1994), horizontal

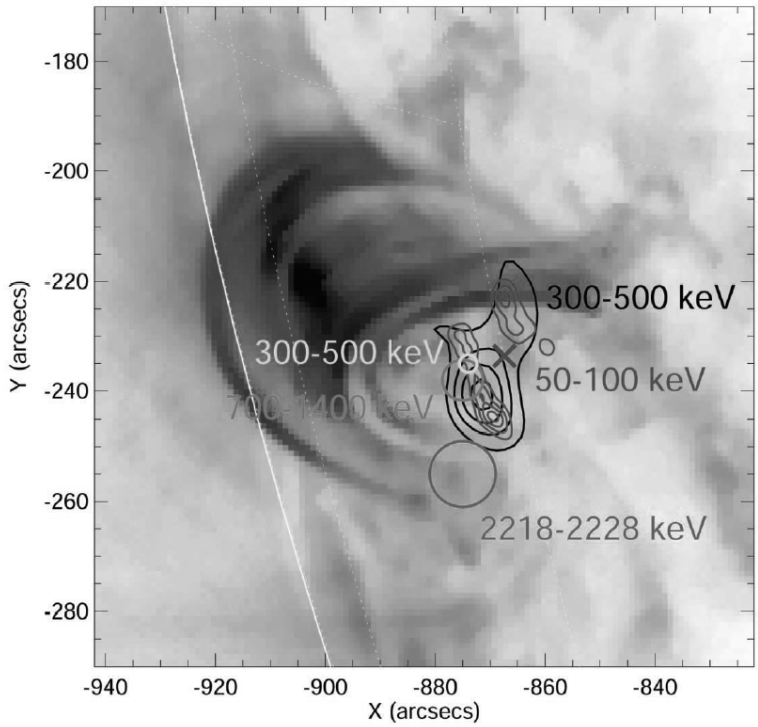

Figure 1.10: RHESSI centroid of the 2.223-MeV line emission that indicates the energetic ion interaction region, superposed on a TRACE 195 Å image taken 90 minutes after the flare, showing the post-flare loops. The circles are the centroids of the 300–500 and 700–1400 keV bands, respectively, dominated by bremsstrahlung emission. The contours show the detailed images at 300–500 keV (dark) and 50–100 keV (grey), respectively; the 50–100 keV centroid is indicated by the cross (from Lin et al., 2003a).

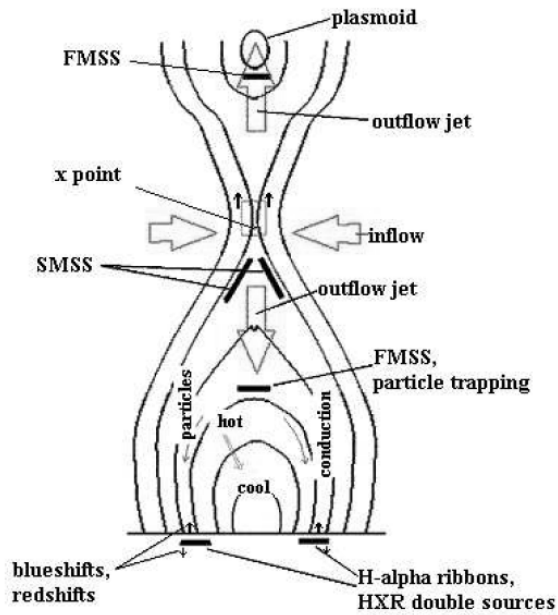

Figure 1.11: A two dimensional cartoon of the standard model, wherein post-eruption coronal arcades result from magnetic reconnection. FMSS stands for fast-mode stationary shock, while SMSS stands for slow mode stationary shock. (from McKenzie, 2002).

inflow above the cusp region (Yokoyama et al., 2001), downflow above the cusp-shaped loops (McKenzie & Hudson, 1999), an upward ejected plasmoid above the loops (Shibata et al., 1995; Ohyama & Shibata, 1998), and sudden changes in magnetic field strength and configuration (Wang et al., 2002, and references therein). A more detailed summary of the observational signatures predicted by the standard CSHKP model is given by McKenzie (2002) (see Fig. 1.11).

Despite all the signatures observed, there is one important model-predicted feature missing: a large-scale current sheet. A current sheet, or neutral sheet, is the boundary region between the annihilating opposite magnetic fields. Only after the formation of a current sheet can rapid magnetic reconnection occur. In the standard flare model, a steady reconnection process can basically be described by orthogonally-directed inflows and outflows through the current sheet (see the two pairs of arrows in Fig. 1.11), where the flows are constrained by the laws of mass and energy conservation. Early concepts, where the diffusion region during the magnetic reconnection process was a long current sheet (Sweet, 1958; Parker, 1957), were found to be too slow to explain the rapid energy release during solar flares. The process can be speeded up by reducing the diffusion region to a short current sheet with a length comparable to its thickness (Petschek, 1964). In order to explain the bursty and intermittent pulses (on time scales of seconds or subseconds) of particle acceleration seen in HXR and radio wavelengths during the impulsive phase of a flare, unsteady magnetic reconnection modes, such as the tearing-mode instability, may play an important role (see review by Sturrock, 1987; Aschwanden, 2002). In the linear tearing-mode instability, first investigated by Furth et al. (1963), one mode tends

to interact with another and small-scale structures called "magnetic islands" develop. Numerical studies by Carreras et al. (1980) show that nonlinear effects can speed up the reconnection rate.

In Chapter 3, I present RHESSI observations of two flares that strongly support the existence of a large-scale current sheet. The observations seem to indicate the collapse of an X-point magnetic configuration (Dungey, 1953) into a Petschek-type (Petschek, 1964) fast reconnection, and the later development of an unsteady tearing-mode instability (Furth et al., 1963). Microwave observations of one of the flares, for the first time showing a cusp structure, are also presented.

Do all the observations support the standard flare model? Despite the fact that many observations appear to support the standard reconnection picture, there are still many observations which do not match the model. For example, some of the essential features predicted by the standard model, such as the cusp structure (i.e., a flare loop with a pointed upper tip) (e.g., Tsuneta et al., 1992), and the plasma inflow and outflow (Yokoyama et al., 2001; McKenzie & Hudson, 1999), have been observed only occasionally. If the model is correct, why can these features not be observed in most flares, if not in all flares. Moreover, the standard model sometimes has difficulties in accounting for the observed features. The outflow speed (i.e., 40–500 km s^{-1}) reported by McKenzie & Hudson (1999) is almost one order of magnitude smaller than the expected coronal Alfven speed. As summarized by Miller et al. (1997), even the nonthermal thick-target model, an important component of the standard flare model, has difficulty in explaining the following observations: (A) plasma heating is often observed before the start of the HXR emission and hence before the production of observable nonthermal electrons; (B) the model generally predicts more upward moving material than is indicated by the observed blue-shifted component of SXR lines.

One important feature predicted in the standard model is continuous upward loop expansion. This is an apparent motion, reflecting a shift of emission to higher, newly reconnected field lines. Therefore, the flare loops would be expected to appear to move upward continuously. In Chapter 4, the apparent motion of flare loops in three homologous flares is examined. A surprising finding is that in all the three flares, around the start of the impulsive phase, the looptop centroid initially moved downwards, and then moved upwards later. The downward motion indicates that the loops decrease in height, which contradicts the prediction of the standard model.

Do high-energy particles carry a significant fraction of the released energy? It has been of interest for decades to compare the total energy of nonthermal electrons with the energy in the thermal plasma. The comparison allows us to know what fraction of the flare energy is used to accelerate electrons. Such a study is critical for an understanding of the mechanisms of particle acceleration and plasma heating in flares, and thereby provides an important constraint on electron acceleration mechanisms (Miller et al., 1997). An earlier study by Lin & Hudson (1976) indicated that the nonthermal electrons carry a large fraction, ∼10–50%, of the total flare energy, suggesting that the particle acceleration and energy release processes are intimately linked.

It is generally accepted that often-observed flare power-law photon spectra (photons s^{-1} cm^{-2} keV^{-1}), i.e., $I(E) \propto E^{-\gamma}$ (where E is the photon energy, and γ is the power-law index), are produced by nonthermal electrons with a power-law flux distribution

(electrons s^{-1} cm^{-2} keV^{-1}), i.e., $f(\varepsilon) \propto \varepsilon^{-\delta}$ (where ε is the electron energy and δ is the electron power-law index). In the case of the thick-target bremsstrahlung model, $\delta = \gamma + 1$ (Brown, 1971). The total energy carried by the nonthermal electrons is calculated with the integration $\int_{\varepsilon_c}^{\infty} f(\varepsilon)\ \varepsilon\ d\varepsilon \propto \varepsilon_c^{-\delta+2}$, where ε_c is the low-energy cutoff of nonthermal electrons. The low-energy cutoff is required to keep the integral finite. Thus, in order to obtain an accurate estimate of the total energy in accelerated electron, it is important to determine the value of ε_c, especially for electron spectra with $\delta \gg 2$, which is usually the case.

The low-energy cutoff in the electron distribution has been difficult to identify (e.g., Dennis et al., 2003; Holman, 2003), leading to a big uncertainty in determining the nonthermal energy. As summarized by Dennis et al. (2003), most early studies assumed a certain cutoff energy or a reference energy. Even with RHESSI, the cutoff energy is difficult to determine. However, an upper limit of the low-energy cutoff usually can be determined in flares observed with RHESSI (Holman et al., 2003), thus giving a lower limit to the nonthermal energy.

In Chapter 5, spectral analysis of a flare was carried out with the RHESSI Spectral Executive software (SPEX) (Smith et al., 2002). Because of its steep power-law spectra, a low-energy cutoff of 28 ($\pm$2) keV for the nonthermal electrons is obtained. As a result, the total nonthermal energy is found to be comparable to the thermal energy in the flare plasma. The technique used for deducing the cutoff energy with such precision will be useful in future studies.

Chapter 2

Modeling Images and Spectra of a Solar Flare

2.1 Overview of HXR Looptop Source Studies

2.1.1 Discovery of HXR Looptop Sources

Based on flare morphology, flares can be classified into two categories (e.g., Shibata et al., 1995): two ribbon flares and compact flares. The two ribbon flares are believed to be triggered by a filament eruption and then powered by magnetic reconnection above an arcade of flare loops. The compact flares were formerly considered to be powered by magnetic reconnection within a simple flare loop. However, the discovery of a HXR coronal source above a compact flare loop (hereafter, HXR looptop source) suggested otherwise.

Masuda et al. (1994) studied a compact flare (later called the 'Masuda' flare) observed with the Yohkoh/HXT on 1992 January 13. As shown in Fig. 2.1, the HXT 14-23 keV image shows a simple, compact flare loop. Images at higher energies (23-33 and 33-53 keV) show two footpoints of the flare loop and a HXR looptop source. The two footpoints are what we would expect for thick-target bremsstrahlung when the electrons lose all their energies at the footpoints. However, the compact HXR looptop source was a big surprise. Because the coronal density is usually around 10^{10} cm^{-3}, the electrons should not lose significant energy due to Coulomb collision in the upper corona. Masuda et al. (1994) also found that the HXR looptop source is temporally impulsive, similar to the two footpoints. Based on its apparent steep spectrum at high energies, Masuda et al. assumed that the HXR looptop source was due to thermal emission with the plasma temperature at $\sim$200 MK. They interpreted such super hot plasma as being heated by a shock front produced by magnetic reconnection above the loop.

Hudson & Ryan (1995) argued that the fast time variability ($\sim$20 s) of the looptop HXR emission was too rapid to be consistent with thermal cooling times. Later, Alexander & Metcalf (1997) analyzed the 'Masuda' flare using a new imaging algorithm called PIXON, which they claimed would allow more accurate photometry. Their analysis indicated that the HXR looptop source was nonthermal in nature, and its power-law spectrum was steeper than that of the two footpoints.

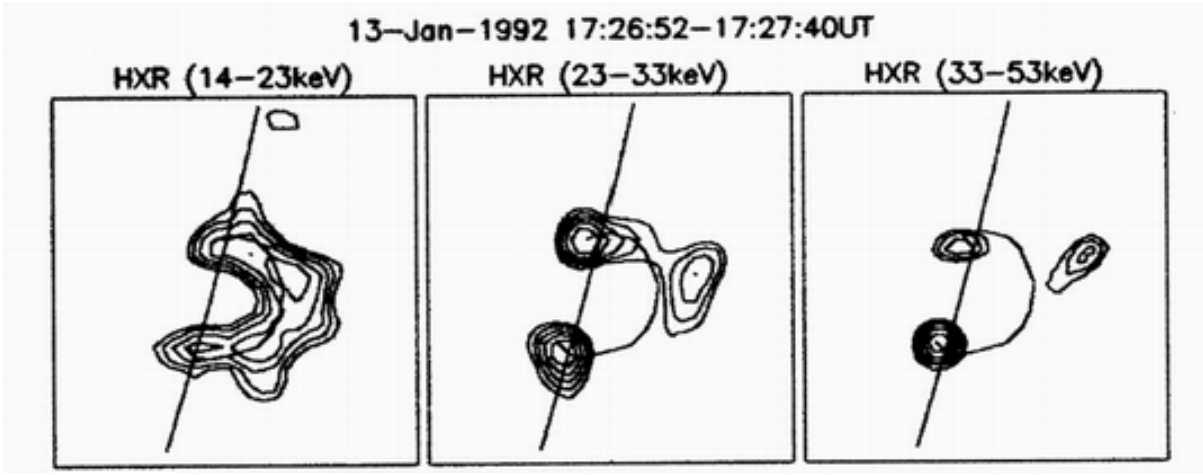

Figure 2.1: Discovery of a HXR looptop source for a flare on 13 January 1992 (Masuda et al., 1994). The three panels show contours of HXR emission in the three lower-energy bands of the Yohkoh/HXT.

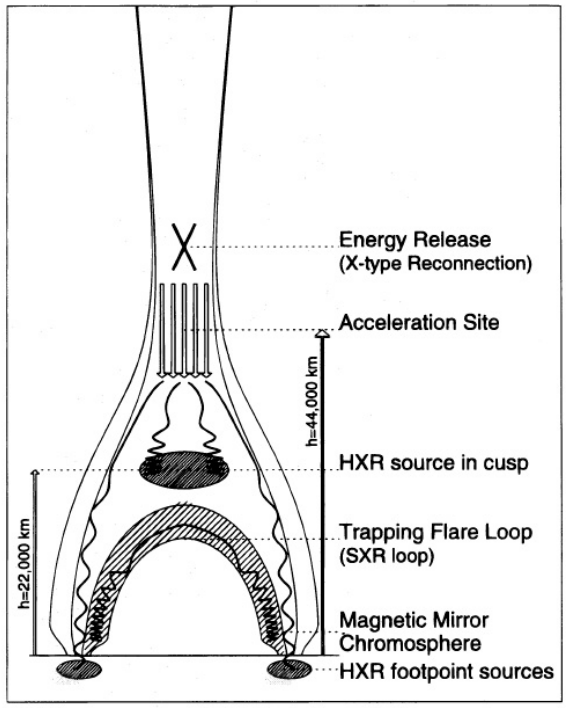

Figure 2.2: Cartoon of a possible flare scenario for the 'Masuda' flare (Aschwanden et al., 1996).

Besides the 'Masuda flare', Masuda et al. (1995) reported another two flares showing HXR looptop impulsive sources at energies $\geq$25 keV. The looptop source is relatively compact and occupies a small portion of the high temperature region seen in SXRs. Petrosian, Donaghy, & McTiernan (2002) did a statistical analysis of HXR looptop sources observed with Yohkoh/HXT in limb flares. With some specific criteria, they found 20 limb flares from 1991 October to 1998 August, for which 18 of them had sufficient data for analysis. Among the 18 flares, 15 show detectable, impulsive HXR looptop sources. Considering the limited dynamic range of Yohkoh/HXT images, they concluded that the HXR looptop sources are likely present in all flares. They found that the looptop sources were usually much weaker than the footpoints, and the ratio of footpoint flux to looptop flux is between 10 and 1. Moreover, the looptop spectra were, on average, steeper than footpoint spectra by 1 in the power-law index.

2.1.2 Interpretation of HXR Looptop Sources

The discovery of the HXR looptop source had a significant impact on our understanding of flares. In particular, this discovery is of crucial importance for understanding the primary energy release in flares. As Masuda et al. (1995) pointed out, the HXR looptop source suggests that something energetic occurs above the flare loops that is closely related to the energy release and particle acceleration during the impulsive phase of the flares. If flares are indeed powered by magnetic reconnection, then the HXR looptop source might be the first clear evidence indicating that magnetic reconnection occurs above the flare loop. A cartoon of this synthesized flare scenario is sketched in Fig. 2.2. Masuda et al. (1995) speculated that the looptop source represented the reconnecting site itself or the site where the downward directed plasma stream, ejected from the reconnection site above the HXR source, collides with the underlying closed magnetic loop. Aschwanden et al. (1996) found that the location of the particle acceleration site inferred from electron time-of-flight differences was higher than the HXR looptop source in 42 flares.

The detection of the looptop sources has generated a variety of models:

(1) Wheatland & Melrose (1995) suggested that the existence of high density plasma above the loop ($\sim 10^{12}$ cm^{-3}) can explain the observed source as thick-target HXR bremsstrahlung. The justification for this compact high density plasma is based on the results of Phillips et al. (1996) from their spectroscopic analysis of a few flares observed with the Solar Maximum Mission/Bragg Crystal Spectrometer (SMM/BCS).

(2) Using a stochastic simulation of electron transport, Fletcher (1995) found that the presence of looptop emission can be explained by the presence of electrons with large pitch angles. Electrons injected at the top of the loop with large pitch angles do not progress quickly down the loop. They remain near the looptop, orbiting the magnetic field until they are sufficiently scattered by Coulomb collisions, and then begin to move along the field. While at the looptop, they emit HXR bremsstrahlung.

(3) Using the current sheet magnetic field geometry proposed by Syrovatskii (1971), Fletcher & Martens (1998) considered the effect of having a magnetic "bottle" at the looptop where particles can be effectively trapped. These trapped particles would produce HXR bremsstrahlung above the flare loop.

(4) In a two dimension model, Holman (1996) computed the emission of nonthermal

HXR radiation from the cusp of a magnetic loop structure [1]. Because of the large energy loss rate for low energy electrons, these electrons radiate quasi-thick-target bremsstrahlung emission. When the loop density is over 10^{11} cm^{-3}, the electrons with energy less than 30 keV rapidly lose most of their energy by collisions and produce the HXR source at the cusp region.

As reviewed by Fletcher & Martens (1998), most of the work described above requires high plasma densities (up to 10^{12} cm^{-3}) to generate an observable HXR looptop source. Although there are some observations indicating high loop densities (Doschek, 1994; Phillips et al., 1996), more usual active region loop densities are a few times 10^{10}cm^{-3}.

2.2 Motivation for the Modeling

Although the models mentioned above can qualitatively explain the existence of the HXR looptop source, none of them has been quantitatively compared with flare observations. In order to test these models, we ought to check whether or not the HXR looptop source predicted by each model is consistent with satellite observations, considering their instrumental capabilities and image dynamic range, whether or not the model-predicted HXR looptop source and footpoint spectra agree with the observed counterparts, and whether or not the required model parameters are reasonable for the observed flaring environment.

Because the model proposed by Holman (1996) does not require any special geometry or high density in the looptop region, it is the simplest one among the models listed above. Holman (1996) did not include electron pitch angle scattering or magnetic mirroring in the flare loops. Moreover, he did not consider instrumental capabilities and image dynamic range. In the following sections, I apply a particle transport model, based on the model proposed by Holman (1996) to compare with the RHESSI observations of a solar flare on 2002 February 20. The RHESSI images appear to show two footpoints and a looptop source in HXRs. My goal was to determine if the observations are consistent with a simple steady-state particle transport model in which high-energy electrons are continuously injected at the top of a semicircular flare loop.

I selected this event because: (1) the RHESSI HXR images show two clear-cut footpoints and one faint looptop source, (2) the flare occurred close to the solar limb so the HXR looptop source and the footpoints are well separated, and (3) the count rate in the 50-100 keV band is well above the background level, giving a reliable spectrum up to 100 keV at the flare HXR peak.

2.3 RHESSI Observations of the Flare

On 2002 February 20, RHESSI observed a C7.5 flare in NOAA active region 9825, located near the northwest limb of the Sun at N16W80 (919″W, 285″N). The soft X-ray flare observed with GOES-8 started at 11:02 UT and ended at 11:12 UT. The RHESSI HXR peak time was 11:06:20 UT, as shown in the RHESSI light curve (Fig. 2.3).

[1]The model results can be seen at http://hesperia.gsfc.nasa.gov/sftheory/loop.htm

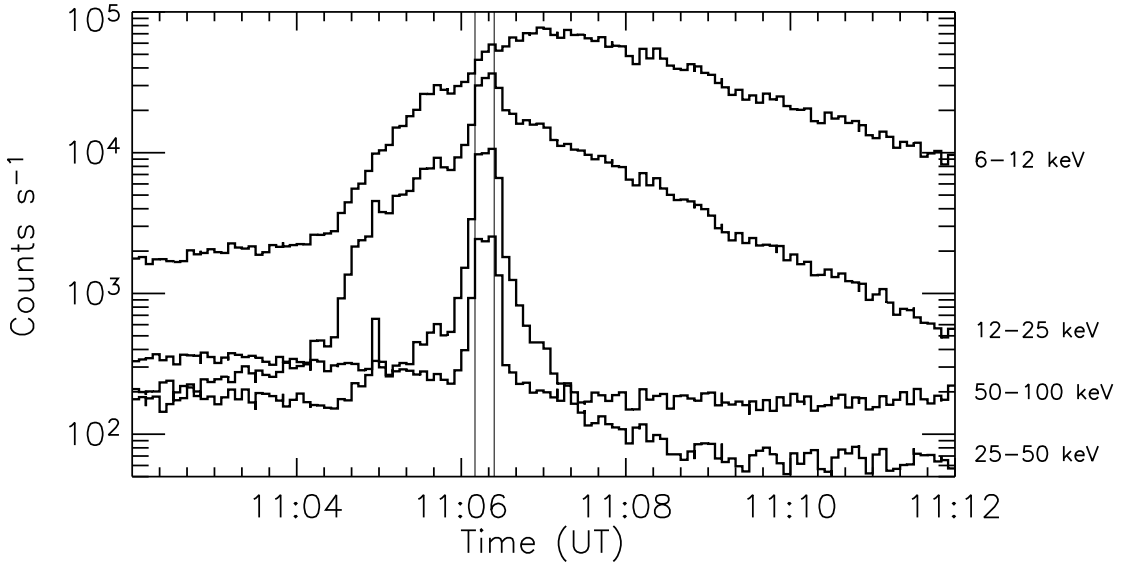

Figure 2.3: RHESSI light curves in four energy bands for the flare on 20 Feb. 2002. The count rates are binned in 4 s time intervals ($\sim$ 1 RHESSI rotation period). For clarity, I have scaled the count rates by 5.0 (6-12 keV), 1.5 (12-25 keV), 1.0 (25-50 keV), and 1.0 (50-100 keV). The two vertical lines show the integration time interval for the RHESSI images and spectra in Figs. 2.4, 2.5, and 2.6.

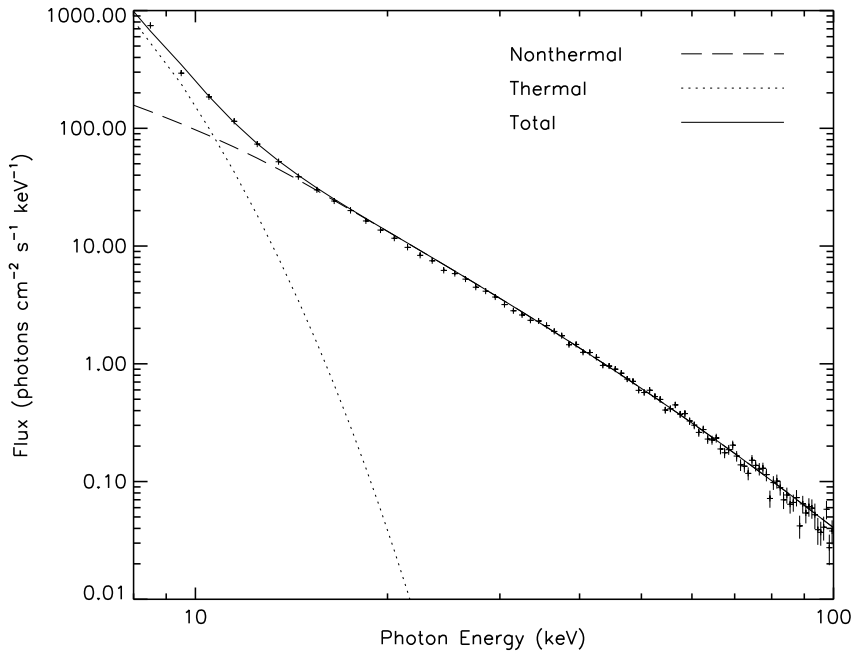

Figure 2.4: RHESSI spatially integrated photon spectrum for the time interval 11:06:10–11:06:24 UT. The bremsstrahlung spectra from an isothermal plasma and from a double power-law electron distribution (both shown separately in the plot, in addition to the total spectrum) provided the best fit to the RHESSI count-rate data after background subtraction. The error bars on the data points are the quadrature sum of the 1σ statistical uncertainties and a 5% systematic uncertainty. See Table 2.2 for the best-fit spectral parameters.

Spectral Analysis

The spatially integrated and background-subtracted photon spectrum at the time of the HXR peak, 11:06:10-11:06:24 UT (between the two lines in Fig. 2.3), is shown in Figure 2.4. The photon spectrum was obtained by (forward) fitting the RHESSI count-rate data to the bremsstrahlung spectrum from an isothermal plasma plus a double power-law electron distribution (assuming thick-target). The goodness of the spectral fitting is based on the reduced chi-square. The fitting process and limitations with the forward-fitting method are discussed in § 6.2.3. A detailed description of the RHESSI spectrometer, spectral fitting procedures, and current limitations is given by Smith et al. (2002).

The emission measure and temperature determined from the fit to the spectrum in Fig. 2.4 are 2×10^{48} cm^{-3} and 15 MK, respectively. The corresponding emission measure and temperature from the GOES-8 soft X-ray data at 11:06:20 UT are 3×10^{48} cm^{-3} and 14 MK, respectively. They were determined using the program GOES_TEM.PRO in the Solar Software tree (SSW), which was developed from the concepts of Garcia (1994) and Thomas et al. (1985). The GOES-8 results are consistent with those from the spectral fit to the RHESSI data.

The RHESSI thin shutters were in the field of view for this event. When the thin shutters are in, the effective area of the detectors drops rapidly as the photon energy falls

below 10 keV. The present uncertainty in the correction factor is large at these energies, so fluxes below 10 keV were not included in the spectral fitting. The X-ray background fluxes are almost half the total fluxes at photon energies above 100 keV, so fluxes at energies above 100 keV were also not included. The background varied with time during this flare. It was subtracted from the flare data by obtaining a linear fit to measurements of the background flux before and after the flare. Below 100 keV uncertainties in the fluxes resulting from the background subtraction were less than 20%.

Several functions provide a good fit to the nonthermal part of the spatially integrated spectrum. I first tried a double power-law function:

$$I(E) = \begin{cases} C\ (E/E_p)^{-\gamma_1} & \text{for } E < E_b \\ C\ E_b^{-\gamma_1+\gamma_2}(E/E_p)^{-\gamma_2} & \text{for } E > E_b \end{cases} \tag{2.1}$$

where I(E) is the observed HXR photon flux (photons s^{-1} cm^{-2} keV^{-1}) at photon energy E; E_b is the photon break energy, E_p is the pivot energy set to 50 keV by default, -γ_1 and -γ_2 are the power-law indices below and above E_b, respectively. The double power-law fit to the photon spectrum included with RHESSI spectral executive (SPEX) software (see Smith et al., 2002) gives a best-fit spectral index of 3.3 below 56 keV and 4.3 above 56 keV. The normalization constant of the double power-law function (C) is 0.6 photons s^{-1} cm^{-2} keV^{-1}. The calculation of the reduced chi-squared χ_r^2 is based on 1σ statistical errors and 5% of systematic errors, giving a value of 0.9. Since the systematic error is unknown for RHESSI at this stage, the value of χ_r^2 can only be used for relative comparison purposes.

The fit shown in Fig. 2.4 is the bremsstrahlung spectrum that results from a double power-law electron density distribution $f(\gamma)$ (electrons cm^{-3} keV^{-1}) assuming thick-target bremsstrahlung (Brown, 1971). For a double power-law electron distribution, $f(\gamma)$ is:

$$f(\gamma) = \begin{cases} 0 & \text{for } \varepsilon < \varepsilon_c \\ Q\ (\gamma-1)^{-\delta_1} & \text{for } \varepsilon_c \leq \varepsilon \leq \varepsilon_b \\ Q\ (\gamma-1)^{-\delta_1+\delta_2}(\gamma-1)^{-\delta_2} & \text{for } \varepsilon > \varepsilon_b \end{cases} \tag{2.2}$$

where $\gamma = 1/\sqrt{1-(\frac{v}{c})^2}$ is the relativistic factor, v is the electron speed and c is the speed of light. The electron kinetic energy $\varepsilon = (\gamma-1)mc^2$, where m is the mass of the electron, so that mc^2 is the rest mass energy of the electron in keV (i.e., 511 keV). ε_c is the electron low-energy cutoff, and ε_b is the electron break energy. -δ_1 and -δ_2 are power-law indices below and above ε_b, respectively. $f(\gamma)$ is normalized so that

$$\int_{\gamma_c}^{\gamma_{hi}} f(\gamma)d\gamma = 1 \tag{2.3}$$

γ_c and γ_{hi} are the relativistic factors related to the electron low-energy and high-energy cutoffs, respectively. Q is the normalization factor.

The photon flux, I, at photon energy E = ε_x is computed using the following thick-target bremsstrahlung equation (Brown, 1971):

$$I(E=\varepsilon_x) = \frac{n\ N\ A}{4\ \pi\ (R)^2}\frac{1}{(mc^2)^2}\int_{\varepsilon_x}^{\varepsilon_{hi}} f(\gamma_o)\ v_o\ [\int_{\varepsilon_x}^{\varepsilon_o} \frac{\sigma(\varepsilon_x,\varepsilon)\ v}{d\varepsilon/dt}\ d\varepsilon]\ d\varepsilon_o \tag{2.4}$$

Table 2.1: Parameters for the best-fit double power-law photon spectrum.

T (MK)	EM ($10^{48} cm^{-3}$)	Flux at 50 keV (photons s^{-1} cm^{-2} keV^{-1})	γ_1	E_b (keV)	γ_2	χ_r^2
15	2	0.6	3.3	56	4.3	0.9

Table 2.2: Parameters for the best-fit electron spectra.

Model	T (MK)	EM ($10^{48} cm^{-3}$)	electron flux (electrons s^{-1})	ε_c (keV)	δ_1	ϵ_b (keV)	δ_2	ε_{hi} (keV)	χ_r^2
Double Power-law	15	2	$3.7 \cdot 10^{35}$	15	4.4	100	5.5	5000	1.3
Single Power-law (option 1)	20	0.7	$3.7 \cdot 10^{35}$	15	4.5	...	...	224	1.3
Single Power-law (option 2)	40	0.05	$2.5 \cdot 10^{34}$	47	5.3	...	...	5000	1.5

Here, n and N are the number density of the thermal plasma and the energetic electrons, respectively. A is the area of the emitting region (i.e., footpoint area of a flare loop). R is the distance from the source to the detector, taken to be one astronomical unit. ε_{hi} is the electron high-energy cutoff. I used the relativistic cross section (σ) from Haug (1997). $d\varepsilon/dt$ is the collisional energy loss rate, taken to be

$$d\varepsilon/dt = 4\pi r_0^2 nc \ln \Lambda/\beta \tag{2.5}$$

Here, r_0 is the classical radius of the electron, $\ln \Lambda$ is the Coulomb logarithm, and β is v/c.

The best-fit photon spectrum shown in Fig. 2.4 was derived from a double power-law electron spectrum with an index of 4.4 below 100 keV and 5.5 at higher energies. With a low-energy cutoff in the electron distribution at 15 keV (the reason for choosing this cutoff energy is discussed later), the total integrated electron flux is $\sim 3.7 \times 10^{35}$ electrons s^{-1}. The χ_r^2 of the fit is 1.3.

The bremsstrahlung spectrum for a single power-law electron distribution with a high-energy cutoff (called option 1 in Table 2.2) also provides a good fit to the data (with reduced χ_r^2 of 1.3). This gives a power-law index of 4.5 and a high-energy cutoff of 224 keV. The value of the electron flux is the same as before. A single power-law electron distribution with a low-energy cutoff at 47 keV (option 2) also provides an acceptable fit to the data (with reduced χ_r^2 of 1.5). The power-law index is 5.3, and the total integrated electron flux is $\sim 2.5 \times 10^{34}$ electrons s^{-1}. However, this fit requires a much higher temperature for the thermal plasma, 40 MK, with an emission measure of 5×10^{46} cm^{-3}. Tables 2.1 and 2.2 list all the spectral fitting parameters mentioned above.

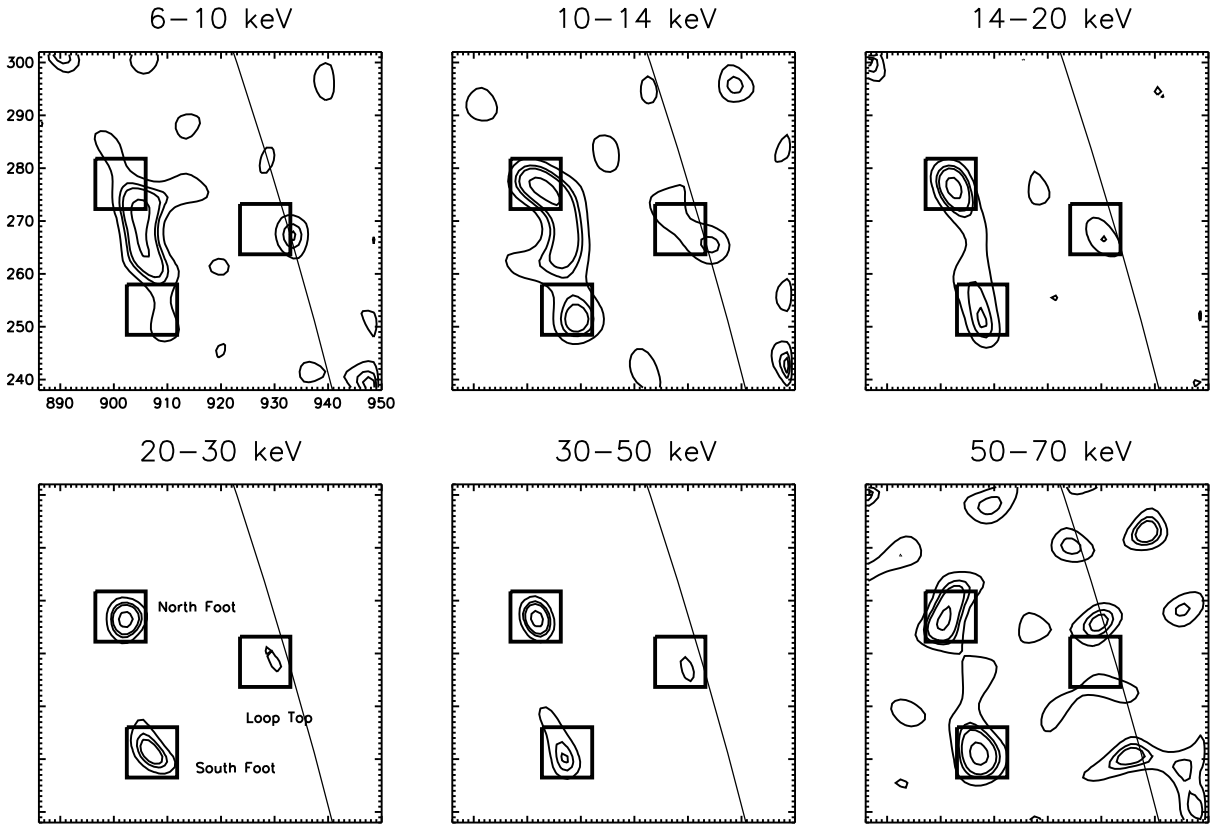

Figure 2.5: Images obtained with the MEM-Sato algorithm (Hurford et al., 2002) for time interval 11:06:10 UT – 11:06:24 UT. The contour levels are 0.08, 0.2, 0.3, and 0.7 of the peak flux in each image. The smooth line shows the location of the solar limb. Each image is 64 × 64 arcseconds in size with 1×1 arcsec pixels. The three boxes indicate the areas used to obtain the footpoint and looptop spectra in Fig. 2.8.

Image Analysis

RHESSI images in six energy bands at the time of the HXR spike are plotted in Fig. 2.5 and 2.6. Each image is 64 × 64 arcseconds in size with 1×1 arcsec pixels. RHESSI grids 3 to 8 were used to reconstruct the images, giving a spatial resolution of ∼7″. Collimator 9 was not included, because all source structure was well below its FWHM resolution of 180″ in extent.

In order to check the reliability of different image reconstruction algorithms, images using both the Maximum Entropy (MEM-Sato, Fig. 2.5) and the CLEAN (Fig. 2.6) reconstruction techniques were obtained. MEM-Sato is an image reconstruction algorithm utilizing the maximum entropy method (MEM) described by Sato et al. (1999), modified for RHESSI. The CLEAN algorithm is an iterative procedure that removes sidelobes from a "dirty" map made using the back projection image reconstruction procedure (Hurford et al., 2002).

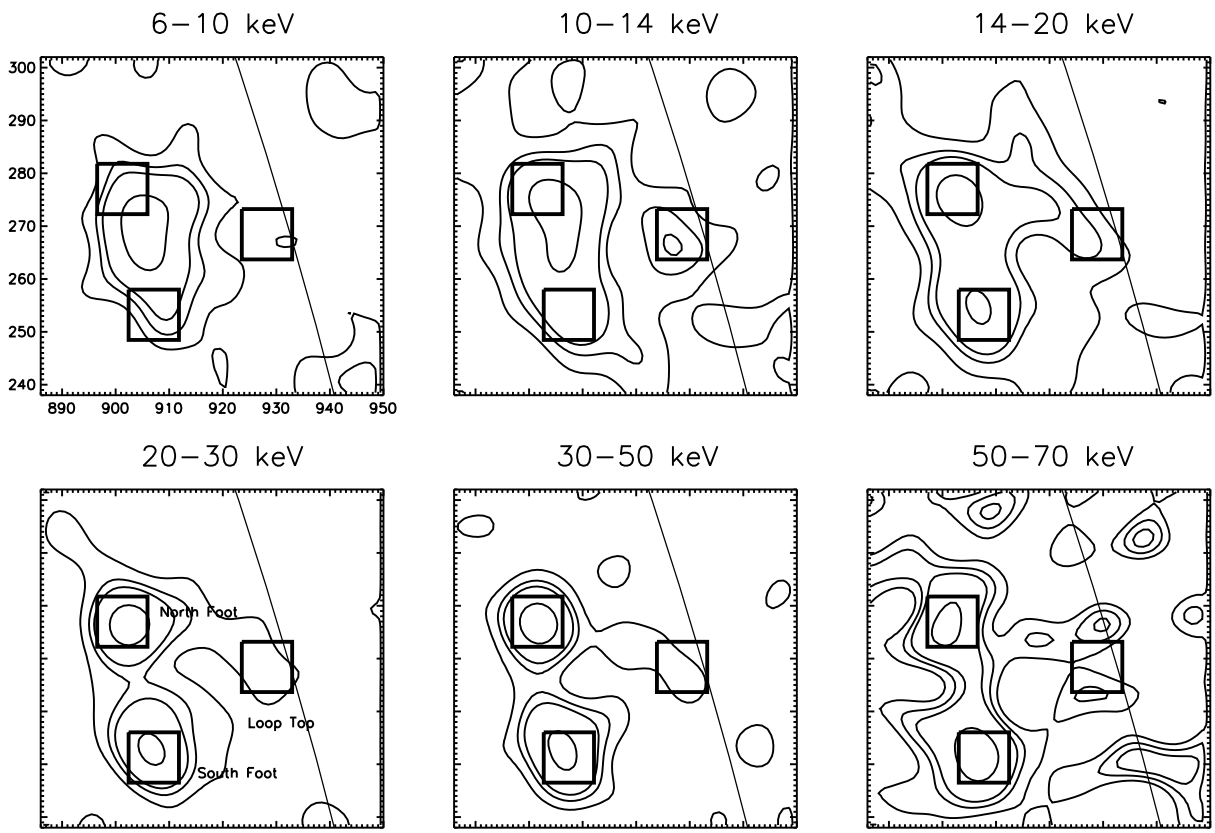

Figure 2.6: Images obtained with the CLEAN algorithm (Hurford et al., 2002). All other aspects are the same as in Fig. 2.5.

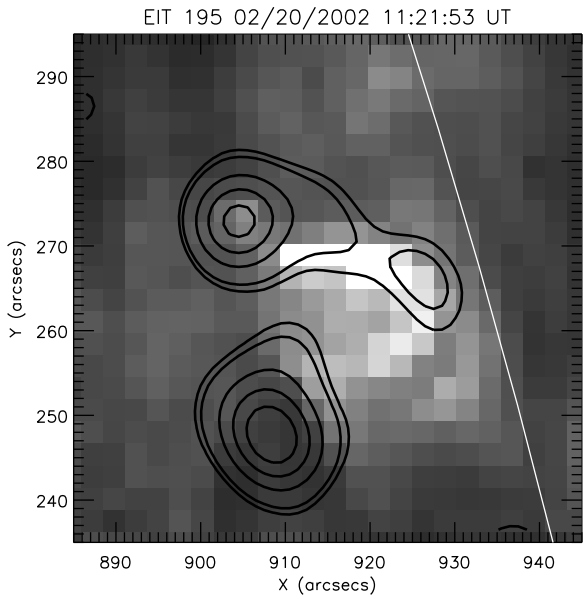

Figure 2.7: Overlay of RHESSI 20-30 keV CLEAN image (11:06:18–11:06:22 UT) on a later EIT image at 195 Å (11:21:53 UT). The contour levels are 15, 20, 40, 60, and 80% of the peak flux in the RHESSI image.

The CLEAN and MEM-Sato images agree with each other in coarse structure. In the low energy band (6-10 keV), the images show an elongated source between the two footpoints observed at higher energies. Since the flare spectrum (see Figure 2.4) at low energies can be fitted to a exponential function (i.e., presumably due to thermal bremsstrahlung), this elongated source is believed to be a thermal source with a temperature of 15 MK. In the 10-14 keV band, the images show the same thermal source plus a looptop source. In the energy bands between 14 and 50 keV, the images show two separate footpoints and the looptop source. In the 50-70 keV band, the looptop source is not apparent, although the quality of the image is marginal because of the low count rate.

Based on the RHESSI images, two loops are assumed to be involved in this flare: a low-lying loop, as indicated in the 6-10 keV images, which produces the bright emission between the two footpoints and a higher flare loop that contains the HXR looptop source shown in the images in the energy bands between 10 and 50 keV. Except for the HXR looptop source, the higher loop itself does not appear in the images. This could be due to weak thermal emission from the loop and/or the limited dynamic range of these images. However, the higher flare loop can be identified in SOHO/Extreme Ultraviolet Imaging Telescope (EIT) 195 Å images as shown in Fig. 2.7, albeit some 15 min. later.

It is well known that for Fourier-transform imaging, as used with RHESSI (Hurford et al., 2002), the existence of bright sources will make weaker sources in the same field of view harder to see against the background from the stronger sources. Because the HXR looptop source in this event is much weaker than the footpoints, even at the peak of the flare, the limited dynamic range ($\sim$20:1 with the present calibration), defined by Hurford et al. (2002) as the ratio of the surface brightness of the strongest source to the weakest

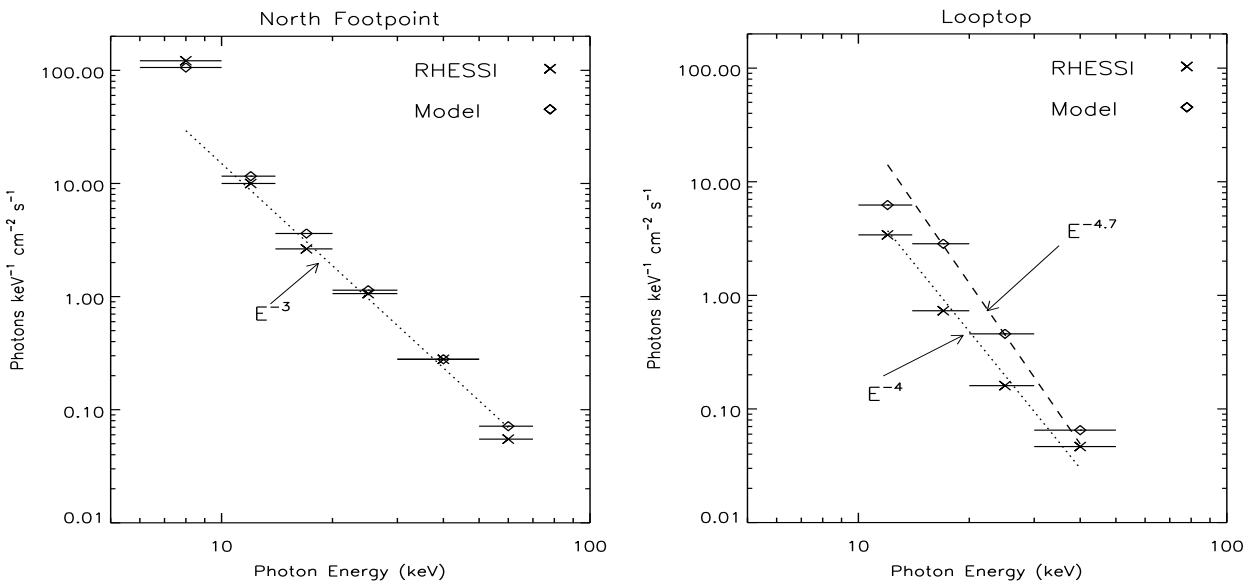

Figure 2.8: Spectra for the north footpoint (left panel) and looptop (right panel). The horizontal bars marked with an "x" are from the CLEAN images shown in Fig. 2.6. The bars marked with a diamond are from the model images reconstructed with CLEAN (Fig. 2.12).

credible source in the field of view, makes the looptop source difficult detect.

In an attempt to enhance the HXR looptop source relative to the bright loop, a RHESSI 20-30 keV CLEAN image at the peak was constructed with a shorter integration time of 4.3s (one RHESSI spin period) vs. the 13s (3 spin periods) used in Fig. 2.5 and 2.6. In this image, shown in Fig. 2.7, the looptop source appears stronger than it does in Fig. 2.5 or 2.6. Evidently, the HXR looptop source in the RHESSI images is indeed located at the top of the higher flare loop seen in the EIT image.

Image Spectra

In order to obtain the spectral characteristics of the footpoint and looptop sources, I integrated the flux within an $8'' \times 8''$ box around each of the two footpoints and the looptop (see Fig. 2.5 and 2.6). In MEM-Sato images, the box size was chosen to encompass the most emission from each feature and avoid the inclusion of the background fluxes. The box size in CLEAN images was chosen to be the same as in MEM-Sato images.

I found the results from MEM-Sato and CLEAN to be the same. Spectra of the footpoints (left panel) and the looptop (right panel) obtained from the CLEAN maps are shown in Figure 2.8. Because the two footpoints have similar spectra, i.e., the power-law indices for the footpoints are about equal, only the spectra of the north footpoint and the looptop are plotted. The results from the data are shown as horizontal bars marked with an 'x'. The length of the bar indicates the width of the energy band. The bars marked with diamonds are from the flare model (see § 2.4.2).

The immediately apparent result from these spectra is that the looptop spectrum is softer than the footpoint spectra. Power-law fits to these spectra give a spectral index of

3.0 for the footpoints and 4.0 for the looptop. This difference of one in spectral index is consistent with a recent statistical analysis of limb flares observed with Yohkoh (Petrosian, Donaghy, & McTiernan, 2002). At 6–10 keV, the flux from the north footpoint is higher than the extrapolated power-law. This is presumably because the thermal source between the footpoints is closer to the north footpoint, and the thermal source contributes to the flux from the north footpoint in this energy band. Because the looptop source does not appear in the images at 50–70 keV, the spectral fitting does not include this energy band.

2.4 Modeling the Flare

I have created steady-state particle transport models based on the analysis of the flare on 2002 February 20. After getting images predicted by the flare model, I input them into the RHESSI simulation software[2] to reconstruct simulated images with the same parameters as those used for reconstructuring the RHESSI images. Finally, I made a comparison between the model-predicted images and spectra and the RHESSI observations.

2.4.1 Modeling and Simulation of the Flare

Establishment of the Electron Transport Model

Although the mechanism for particle acceleration is still unclear, it is generally accepted that the particles are accelerated above flare loops, and then propagate into the loops (e.g., Aschwanden et al., 1996). Although there appeared to be at least two loops involved in the flare, only the higher, larger loop contains the HXR looptop source. Therefore, the particles are believed to be transported down to the lower atmosphere along this higher loop.

In the model, I assume that electrons with a power-law energy distribution and an isotropic pitch-angle distribution are injected at the top of a single semicircular flare loop. The electron spatial and spectral distributions within the loop were obtained with a steady-state Fokker-Planck code (McTiernan, & Petrosian, 1990), which gave a solution for the electron density distribution $f(E, \mu, s)$ (e.g., McTiernan, & Petrosian, 1990):

$$\begin{aligned} \mu\frac{\partial\Phi}{\partial s} &- \frac{d\ln B}{2ds}\frac{\partial}{\partial\mu}[(1-\mu^2)\Phi] \\ &= \frac{1}{\beta^2}\frac{\partial}{\partial\varepsilon}\{[C+S\beta^3\gamma^2(1-\mu^2)]\Phi\} - \frac{S}{\beta\gamma}\frac{\partial}{\partial\mu}[\mu(1-\mu^2)\Phi] + \\ &\quad \frac{\zeta C}{\beta^4\gamma^2}\frac{\partial}{\partial\mu}[(1-\mu^2)\frac{\partial\Phi}{\partial\mu}] + \frac{\Sigma}{c\beta^2} \end{aligned} \tag{2.6}$$

where, $\Phi \equiv f/\beta, \gamma = \varepsilon + 1$ is the total energy, ε is electron kinetic energy in units of $m_e c^2$, and $\beta c = c(1 - 1/\gamma^2)^{1/2}$ is the electron velocity. B is the magnetic field strength, $\mu = \cos(\alpha), \alpha$ is the electron pitch angle, s is the depth along magnetic field line, and Σ

[2]see RHESSI online documentation: http://hessi.ssl.berkeley.edu/~cmj/hessi/doc.html and http://hesperia.gsfc.nasa.gov/rhessidatacenter/simulated_data.html

is the source term for the injected electrons. For a background plasma of fully ionized hydrogen, $\zeta = 1$. The collsional energy loss is given by the expression:

$$C = 4\pi r_0^2 n \ln\Lambda = 2 \times 10^{-13} \left[\frac{\ln\Lambda}{20}\right] \left[\frac{n}{10^{10} cm^{-3}}\right] cm^{-1} \tag{2.7}$$

where $r_0 = e^2/m_e c^2$ is the classic electron radius, n is the ambient proton or electron density, and $\ln\Lambda$ is the Coulomb logarithm. The code includes Coulomb scattering, energy losses, and magnetic mirroring. The HXR emissions from the coronal loop and footpoints were calculated using thin-target and thick-target bremsstrahlung radiation codes (the thin-target bremsstrahlung is radiation from electrons losing only a small fraction of their energy while interacting with ambient plasma). Hot plasma is assumed to fill the flare loop uniformly. I added a low-lying thermal source to account for the low-energy sources seen between the two footpoints.

The radius of the semicircular loop in the model is 17″, and the diameter of the magnetic tube is 4″. The plane of the loop must be rotated 53° from the plane of the sky to match the flare geometry in the RHESSI images. The density distribution of the nonthermal electrons injected at the looptop is determined by the fit to the spatially integrated photon spectrum (see Fig. 2.4). The nonthermal electron power-law spectral index is 4.4 between 15 keV and 100 keV and −5.5 above 100 keV, and the total electron density is 3.5×10^8 cm^{-3}. Because the low-energy cutoff cannot be determined uniquely from the spectral fitting (see discussion in § 5.1.1), I set the low-energy cutoff to 15 keV to minimize the total nonthermal electron energy while still giving a good spectral fit. The plasma density and temperature within the loop were taken as 3.5×10^{10} cm^{-3} and 10 MK, respectively. The loop would be too bright, i.e., would be seen with RHESSI, if its temperature were much greater than 10 MK at this density. Therefore, the temperature and emission measure are determined by the simulations to meet the two requirements: (1) the loop should not be bright enough to be seen with RHESSI; (2) the density must be large enough to produce the observed HXR looptop source.

Based on the simulations, I find that the magnetic mirroring has very little effect on the brightness of the HXR looptop source, in agreement with the results of Fletcher (1995). Therefore, the magnetic field is assumed to be uniform along the flare loop so as to eliminate magnetic mirroring and reduce the number of free parameters by one.

The thermal source between the footpoints is taken to be 20″ long, 4″ wide, and 4″ deep, and shifted 5″ toward the north footpoint from the center of the two footpoints. This configuration was chosen to provide images that agree with the RHESSI images. The plasma density and temperature of this thermal source were chosen to agree with the results of the spectral fit (see Figure 2.4), i.e., 1.4×10^{11} cm^{-3} and 15 MK.

Simulation steps

The simulation procedure consisted of the following steps:

(1) Running the Fokker-Planck code to get the steady-state electron distribution within the higher loop. The electron distribution is a function of energy, pitch angle, and location within the loop.

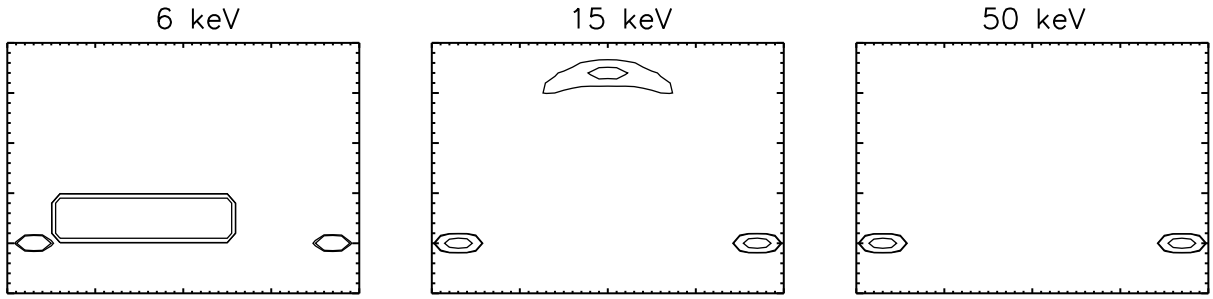

Figure 2.9: Model flare loop images at 6, 15 and 50 keV. Contour levels are 5, 7, and 50% of the peak flux in each image. The spatial resolution is 1″. These images are not rotated and scaled to the RHESSI images.

(2) Computing the photon fluxes along the 2D flare loop that would be seen for RHESSI. A thin-target bremsstrahlung code is used to compute the emissions from the flare loop, and a thick-target bremsstrahlung code is used to compute the emissions from the footpoints.

(3) Adding thermal bremsstrahlung fluxes from the low-lying thermal source to get the final model-predicted loop images.

(4) Running the RHESSI simulation software, with the final model-predicted images as input, to reconstruct the simulated flare images.

2.4.2 Modeling Results

Model-Predicted Images and Imaging Spectra

The model-predicted images (from step 3 of the simulation process listed above) at 6, 15 and 50 keV are shown in Figure 2.9. These images are shown with one arcsecond spatial resolution. At 6 keV, the thermal source between the two footpoints is very strong compared to the footpoints and the looptop source. The higher loop is nearly invisible at this energy. At 15 keV, the low-lying thermal source between the footpoints disappears, while the looptop and footpoint sources are visible. Only the two footpoint sources are visible at 50 keV.

Looptop and footpoint spectra from the model are plotted in Figure 2.8. The footpoint fluxes are obtained by summing over all pixels that show emission from one footpoint. The looptop fluxes are obtained by summing over 32 pixels at the top of the model loop. The thermal emission at low energies (dotted curve) is from the higher loop, not the low-lying thermal source between the footpoints. The spectral index of the footpoints is 3.1 between 15 keV and 56 keV, and 4.4 above 56 keV (shown in Fig. 2.10). The spectral index of the looptop is 5.0 between 15 keV and 56 keV, and 5.7 above 56 keV. Comparing the model spectra with the data, the spectral index of the footpoints from the model below 56 keV agrees with the estimated index, 3, from the RHESSI imaging spectra. The spectrum of the looptop is steeper than the value of 4 estimated from the data by $\sim$1, however.

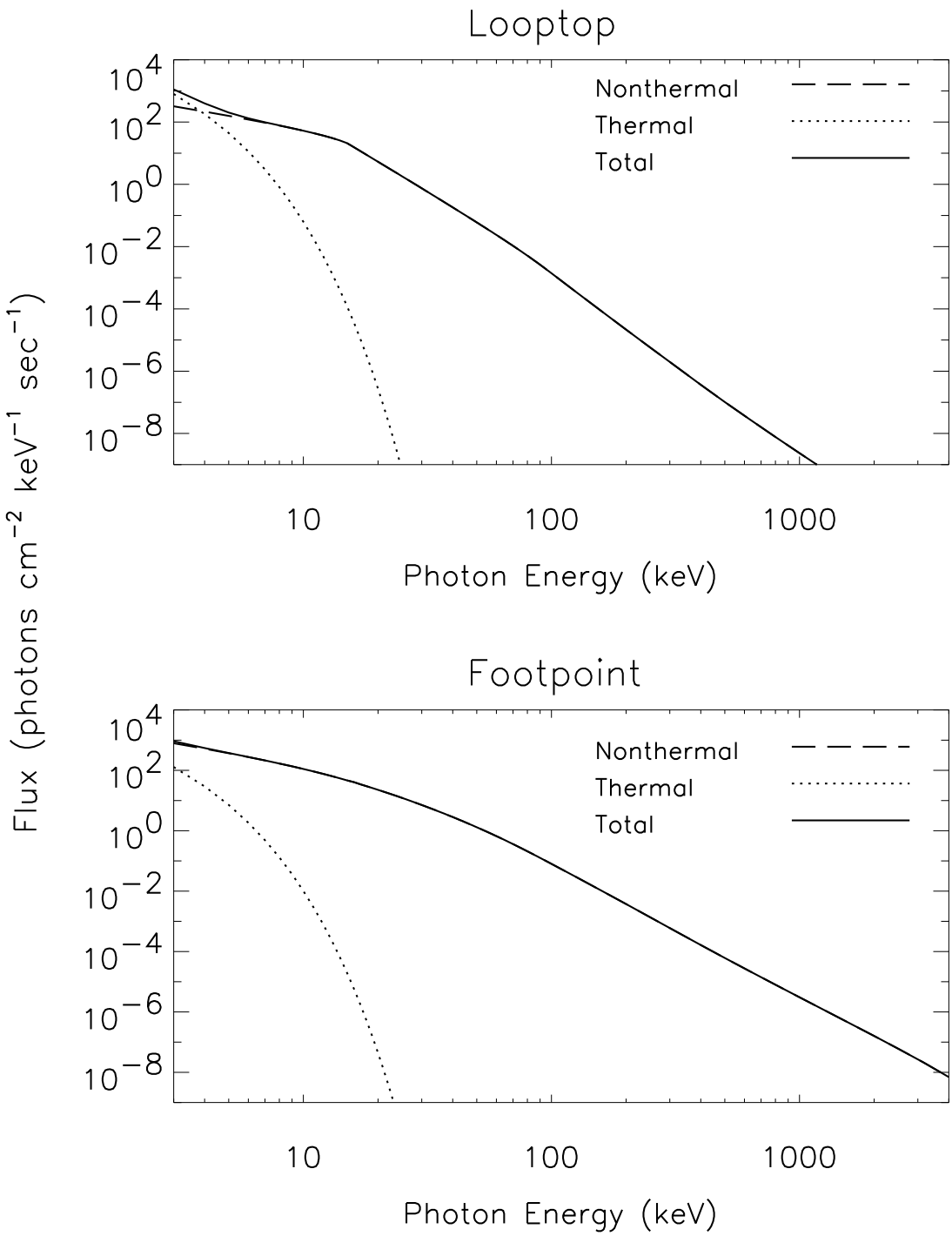

Figure 2.10: Spectra from the model images. The top panel shows the spectrum from the looptop and the bottom panel shows the spectrum from a footpoint. The dashed curve is the total nonthermal bremsstrahlung, the dotted curve is the thermal bremsstrahlung, and the solid curve is the total spectrum.

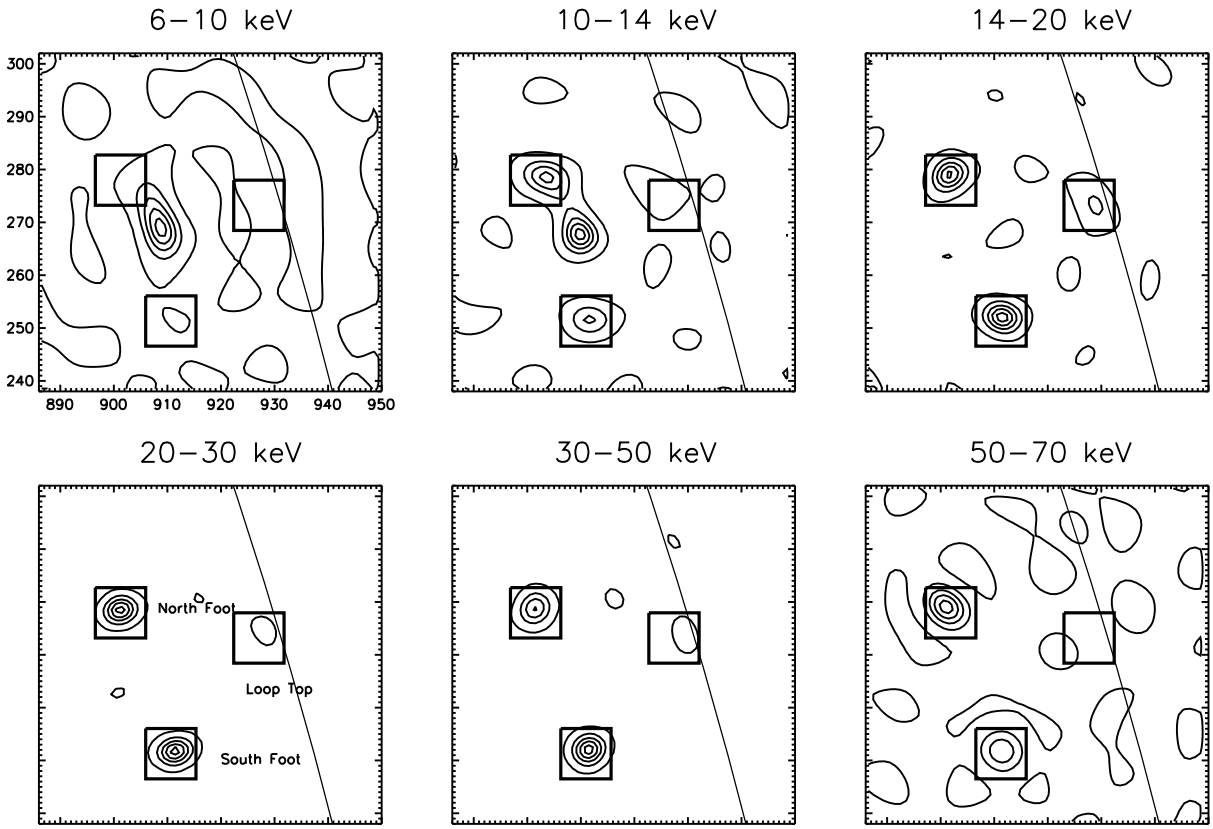

Figure 2.11: MEM-Sato images of the model flare loop for 6 energy bands. Contour levels are 0.1, 0.3, 0.5, 0.7, and 0.9. The contours are normalized to the peak flux of each image. The solid line indicates the solar limb.

Simulated images and imaged spectra

I input each model image as a 64×64 array into the imaging software. All imaging parameters are the same as those used for the RHESSI images. As shown in Figures 2.11 and 2.12, the simulated MEM-Sato and CLEAN images roughly agree with the images in Figures 2.5 and 2.6. At 6–10 keV, only the thermal source between the two footpoints is visible. At 10–14 keV, the thermal source still dominates. Note that in the MEM-Sato images, the uniform thermal source appears to be a double source. There is a weak looptop source visible in both the MEM-Sato and CLEAN images. At 14–20, 20–30 and 30–50 keV, two clear footpoints and a looptop source are visible. This also agrees with the RHESSI images. At 50–70 keV, the looptop source is not apparent, and only the two footpoints are still visible.

Spectra obtained from the simulated images based on the model are shown in Figure 2.8 along with the spectra obtained from the RHESSI flare images. Lacking error bars for the fluxes deduced from the RHESSI images, I do not yet have a meaningful, quantitative test of goodness of fit. Nevertheless, the footpoint spectrum can be seen to be closely reproduced by the model. The looptop spectrum, on the other hand, is poorly reproduced. The model spectrum is too steep relative to the flare data. The looptop spectrum for the RHESSI data has a power-law spectral index of about 4, while the spec-

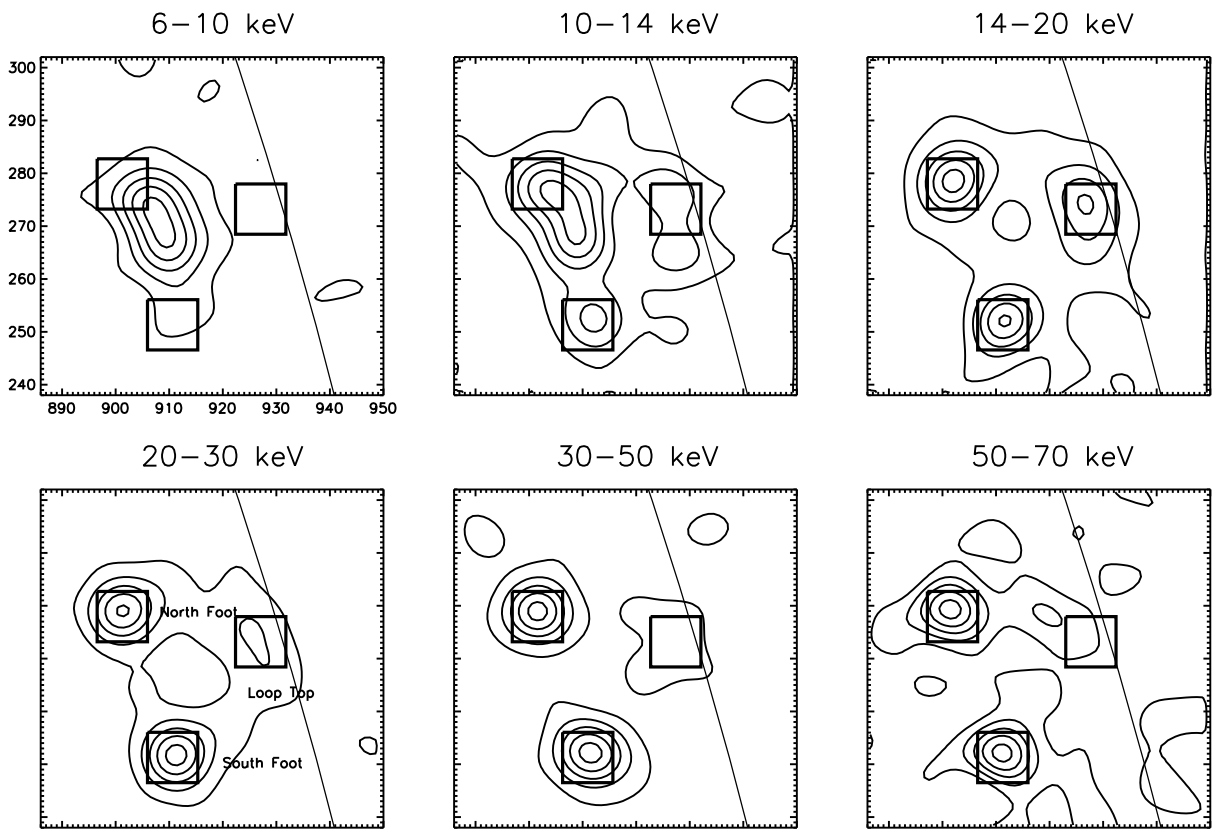

Figure 2.12: CLEAN images of the model flare loop. Contour levels are the same as in Fig. 2.11.

tral index of the model (15 keV to 50 keV) is about 4.7. Notice that the model-predicted looptop index, 4.7, obtained from the simulated images is flatter than the looptop power-law index between 15 and 56 keV, 5.0, obtained directly from the model (see Fig. 2.10). This difference is caused by the energy binning process (i.e., binning every 1 keV model-predicted images into the images with the same energy bands as RHESSI images).

Figure 2.8 shows that the looptop flux from the model is too high at low energies. The flux at, say, 14–20 keV could be brought into agreement with the flux from the flare by decreasing the plasma density in the loop. If this were done, however, the looptop source would be too weak at higher energies and would not be visible in the simulated images. I have not found a way to rectify this problem without significantly changing the physical model.

RHESSI Imaging Software Test With Simulations

The simulations can be used not only to test flare models, but also to check the imaging software itself to identify possible artifacts from the image reconstruction process. With this simple simulation process, I have found that both the MEM-Sato and the CLEAN imaging algorithms can alter the relative brightness of the flare components. An example of this is shown in Figure 2.13. An unprocessed image from the model is shown in the top left panel. This 14–20 keV model image was not used in simulating the RHESSI data because the looptop is too bright. The same images processed with MEM-Sato and with CLEAN are shown in the bottom left and bottom right panels. It was processed in the same way as the other images, including only grids 3 through 8. The upper right panel shows the model image smoothed with a conical response function having a full width at half maximum FWHM of 7″. This simulates the lower resolution of the processed images. In the unprocessed image, the peak flux from each footpoint is about 2 times higher than that from the looptop. In the other three images, however, the peak flux of the looptop is about 2 times higher than that of the footpoints. This is because the looptop source is more extended than the footpoints, and the spatial averaging at the lower spatial resolution picks up flux from many pixels in the looptop while the footpoint emission originates from only a few pixels.

As is the case for the unprocessed model image, the north and the south footpoints have about the same peak flux in the smoothed and the CLEAN images. In the MEM-Sato image, however, the peak flux from the north footpoint is 30% higher than that from the south footpoint. For all the images, however, the integrated flux from the north footpoint is about the same as the integrated flux from the south footpoint. MEM-Sato has super-resolved the X-ray sources — they are more compact than the spatial resolution of the instrument. On the other hand, compared to the smoothed image, CLEAN has enhanced the emission from the southern leg of the loop relative to the peak flux from the footpoints by about 130%. Fortunately most of these discrepancies are relatively small, but they are impossible to recognize in RHESSI images without comparing them to model images.

Figure 2.14 shows a simulated image from the model processed with MEM-Sato on the left (Fig. 2.11, 14–20 keV) and the corresponding MEM-Sato flare image on the right (Fig. 2.5, 14–20 keV). For clarity, an additional low-flux contour (5%) has been added to

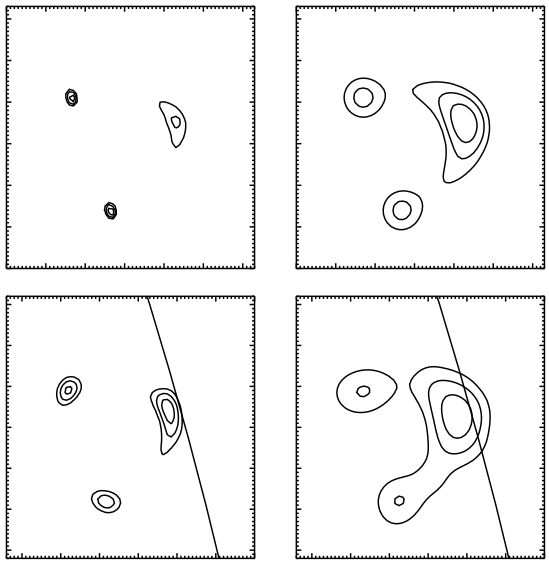

Figure 2.13: An unprocessed image from the flare model (top left), the same image convolved with a 7″ FWHM conical response function (top right), the same image processed with MEM-Sato (bottom left), and the image processed with CLEAN (bottom right) are shown. Contour levels are 20, 40, and 70% of the peak flux in each image. The scale and pixel size are the same as used in Fig. 2.5.

the RHESSI map from Figure 2.5. Some artificial sources appear in the simulated image. Comparing the simulated MEM-Sato image with the RHESSI MEM-Sato image, similar patterns can be seen in both images. Because the sources between the footpoints and coronal source in the simulated image are not in the model, they must be produced by the imaging process itself. Consequently, the "sources" between the footpoints and the coronal source in the RHESSI flare image cannot be taken as real.

To compare the photometric accuracy of spectra and images in flares observed with RHESSI, Aschwanden et al. (2004) tested the accuracy of the photometry by comparing the photon fluxes obtained from the spectral-fitting software (SPEX, Smith et al., 2002) with those fluxes contained in the images reconstructed with different RHESSI image algorithms (Hurford et al., 2002), and found that the CLEAN, PIXON, and FORWARD-FIT (Aschwanden et al., 2002) algorithms have a robust convergence behavior and a photometric accuracy on the order of a few percent, while MEM-Sato does not converge optimally for large degrees of freedom (for a large field of view and/or small pixel size).

2.5 Summary and Discussion

In the steady-state particle transport model, the looptop and footpoint nonthermal X-ray sources arise from the injection of suprathermal electrons at the top of a magnetic loop. The lower energy electrons in the injected particle distribution interact with the plasma inside the flare loops to produce the HXR looptop source, while the footpoint sources are produced when the particles reach the high-density lower corona or chromosphere.

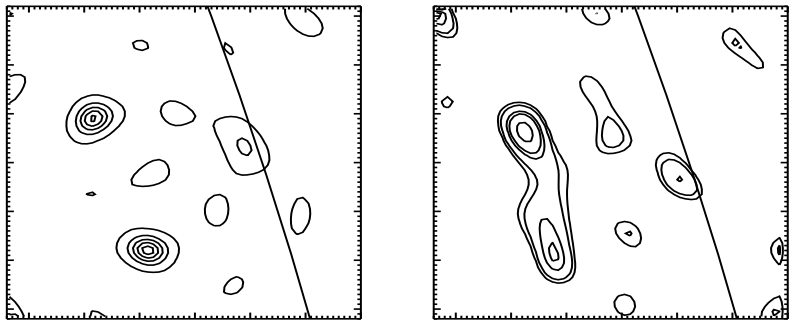

Figure 2.14: MEM-Sato 14–20 keV images of the model (left) and of the observed flare (right). The scale and pixel size are the same as used in Fig. 2.5. I can see similar patterns in them. The sources between the looptop and footpoints in the left image are not real. Consequently, I deduce that sources between the footpoints and the looptop in the right image are also not real.

Although the simulated images from the model roughly agreed with the flare images, the spectrum of the looptop source from the model is steeper than that from RHESSI observations. Therefore, the simulation results indicate that the model applied here does not adequately describe the HXR looptop emission from the 20 February 2002 flare.

A significant handicap I faced for this analysis was the lack of knowledge of the uncertainties in the fluxes obtained from the RHESSI images. Without the knowledge of these uncertainties, I could not properly evaluate the ability of the model to fit the imaged spectra. My future work will include a careful evaluation of the imaging and simulation processes to establish a realistic estimate of these uncertainties.

Here I applied the model to only one event. Future work will include application of the model to more events observed with RHESSI. However, the statistical analysis of looptop sources observed with Yohkoh (Petrosian, Donaghy, & McTiernan, 2002) indicate that the looptop spectra are, on average, steeper than the footpoint spectra by 1, not 1.7 as my model predicts. Therefore, the particle transport model being proposed here may not be able to explain the HXR looptop sources in general. Other particle injection and propagation models that include a density enhancement (Wheatland & Melrose, 1995) or magnetic trapping (Fletcher & Martens, 1998) at the top of the loop are likely to suffer the same problem with the looptop spectrum as the model applied here.

To produce a HXR looptop source with a flatter spectrum, a new model should allow a flatter electron spectrum than the current model offers. One likely solution is that suprathermal electrons are accelerated in the looptop region, rather than injected into the loop after being accelerated above it. Thus, the acceleration process will interfere with particle transport so that low-energy electrons escape from the looptop region faster than the current transport model predicts. As a result, the electron spectrum in the looptop region will be flatter. Petrosian & Liu (2004) studied a stochastic acceleration model, in which the magnetic reconnection generates plasma wave turbulence in the looptop region. Instead of being accelerated above the loop and then injected into it, the particles are believed to be accelerated by the turbulence in the looptop region and then transported down to loop footpoints. Without including the particle transport effect within the flare

loop and RHESSI instrument response, Petrosian & Liu (2004) found that, in general, looptop spectra are steeper than the footpoints spectra. In this stochastic acceleration model, low-frequency waves preferentially accelerate high-energy electrons, while high-frequency waves accelerate low-energy electrons. If a turbulent wave spectrum is very steep, scattering of high-energy particles would be more efficient than low-energy electrons. Then the escape of the low-energy electrons becomes more efficient relative to the high-energy electrons, thereby a flatter electron spectrum could be obtained at the looptop for a given footpoint spectrum. At present, the creation of these waves and their interaction with particles are not fully understood.

Another question worth considering is whether or not all the observed HXR looptop sources are produced by the same mechanism. Earlier observations with Yohkoh and recent observations with RHESSI all indicate that the shape, location, and intensity of HXR looptop sources vary from event to event. In the 'Masuda flare' (Masuda et al., 1994), the looptop source was apparently located ($\sim$10″) above the SXR flare loop, and the shape of the source is cusp-like (see Fig. 2.1). It is the only HXR cusp-shaped looptop source ever observed. Masuda et al. (1995) reported another two flares, however, showing more rounded HXR looptop sources (see Fig. 6 and 10 of Masuda et al., 1995). For those two looptop sources, one appeared to be located at the top of the SXR loop, while the location of the other looptop source relative to the SXR loop was difficult to identify because no SXR loop was observed. The looptop sources presented in this thesis (Fig. 2.6 of this chapter, and three other flares discussed later as shown in Figs. 3.9, 3.17, 4.1) also all have a rounded shape. The looptop source in the 2002 February 20 flare is weaker than the footpoints. However, the looptop sources in 2002 April 14 and 16 are much stronger than the footpoints. Are these differences caused by the same mechanism but with different coronal conditions (e.g., plasma density) or caused by different mechanisms? More modeling needs to be carried out in future studies to answer these questions.

Chapter 3

Evidence for the Existence of a Current Sheet

3.1 Review of the Standard Flare Model

3.1.1 Magnetic Reconnection in a Current Sheet

As discussed in Chapter 1, magnetic reconnection is thought to be the cause of the primary energy release in flares. It is envisaged that a volume of coronal plasma with magnetic field lines in one direction is brought into close contact with another such volume with magnetic field lines in the opposite direction. Such a field configuration is far from 'potential' ($\bigtriangledown \times B \neq 0$), and in fact can exist only if there is an associated current located along the boundary between the two volumes in a direction perpendicular to the field lines. The boundary region is, for this reason, called a current sheet. When the magnetic fields associated with the current reconnect, part of the magnetic energy is converted to heat the ambient plasma and accelerate particles. For classic resistivity, i.e., resistivity caused solely by collisions, a temperature of 10^7 K in the solar corona with a plasma density of 10^9 cm^{-3}, the current sheet can be only a few hundred meters in thickness (Holman, 1985). Even with 'anomalous' resistivity (Syrovatskii, 1972), such as caused by the presence of plasma waves or turbulence, the width of the current sheet is probably only on the order of a kilometer. This is far smaller than the observational limits of present-day imaging instruments (1 arcsecond at 1 AU corresponds to ∼725 km on the Sun).

The first quantitative model of magnetic reconnection was propose by Sweet (1958) and Parker (1957). The current sheet geometry in the Sweet-Parker model is shown in Figure 3.1, where it is assumed that the length of the diffusion region ($2L$) is much larger than the width ($2l$). In the diffusion region, the plasma inflow (with velocity v_i) creates an outflow (with velocity v_o) along the current sheet. Based on normal Spitzer resistivity (Spitzer, 1962), the Sweet-Parker reconnection model leads to the release of magnetic energy over a period of time that is several orders of magnitude longer than the observed energy release time in solar flares. Petschek (1964) proposed that magnetic reconnection can be speeded up by reducing the length of the diffusion region to be the same as the width (i.e., $L \sim l$, see Fig. 3.2). Because the length of the current sheet is much shorter, the propagation time through the diffusion region is short and the reconnection process

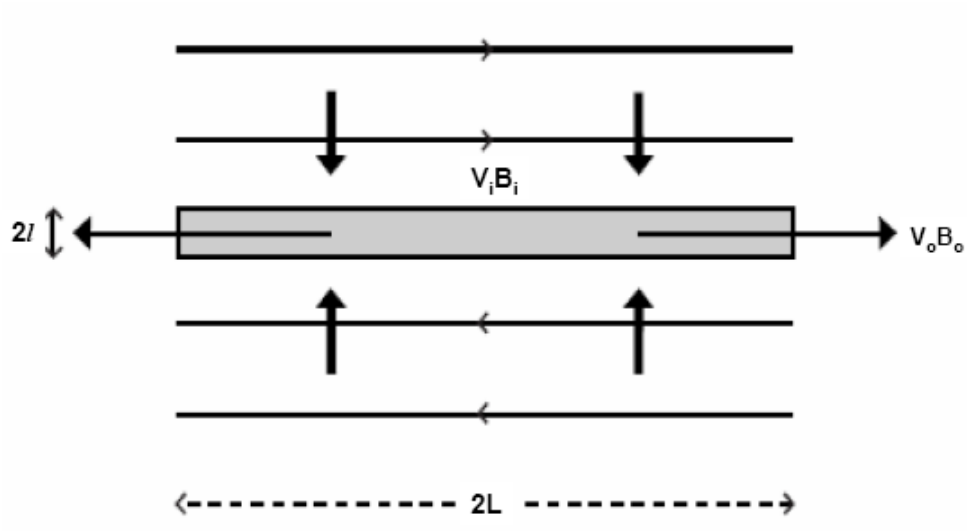

Figure 3.1: Cartoon of the Sweet-Parker magnetic reconnection model (Sweet, 1958; Parker, 1957). The figure is adapted from Priest & Forbes (2002).

speeds up. In the Petschek reconnection model, two slow mode shocks stand in the flow on either side of the interface, marking the boundaries of the plasma outflow region. Summaries of the Sweet-Parker and Petschek models can be found in Priest & Forbes (2000).

Recent studies indicate that the initially closed magnetic field does not necessarily become fully open as suggested in the Kopp-Pneuman model (see Fig. 1.5) (e.g., Forbes & Priest, 1995; Antiochos, 1998; Uchida et al., 1999). Instead, the magnetic structure is thought to be highly stretched by the eruption of a flux rope, below which a current sheet forms (e.g., Forbes & Priest, 1995). With dissipation in the current sheet, the stretched magnetic field lines start to reconnect, producing closed field lines below the current sheet. Figure 3.3 illustrates the 2D flux rope model developed by Forbes & Priest (1995) and Lin & Forbes (2000). Forbes & Priest (1995) proposed that converging photospheric flow or flux emergence leads to the formation of a sheared arcade field containing a flux rope (note that the flux rope pre-exists before eruptions, in order to create such flux ropes, a 3D magnetic reconnection, such as proposed by Gosling et al. (1995), may be required). Two photospheric field sources of opposite polarity approach each other until a catastrophe point is reached and the flux rope erupts. The eruption drives reconnection in a current sheet below the flux rope. The model predicts a continuous rise of the Y-type reconnection points at each end of the current sheet. One of the most significant predictions of the flux rope model is that a current sheet develops following the onset of the eruption. There is some possible observational evidence for such current sheets followed by erupting CMEs (Ciaravella et al., 2002; Ko et al., 2003; Webb et al., 2003; Lin et al., 2005). However, it has been difficult to obtain direct observations of the formation and evolution of a current sheet in a flare.

The previous observations, e.g., cusp-shaped soft X-ray flare loops (Tsuneta et al., 1992; Tsuneta, 1996), high temperature plasma along the field lines mapping to the tip

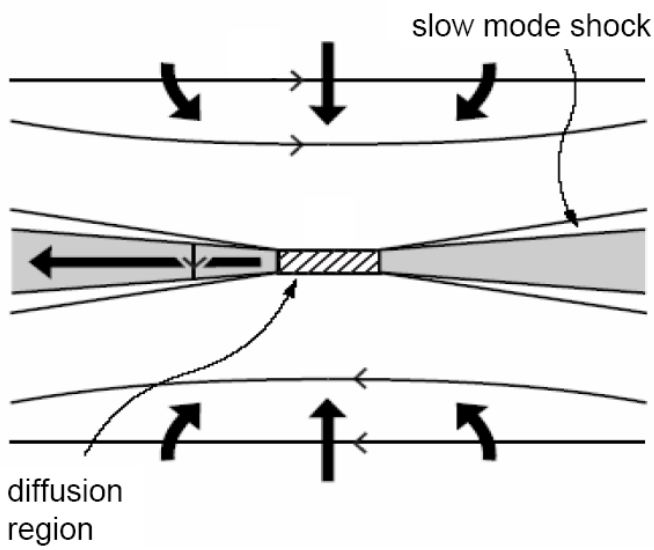

Figure 3.2: Cartoon of the Petscheck reconnection model (Petschek, 1964). The figure is adapted from Priest & Forbes (2002).

of the cusp (Moore et al., 1980; Švestka et al., 1987; Tsuneta, 1996), and a HXR source located above the soft X-ray loops (Masuda et al., 1994), undoubtedly suggest that the lower tip of the current sheet should be located somewhere at or above the top of the flare loops. However, observations related to the location of the upper end of the current sheet are very rare. Outward moving coronal sources above flare loops have been observed with Yohkoh/SXT in several events (Shibata et al., 1995; Ohyama & Shibata, 1998). One striking event on 1992 October 5, reported by Ohyama & Shibata (1998), showed a plasma blob above a flare loop (see Fig. 3.4). The long-exposure SXT images revealed that the plasma blob was penetrated by, or connected to, the top of a large-scale loop. This seemed to suggest that the plasma blobs observed above the flare loops may well have been part of a large-scale loop with its two ends anchored on the Sun, as predicted by Shibata et al. (1995) (see Fig. 1.6). Tsuneta et al. (1997) reported another event showing the rise of a loop structure about 10 minutes before the flare, which later evolved into a plasmoid. Moreover, a Yohkoh/SXT temperature map of this event showed a compact hot source, which coincided in position with the plasmoid and slowly moved upwards. This compact source was interpreted as plasma heated at a fast-mode shock due to the collision of the upward fast outflow from the X-point with quasi-stationary reconnecting field lines. These observations suggest that the upper end of the current sheet might be below the plasma blob.

3.1.2 Tearing-Mode Instability

Furth et al. (1963) showed that a current sheet can be unstable to a process that significantly increases the rate of magnetic reconnection, the tearing-mode instability. Such unsteady magnetic reconnections are better able to explain the bursty and intermittent pulses (on time scales of seconds or subseconds) of particle acceleration seen in HXRs and

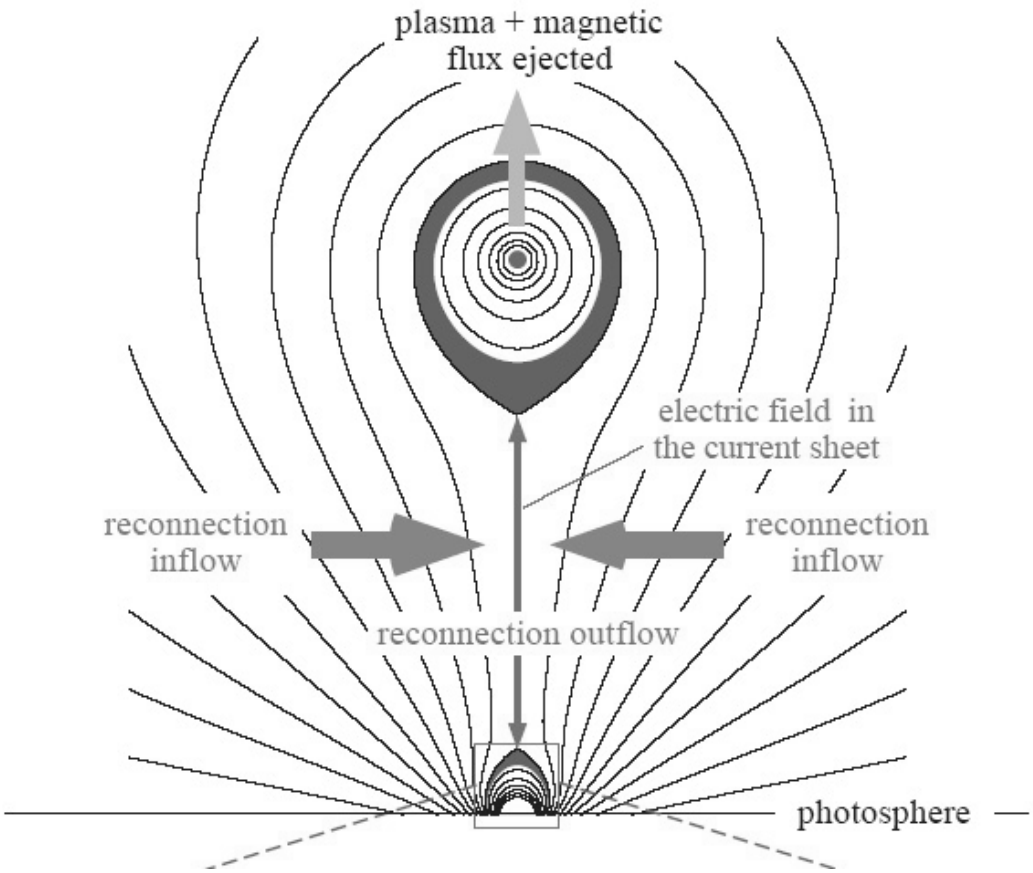

Figure 3.3: A sketch of the flux rope/CME model of Forbes & Priest (1995) showing the eruption of the flux rope, the current sheet formed behind it, and flare loops below (from Lin & Forbes, 2000).

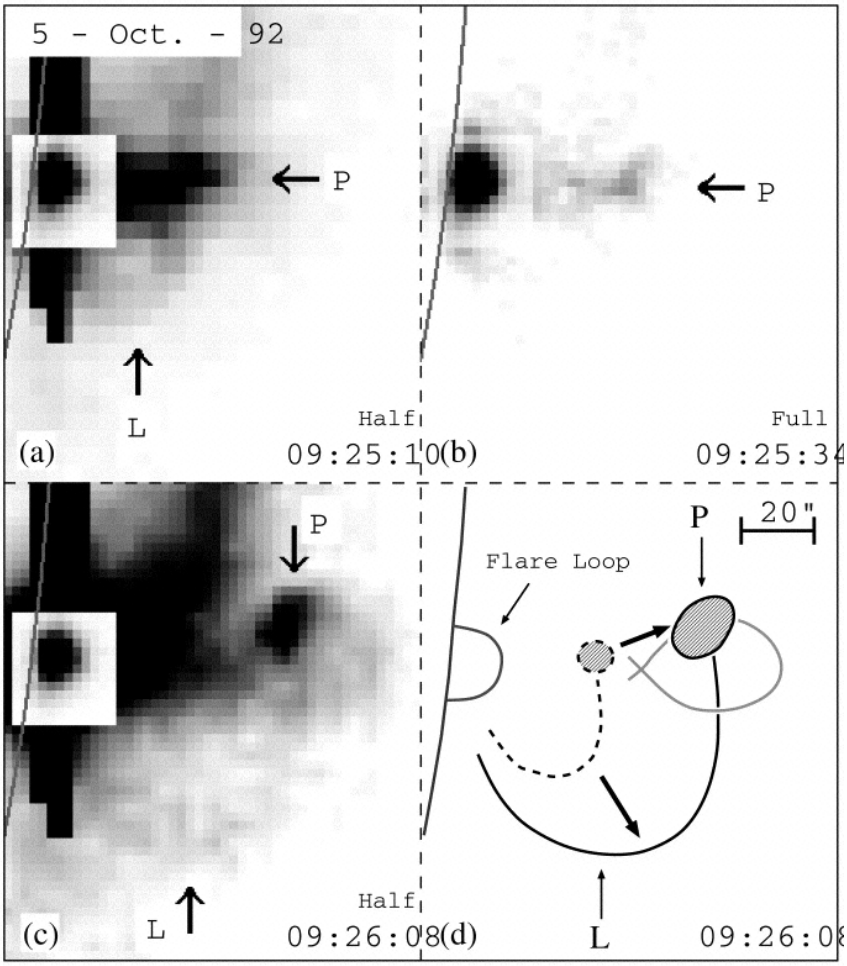

Figure 3.4: Sequence of Yohkoh/SXT images of the flare on 1992 October 5 (from Ohyama & Shibata, 1998). The ejected loop and plasmoid features are indicated by L and P, respectively. The curves indicate the solar limb. (a) Half-resolution (5 pixel) image at 09:25:10 UT (78 ms exposure). (b) Full-resolution image at 09:25:34 UT (2.9 ms exposure). (c) Half-resolution image at 09:26:08 UT (38 ms exposure). (d) Schematic picture of (c). The dashed curves indicate the plasmoid and expanding loop at 09:25:10 UT.

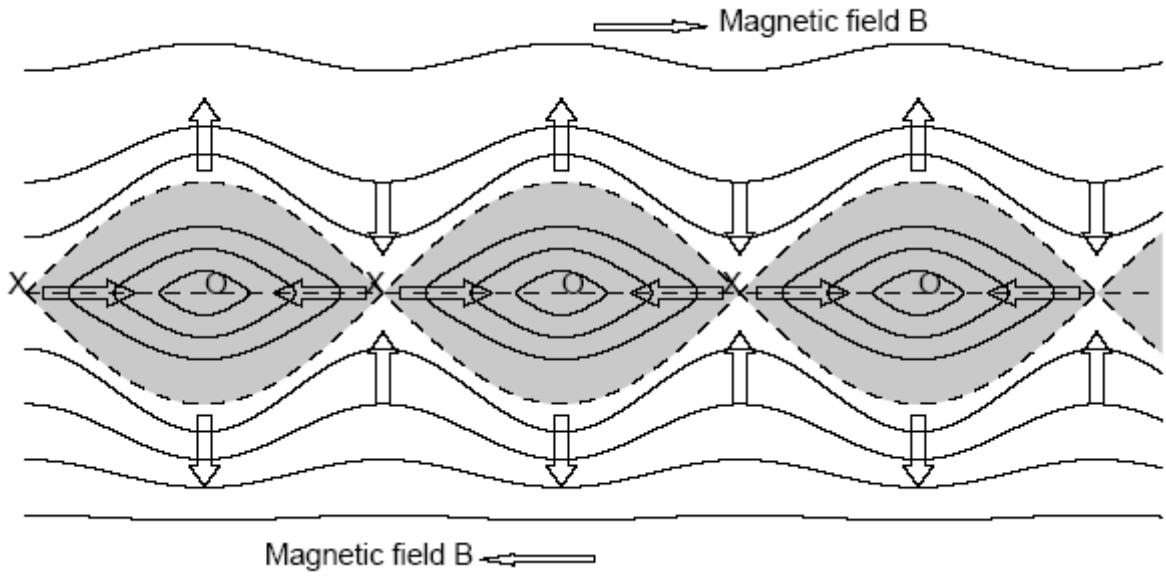

Figure 3.5: Magnetic island formation by the tearing-mode instability in a magnetic reconnection region. Magnetic neutral X and O points are formed at the boundary between regions of oppositely directed magnetic fields (from Aschwanden, 2002).

radio wavelengths (Aschwanden, 2002). Furth et al. (1963) also predicted that a current sheet will become unstable to the tearing-mode after its length (see Fig. 3.1) exceeds about 2π times its width (i.e., $L \geq \pi l$). As described by Phillips (1992), in the tearing-mode instability, two regions with oppositely directed magnetic fields are not pushed together, as in the Sweet-Parker (Sweet, 1958; Parker, 1957) and Petscheck (Petschek, 1964) mechanisms, but reconnection is spontaneous. Plasma is driven towards these points in the current sheet by non-uniformities in the field outside the sheet. An X-shaped neutral point develops and the sheet tears. It does so repeatedly along the length of the sheet, forming magnetic 'islands' that contain separate strands of current (see Fig. 3.5). This linear phase of the tearing-mode instability does not seem to provide enough energy for flares, but the non-linear development of the instability, in which the magnetic islands coalesce, results in a much greater energy release rate. It, thereby, shows greater promise for explaining flares (see review by Priest & Forbes, 2000). Signatures of the tearing mode have been seen in Tokomaks.

3.1.3 Flare Loop with a Cusp Structure

The "cusp", the pointed top of a bright loop (see Fig. 3.6), has become almost a Yohkoh emblem (Martens, 2003), because it was first clearly observed with SXT (Tsuneta et al., 1992). These cusp structures are quiet similar to the magnetic field configuration suggested by the standard models for two-ribbon flares (Carmichael, 1964; Sturrock, 1966; Hirayama, 1974; Kopp & Pneuman, 1976). The pointed tip of the cusp is interpreted as the remnant of a kink in the reconnected field lines. The existence of the cusp geometry is

Figure 3.6: Soft X-ray image of a flare on 1999 March 18 showing a cusp-shaped loop (from Martens, 2003).

direct evidence for current sheet formation in the corona (Hudson & Ryan, 1995). Of crucial importance is that the cusp, especially its outer boundary, has a higher temperature than the other portions inside the loop, and that successive loops are formed at higher altitude with more separated footpoints. This observation further supports flare energy being supplied by an ongoing reconnection process near the top of the loop (Tsuneta et al., 1992).

3.2 Evidence for Current Sheets in RHESSI Observations

The period from 14 to 21 April 2002 was a time of moderate to high solar activity, due mainly to the transit across the disk of three large active regions: AR9901, AR9906 and AR9907 (Gallagher et al., 2002). RHESSI observed three flares (GOES M3.7, M1.2, and M2.5) in the same active region (AR9901) on 2002 April 14-15, 15 and 16, as it approached the northwest limb. All three flares occurred within $\sim 10''$ in latitude and $\sim 30''$ in longitude of one another after allowing for solar rotation. They are homologous in morphological appearance and have similar light curves (see Fig. 3.7). The 25-50 keV HXR fluxes in all three flares increased abruptly at the start of the impulsive phases and decayed gradually later in the flares. The impulsive phases all had multiple HXR peaks and lasted about 6–16 min.

In this section, I will present the RHESSI observations of the two flares on 2002 April 15 and 16 that strongly suggest the existence of a large-scale current sheet above the flare loops. Analysis of the 2002 April 14-15 flare is presented in Chapter 4.

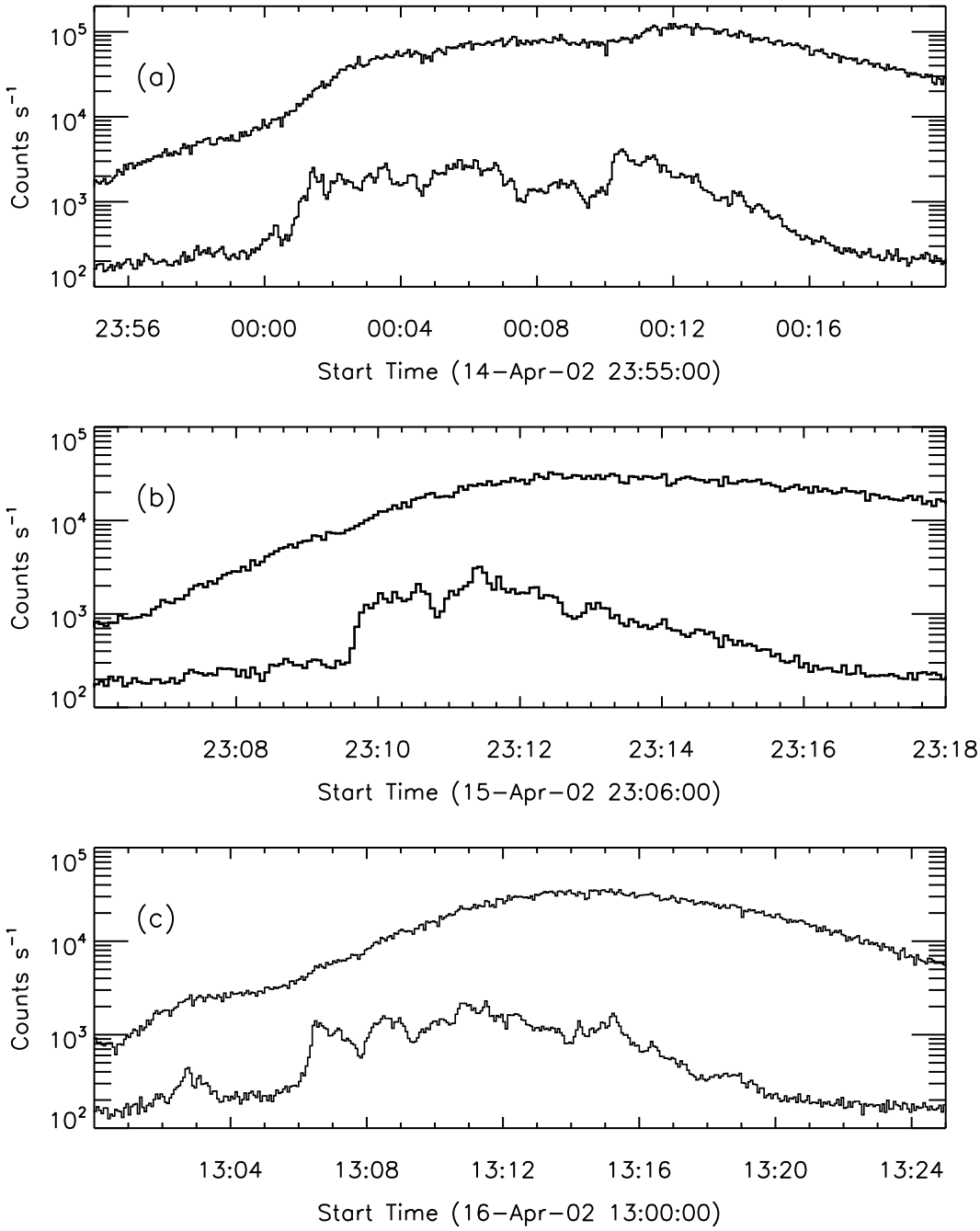

Figure 3.7: RHESSI light curves of the three flares. Panels (a), (b), and (c) show the light curves of the April 14-15, 15, and 16 flares, respectively. The energy bands in each panel are 6-12 (upper curve) and 25-50 keV (lower curve). Time resolution is 4 s. The RHESSI thin attenuators were in for all three events.

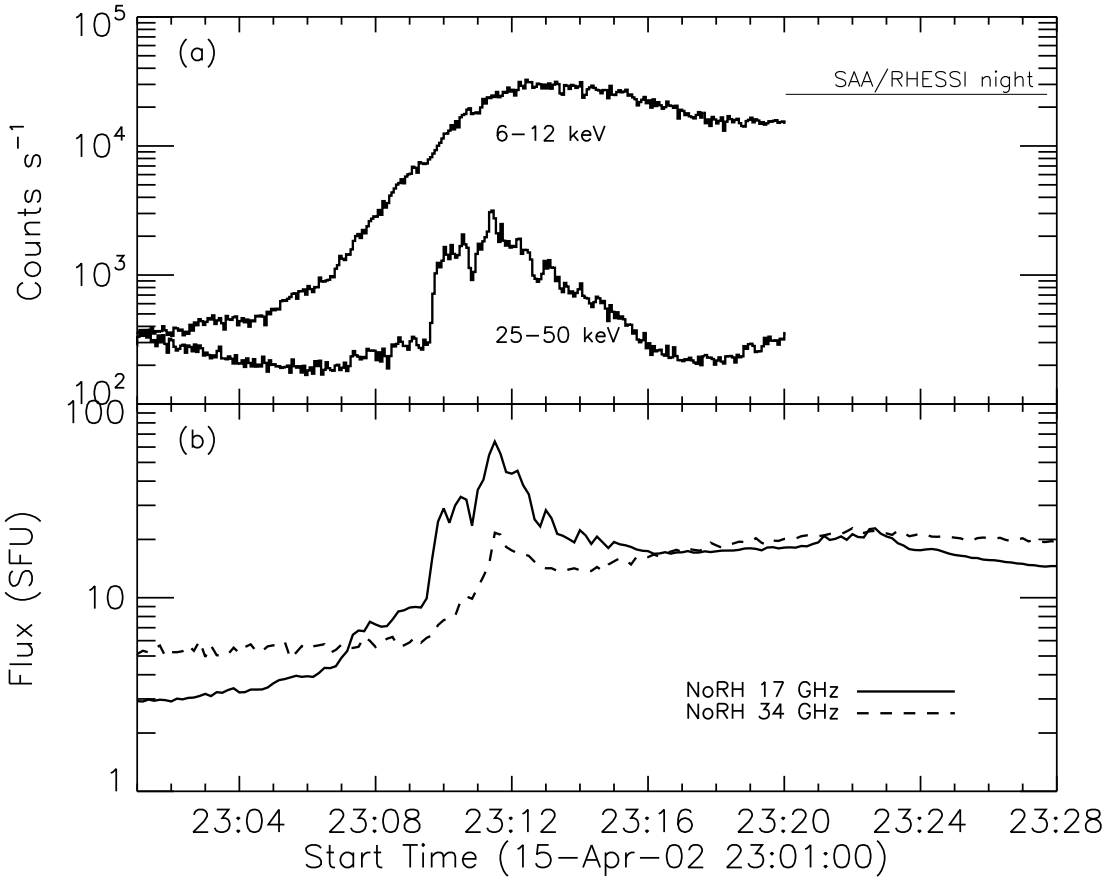

Figure 3.8: Light curves for the April 15 flare. Panel (a) shows the RHESSI light curves in two energy bands (same as Fig. 3.7b). Panel (b) shows the time profiles of the NoRH microwave light curves at two frequencies.

3.2.1 RHESSI Observations of the 2002 April 15 Flare

RHESSI images

RHESSI X-ray light curves in two energy bands are shown in Figure 3.7(b) and 3.8(a). The flare had a typical gradual rise and fall in SXRs. The HXR flux (>25 keV) increased abruptly at 23:09:40 UT, then decayed more slowly after the major peak at 23:11:26 UT.

A time sequence of RHESSI 10-20 keV images is shown in Fig. 3.9. The images show emission from a flare loop with its northern leg longer than the southern one. Besides the flare loop, there is a coronal source above the loop, which appears to be connected to the looptop in the rise phase of the flare (first two panels in Fig. 3.9). The coronal source then separated from the flare loop at the start of the impulsive phase at 23:09:40 UT. It stayed stationary for about 2 minute without obvious motion until the peak of the flare at 23:11:26 UT, after which it moved outward. The speed obtained from the centroid of the coronal source in images between 23:12:09–23:12:50 UT (panels in the bottom row of Fig. 3.9) is estimated to be 300 ± 30 km s^{-1}. The dotted line in the last panel of Figure 3.9, connecting the centroids of the coronal sources between 23:12:09–23:12:50 UT, represents the trajectory of the coronal source. More discussions of the motion of the coronal source,

along with the motion of the flare loop itself, is presented in Chapter 4.

There was a CME associated with this flare. As indicated by SOHO/LASCO C2 and C3 images (Fig. 3.10), a large coronal loop was seen propagating outward up to 16 $R_\odot$ at the same speed of $\sim$ 300 km s^{-1} as the RHESSI coronal source. Extrapolating forward in time from the RHESSI images with this velocity puts the coronal source at the inner edge of the coronal loop seen in the LASCO C2 image at 02:26:00 UT on 2002 April 16.

RHESSI images in nine different energy bands at the HXR peak (23:11-23:12 UT) are shown in Fig. 3.11. At lower energies (<20 keV), the images show the bright looptop. At higher energies (20-50 keV), the images show two footpoints and a bright looptop. They can be seen during the entire impulsive phase from 23:09:40 to 23:13 UT. Unlike the previously reported HXR looptop sources (e.g., Masuda et al., 1994, 1995; Petrosian, Donaghy, & McTiernan, 2002), the looptop source of this flare was always brighter than the two footpoints except at the major peak when the southern footpoint (indicated as 'SF' in the Fig. 3.11) was brighter. As indicated in Figure 3.9, the 25–30 keV HXR looptop source shown in the image at 23:11:06.75 UT is located at the upper part of the looptop region seen at 10–20 keV. The southern footpoint was always brighter than the northern footpoint ('NF' in Fig. 3.11). All the RHESSI observations indicate that a compact flare loop system was involved in the flare, in agreement with the TRACE 1600 Å observations of this event (Sui et al., 2005).

Temperature Distribution of the Loops

Because the RHESSI images consistently show a bright looptop, I use the centroid of the flux within the 60% contour to quantify the location of the looptop source. I define the "altitude" of the looptop centroid in the plane of the sky as the distance between the centroid of the looptop and the center of the line between the two footpoints. The footpoint locations are taken as the centroids of the footpoint sources at 25–30 keV. Figure 3.12 shows this looptop altitude at different energies (plus signs). It is evident that flare looptops at higher energies are located higher in altitude, suggesting hotter loops are located higher than cooler loops, in agreement with previous Yohkoh/SXT and RHESSI observations (Tsuneta et al., 1992; Tsuneta, 1996; Gallagher et al., 2002). These observations support the scenario of energy release above the flare loops. At any given time, the outer, higher loops just formed are filled with hot plasma, whereas the inner, lower, loops were formed earlier, and have cooled by radiation and conduction (Tsuneta, 1996). The apparent sudden increase of the loop height around 17 keV may be due to the displacement of the HXR looptop source from a region of predominately thermal emission to a region of predominantly nonthermal emission. On the other hand, it could be an artifact of the image reconstruction process.

Temperature Distribution of the Coronal Source

RHESSI images showing the coronal source above the loop in three energy bands are presented in Figure 3.13. To quantify the location of the coronal source, I first obtained its centroid in each energy band. The altitude of the coronal source centroid, defined in the same way as the altitude of the looptop source, is also plotted in three energy

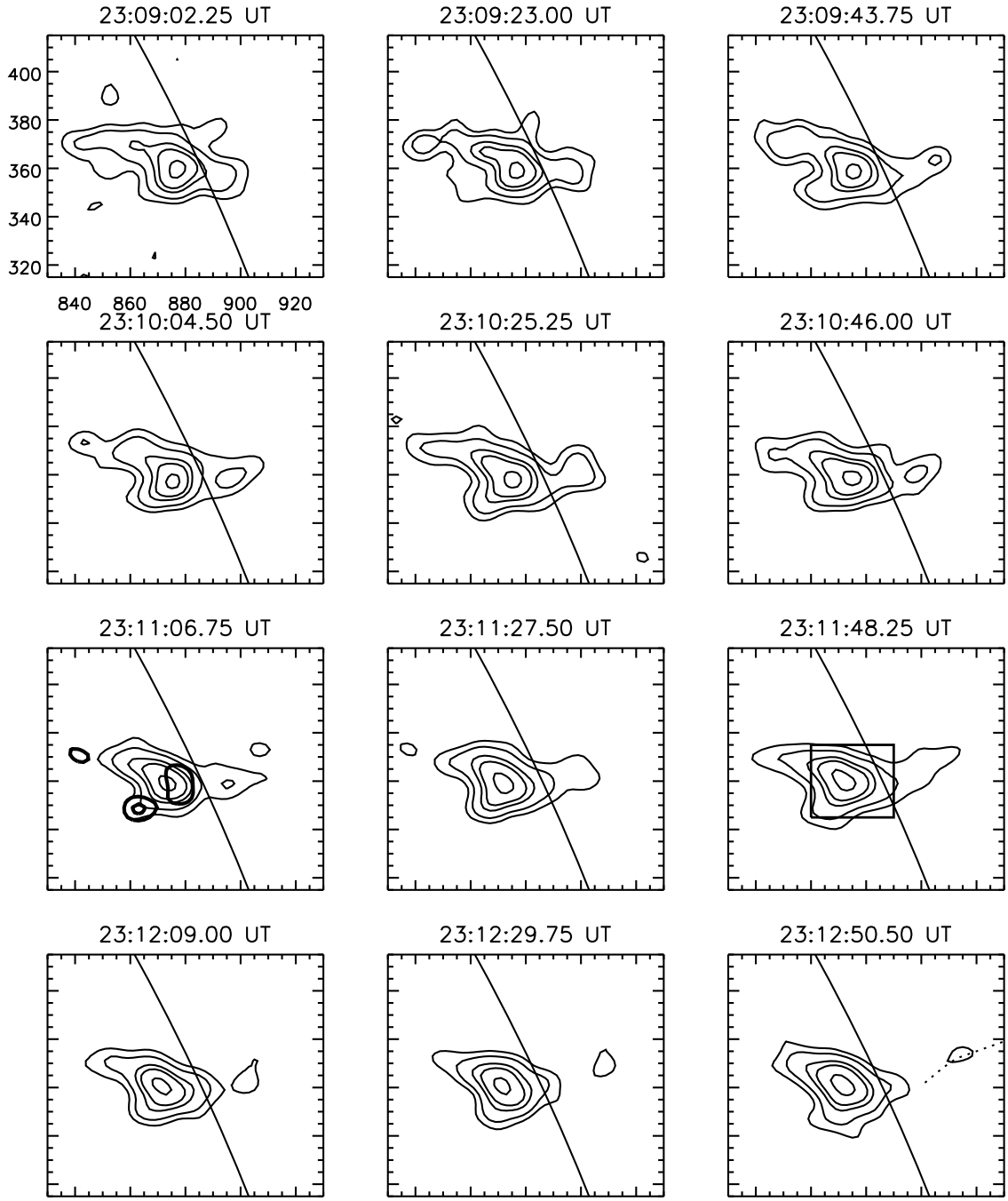

Figure 3.9: A time sequence of RHESSI 10-20 keV images for the 2002 April 15 flare. The images were reconstructed with the CLEAN algorithm using grids 3-9, giving an angular resolution $\sim 7''$. The accumulation time of each of the images is 20 s. The start time of each image is indicated. The contour levels are 15, 25, 45, 60, and 90% of the peak flux in each image. The RHESSI 25-30 keV image (thick contours) at the flare HXR peak is overlaid on the 10-20 keV image at 23:11:06 UT. Its contour levels are 55 and 90% of the peak flux. The box in the image at 23:11:48 UT shows the size of the image in Fig. 4.5. The dotted line in the last panel shows the trajectory of the coronal source above the loop.

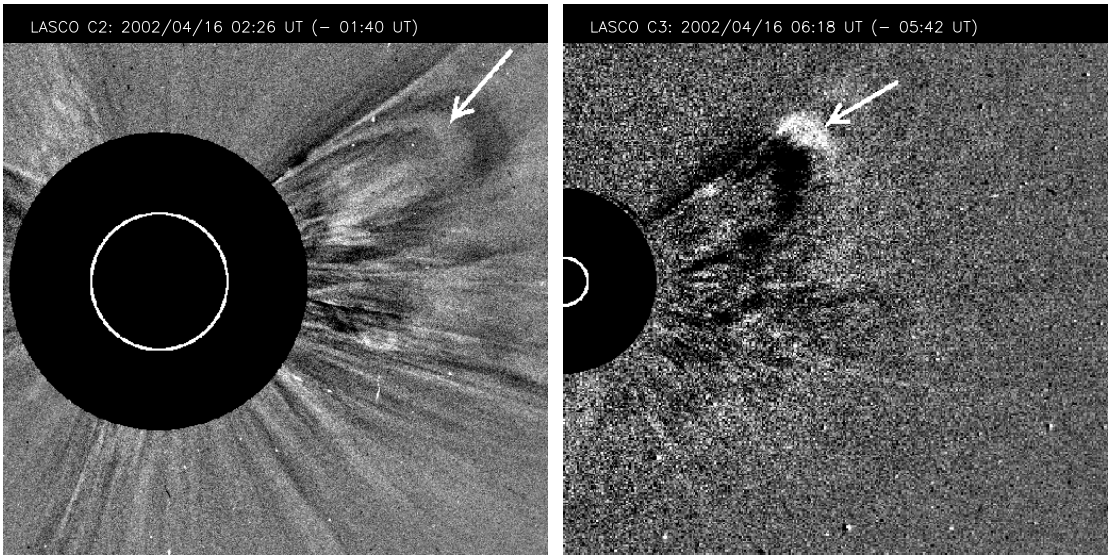

Figure 3.10: SOHO/LASCO C2 (left panel) and C3 (right panel) images on April 16, 2002. The arrow indicates the leading edge of the CME.

bands in Figure 3.12 (diamond symbol). It is evident that the coronal source at higher energies is located lower in altitude than it is at lower energies. Because the coronal source appeared only in images below 20 keV, it was most likely due to thermal emission. Therefore, the energy gradient implies that the hotter part of the coronal source is located lower in altitude than the cooler part. This negative gradient of altitude vs. energy is of opposite sign to that of the flare loops. The two opposite energy gradients are illustrated in Figure 3.14.

Plasma Blobs Above the Flare Loop

Because the coronal source moved outward at a constant speed of $\sim$300 km s^{-1}, it would exit the field of view of the RHESSI images at around 23:14:00 UT. The RHESSI 10-20 keV images between 23:14 UT and 23:18 UT , however, still show several faint blob-like sources along the trajectory of the initial coronal source above the flare loop. Two images showing these blobs are plotted in Fig. 3.15. Although the location of these sources changed from time to time, they were always located along this trajectory (dotted lines) within $\sim$3 arcsec. Therefore, I believe these blob-like sources may be evidence for magnetic islands initiated by the tearing-mode instability.

It is possible that these blobs could be artifacts of the RHESSI image processing, but the appearance of these blobs in the expected location, at different times, in different energy bands in the RHESSI images constructed with different imaging algorithms, argues against this possibility. The ongoing efforts by the RHESSI team in improving the RHESSI imaging dynamic range will be helpful to further check the reality of these sources.

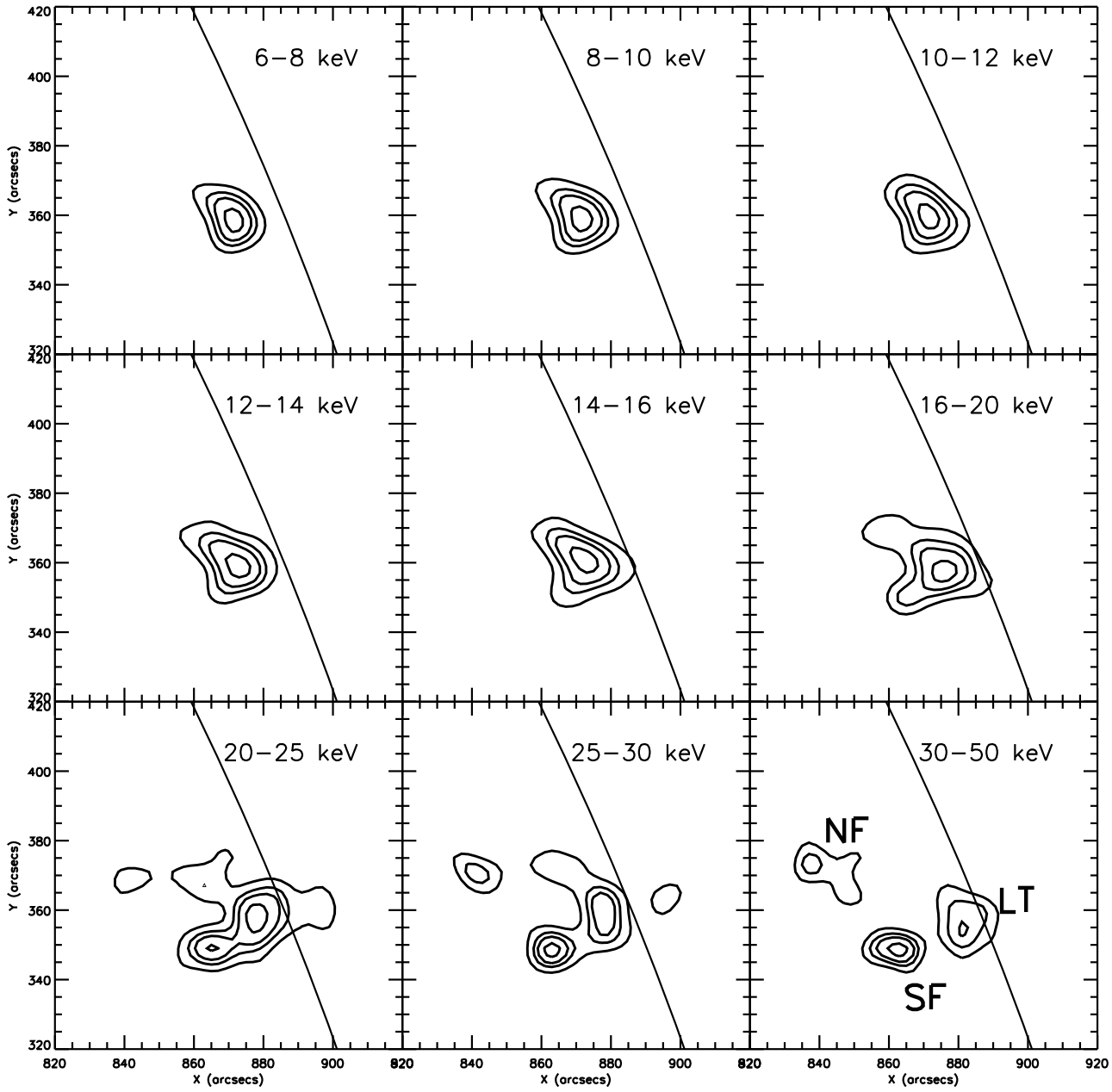

Figure 3.11: RHESSI images in different energy bands at the HXR peak (23:11-23:12 UT). The images were reconstructed with the CLEAN algorithm using grids 3-9, giving an angular resolution $\sim 7''$. The contour levels are 35, 55, 70, and 90% of the peak flux in each image. The labels – NF, SF, and LT – in the bottom right panel indicate the north and south footpoints and the looptop sources, respectively.

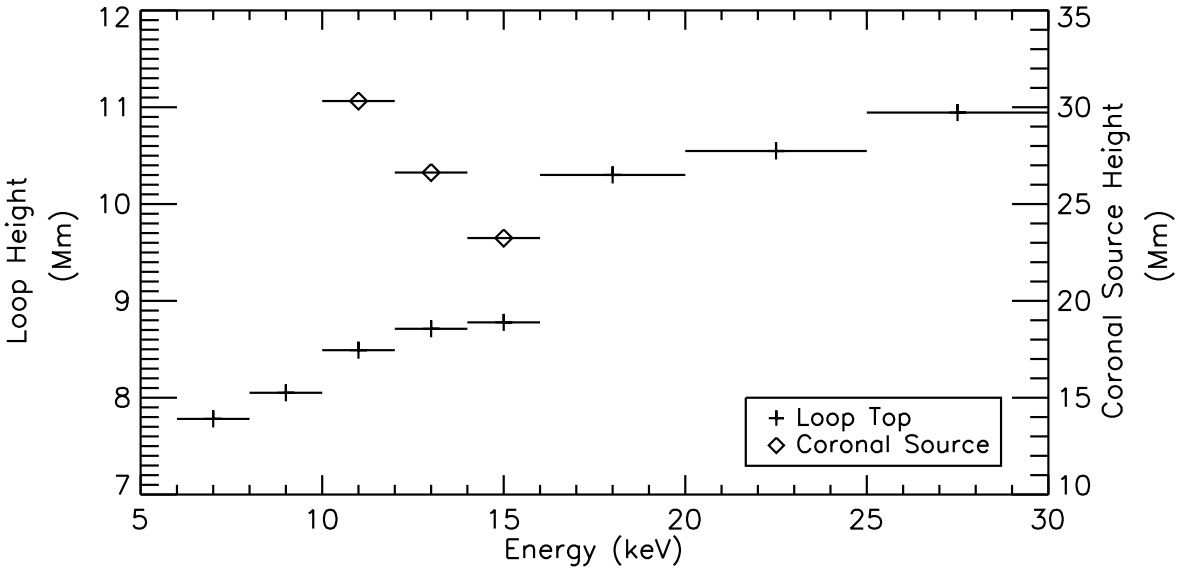

Figure 3.12: The altitude of the looptop centroid and the coronal source centroid at different energies near the HXR peak (23:11–23:11:20 UT) of the 2002, April 15 flare. The horizontal bars represent the energy bandwidth of the RHESSI images.

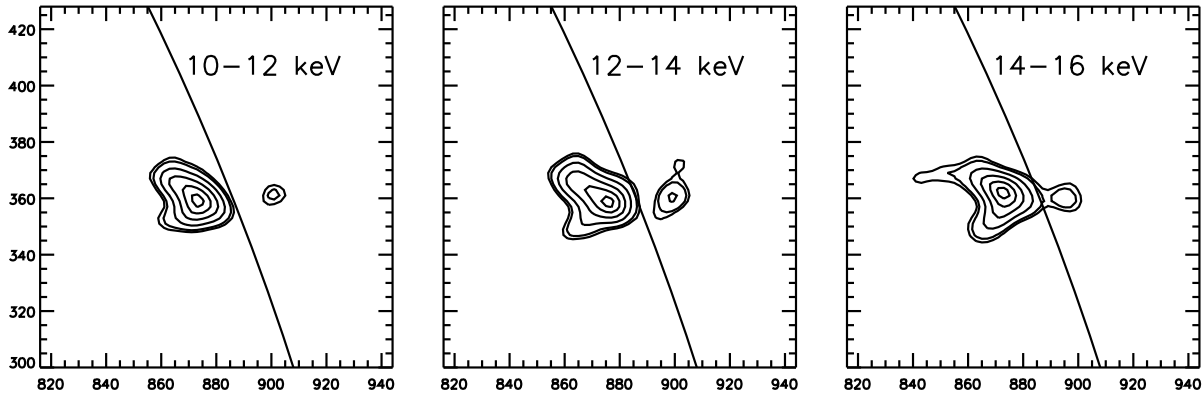

Figure 3.13: RHESSI CLEAN images in three energy bands near the HXR peak (23:11–23:11:20 UT) of the 2002 April 15 flare. The contour levels are 20, 25, 40, 60, 80, and 95% of the peak flux in each image. The solid lines denote the solar limb.

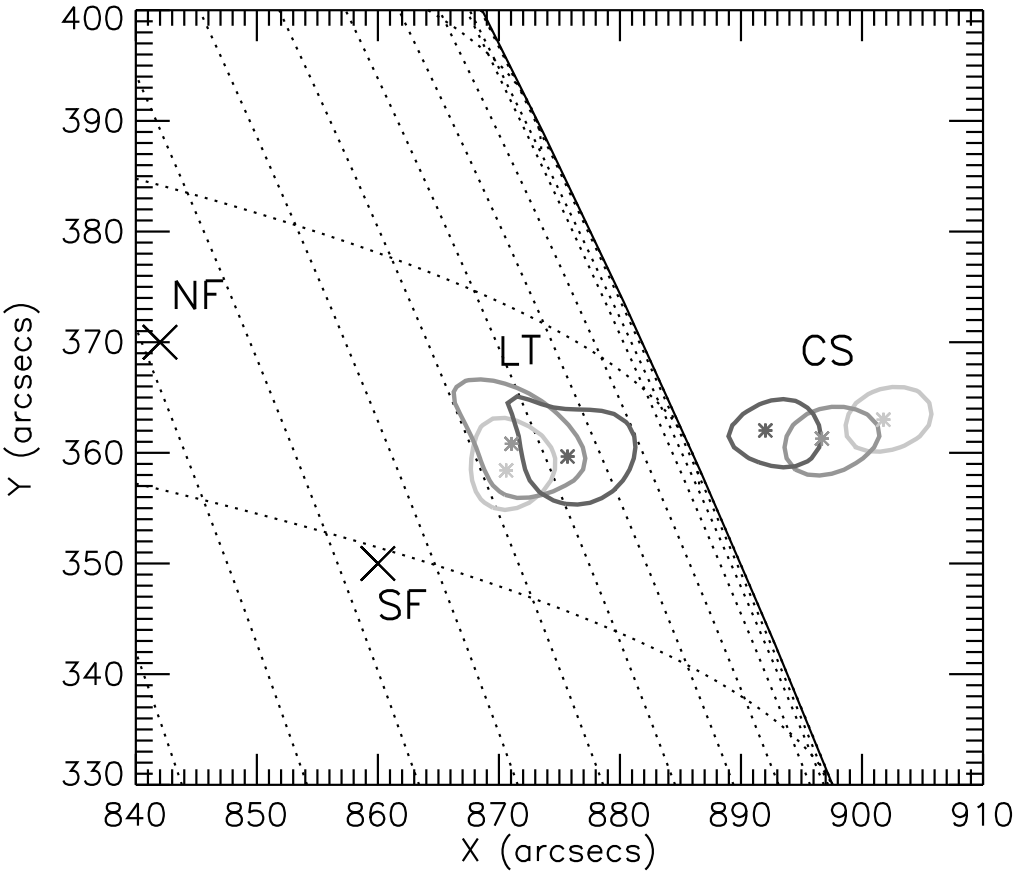

Figure 3.14: RHESSI images in different energy bands at the HXR peak showing the oppsite gradient of altitude vs. energy for the looptop ('LT') source and the coronal source ('CS'). The three contours (80% of the peak flux in each image) on the solar disk indicate the looptops ('LT') in the energy bands (contour line shade from light to dark) 8-10, 12-14, and 16-20 keV. The contours, 80% of the peak flux of the coronal source ('CS') in each image, above the limb are for the (from light to dark) 10-12, 12-14, and 14-16 keV bands. An asterisk ('$*$') marks the centroid of each source. The '$\times$' signs mark the centroids of the north footpoint ('NF') and the south footpoint ('SF') of the X-ray loop.

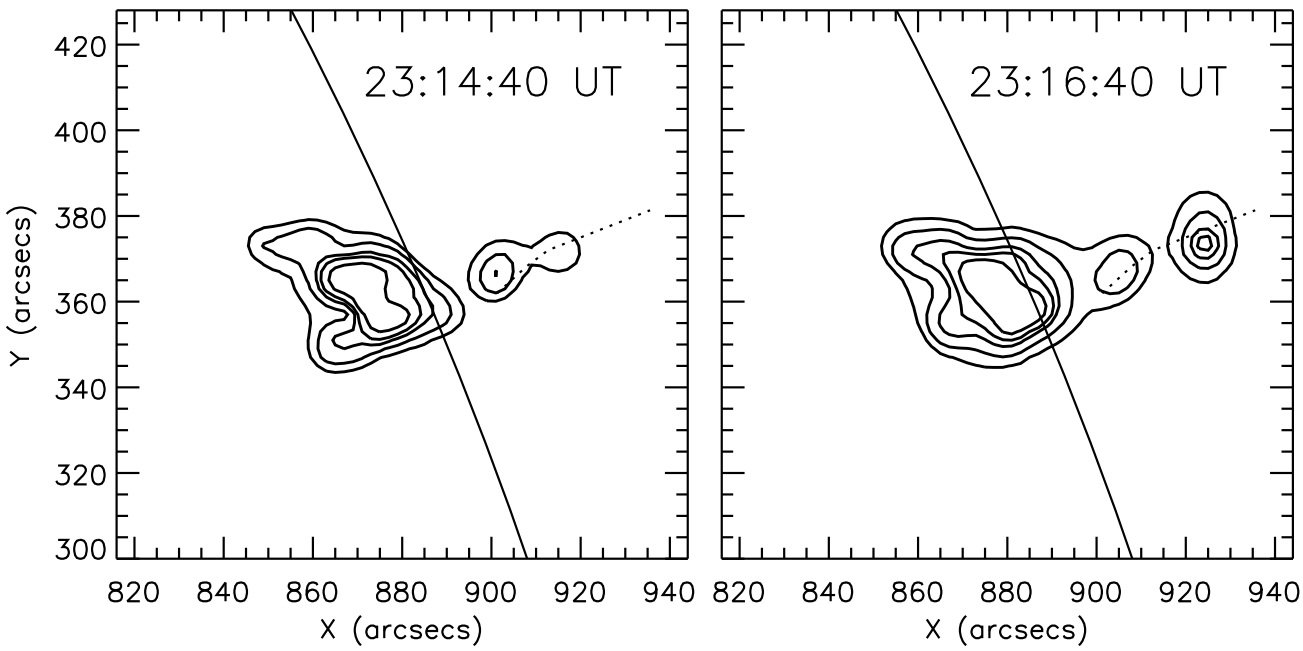

Figure 3.15: RHESSI 12-25 keV images at 23:14:40 UT (left panel) and 23:16:40 UT (right panel) showing coronal blobs believed to be evidence for magnetic islands produced by the tearing-mode instability along a current sheet above the flare loop. The contour levels are 5, 10, 20, 30, and 50% of the peak flux of each image. The dotted line indicates the trajectory of the coronal source above the loop shown in Fig. 3.9.

Discussion of the Observations

The observations provide strong evidence for the presence of a large-scale current sheet above the bright X-ray loop structure. The main arguments are the following:

(1) The temperature distribution pattern of the flare loops and the coronal source in the impulsive phase indicate that a current sheet formed between the top of the flare loops and the coronal source. The temperature distribution of the loops is interpreted in terms of energy supply by reconnection near the top of the loop, the filling with evaporated plasma from the chromosphere, and the subsequent cooling of the inner loops by heat conduction (Švestka et al., 1987; Tsuneta et al., 1992). Above the current sheet, the plasma close to the sheet will also be heated by the energy supplied from the reconnection. Due to adiabatic cooling and conduction, the cooler sources are located farther above the current sheet.

(2) The sudden separation of the coronal source from the underlying loop (see Fig. 3.9) at the start of the impulsive phase indicates the magnetic field configuration has changed, perhaps from X-type to Y-type due to the current sheet formation. The magnetic field configuration is X-type before the impulsive rise. An X-type neutral point tends to be locally unstable, provided the sources of the field are free to move (Dungey, 1953). After the impulsive rise, the X-type magnetic configuration collapses to a configuration with a current sheet having Y-points at each end (Priest & Forbes, 2000). The mechanism of the collapse is still unclear. The length of the current sheet before the HXR peak, i.e., the distance between the top of the loops and the coronal source, is $\sim 10^4$ km.

Based on the observations, it is interesting to speculate on the timing of the current sheet formation and the flare energy release rate. I assume that in the rise phase of the flare, the current sheet has not yet formed, and the magnetic field configuration was X-type. Consequently, the reconnection rate was slow, explaining the relatively low X-ray flux and the relatively smooth nature of the RHESSI light curve. Most of the released magnetic energy heated the plasma within the loops near the neutral point, so the RHESSI images show only a simple looptop source. In the impulsive phase, the current sheet forms and the field configuration becomes Y-type. The reconnection rate suddenly increases matching the increased HXR flux and its impulsive behavior. The appearance of footpoints in the HXR images (25-50 keV) indicates that nonthermal particles are accelerated and dumped into the lower atmosphere. As a result, the magnetic energy dissipated by the reconnection goes to both heating the plasma and accelerating particles. Perhaps the impulsive phase is associated with faster Petschek-type reconnection (Petschek, 1964). After the peak of the HXR emission, the current sheet stretches into a Sweet-Parker type (Parker, 1957; Sweet, 1958) of configuration. The energy release rate decreases as the current sheet expands.

3.2.2 RHESSI Observations of the 2002 April 16 Flare

RHESSI Images

The RHESSI X-ray light curves of this flare in three energy bands are shown in Figure 3.16. They are very similar to those in the 2002 April 15 flare. There was a pre-impulsive burst at 13:03 UT. The impulsive phase lasted about 14 min, from 13:06 to 13:20 UT.

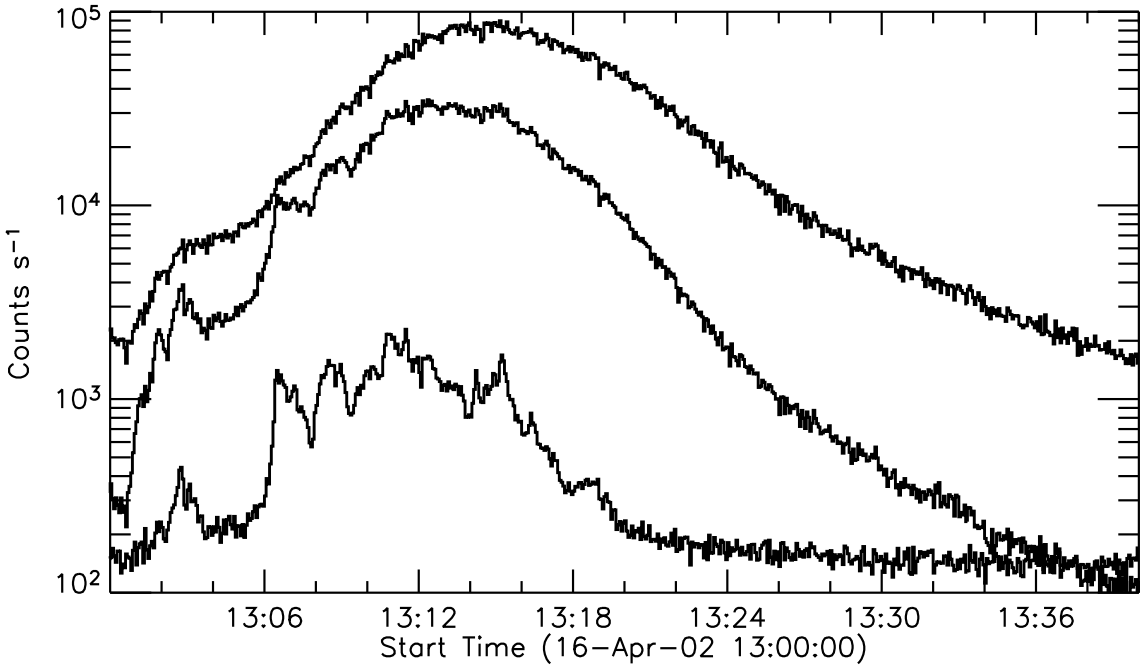

Figure 3.16: RHESSI light curves in three energy bands (from top to bottom): 6-12, 12-25, and 25-50 keV. To avoid overlap, the light curves are scaled by 2.5, 1.0, and 1.0, respectively. The RHESSI thin attenuators were in throughout the flare. The time resolution is 4 s.

Figure 3.17 shows a time sequence of 6-12 keV images starting after the pre-impulsive burst at 13:03:20 UT. Since the count rate was low in the early impulsive phase (before 13:07:20 UT), the image integration time during that period was extended to 1 min. All the RHESSI images below 25 keV are interpreted as showing a flare loop with a bright looptop. Most of the RHESSI 25-50 keV images also show a bright looptop source (see the image at 13:08:20 UT in Fig. 3.17), except at the HXR peak, when the northern footpoint can be seen. The 6-12 keV image in Figure 3.17 at 13:03:20 UT shows a cusp-like coronal source connected to the loop below. Similar to the cusp seen in the rise phase of the April 15 flare, the cusp has a rounded tip. After 13:04:20 UT, the cusp evolved to be a blob-like source but still connected to the underlying loop. At the start of the impulsive phase at 13:06:20 UT, the coronal source clearly separated from the lower loop structure and moved outward at a speed of $\sim$140 km s^{-1}. It disappeared from the RHESSI images at 13:08:20 UT. In this section, I focus only on the energy distribution of the coronal source, so the detailed discussions on the motions of the coronal source are presented in § 4.2.3.

Compared with the coronal source in the April 15 flare, the coronal source in this flare is very bright relative to the looptop, especially when the peak fluxes of the RHESSI images were low. Between 13:04:20 and 13:06:20 UT, the coronal source is $\sim$ 50% as bright as the looptop. After 13:05:20 UT, although the flux of the coronal source did not change, the peak flux of the looptop kept increasing, and so the ratio of the coronal source to the looptop intensity became smaller and smaller. The limited dynamic range of the RHESSI images ($\sim$20:1 with current instrument calibration) most likely explains why the coronal source eventually disappeared from the images after 13:08:20 UT.

All the images in Figure 3.17 were constructed with 'natural weighting', which is one of the weighting schemes used by RHESSI. When forming the RHESSI 'dirty' map using back projection (Hurford et al., 2002), two different weighting schemes, i.e. 'natural weighting' and 'uniform weighting', are employed to optimize the resolution and sensitivity of the map. Following the radio astronomy nomenclature, the use of equal weights for the different subcollimators (RHESSI has 9 subcollimators, only 7 of them being used for Fig. 3.17) is termed 'natural weighting'. For 'uniform weighting' the subcollimators are weighted in inverse proportion to their FWHM resolutions, thus emphasizing the collimators with higher resolution. 'Natural weighting' optimizes the image sensitivity, but has two negative effects on images: (1) it decreases the image resolution; (2) it increases the sidelobes of the dirty map. The alternative, uniform weighting optimizes the resolution and sidelobe level at the expense of sensitivity.

Originally, all the 6-12 keV images were constructed with the default weighting in RHESSI imaging software, i.e., 'uniform weighting'. I found that the coronal source appeared only in the images before 13:07:20 UT, and no coronal source could be seen in the later images (Sui, Holman, & Dennis, 2004). However, after switching to 'natural weighting', the images between 13:07:20 and 13:08:20 UT also show the coronal source. Obviously, the coronal sources during that period are much weaker than the bright loop. This supports the argument that 'natural weighting' optimizes the sensitivity. Compared with the 6-12 keV images constructed with 'uniform weighting' (see Fig. 8 of Sui, Holman, & Dennis, 2004), one obvious difference is that both the loop and the coronal source above the loop appear larger in Figure 3.17. This can be explained by the decrease of the image resolution with 'natural weighting'.

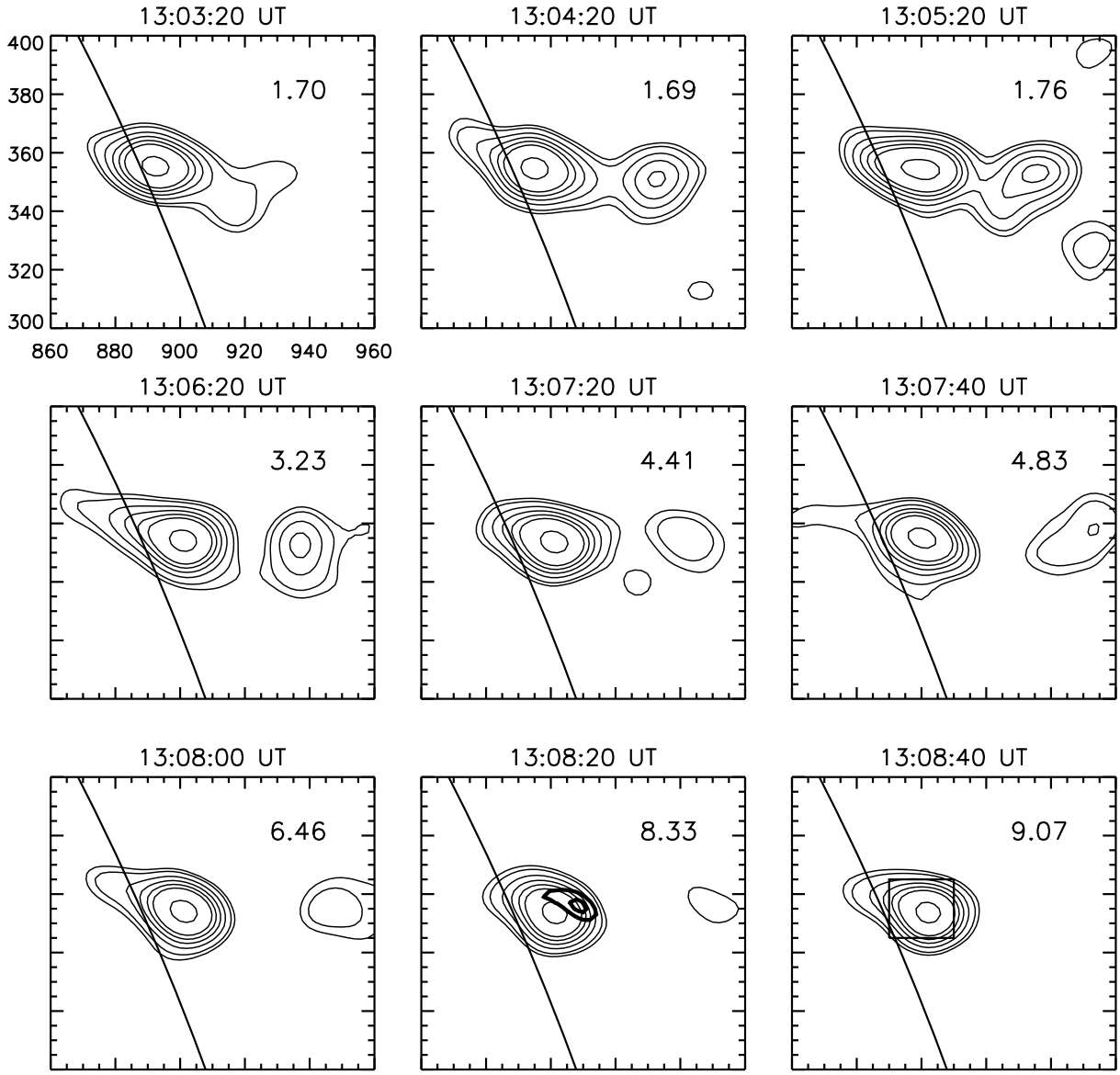

Figure 3.17: A time sequence of RHESSI 6-12 keV images for the 2002 April 16 flare. The images were reconstructed with the CLEAN algorithm using grids 3-9, giving an angular resolution $\sim 7''$. The 'natural weighting' scheme is used in which counts from all detectors are given equal weight. The start time of each image is indicated, and the duration lasts until the start time of the next image. The contour levels are 15, 20, 30, 40, 50, 60, and 90% of the peak flux in each image. The RHESSI 25-50 keV image at 13:08:20 UT is overlaid. The diagonal line denotes the solar limb. The box in the image at 13:08:40 UT shows the outline of the image in Fig. 4.7. The number at the upper right corner of each panel is the peak flux (photons cm^{-2} s^{-1} arcsec^{-2}) in each image.

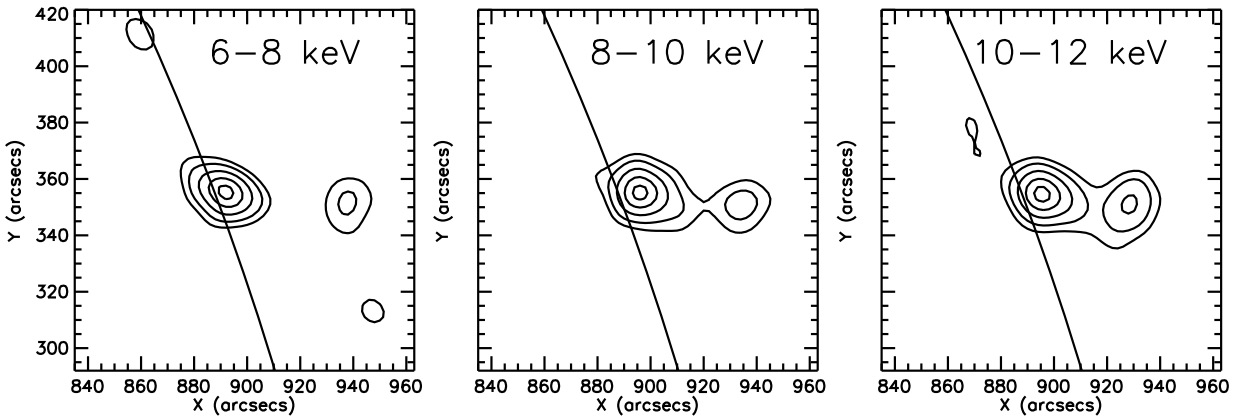

Figure 3.18: RHESSI CLEAN images in three energy bands at 13:04:20 UT. The contour levels are 25, 40, 60, 80, and 95% of the peak flux in each image. The diagonal line denotes the solar limb.

Temperature Distribution of the Coronal Source

Similar to the April 15 flare, the RHESSI images in three energy bands showing the coronal source above the loop are plotted in Figure 3.18. It is evident that the coronal source at higher energies is located closer to the underlying loop. The altitudes of the looptop centroids and the loop heights in the different energy bands were obtained using the same method as for the April 15 flare. They are plotted in Figure 3.19. Obviously, the higher energy part of the coronal source is located lower in altitude than the lower energy part, and the higher energy looptop is located higher than the lower energy looptop. Both are in agreement with the observations of the April 15 flare. Therefore, the temperature distribution inferred from the observations, again, provides strong support for the existence of a large-scale current sheet between the top of the flare loop and the coronal source above it.

3.3 Cusp Structure Observed in Microwaves

Because both microwave and HXR emissions can be produced by highly energetic electrons with different emission mechanisms, the observations in these two wavelength regimes offer us information on different aspects of conditions in the solar atmosphere where flares occur (White et al., 2003). Bremsstrahlung is produced by collisions of accelerated electrons with ambient protons, and therefore requires high densities. Gyrosynchrotron microwave radiation is produced by the interaction of accelerated electrons with the magnetic field. It is extremely efficient and allows us to detect electrons at energies of hundreds of keV, even when their numbers are relatively low.

The 2002 April 15 flare was well observed with the Nobeyama Radioheliograph (NoRH) at 17 and 34 GHz, with spatial resolutions of 10 and 5 arcsec, respectively. In Figure 3.20, I present the 34 GHz NoRH observations of the 2002 April 15 flare showing a cusp structure

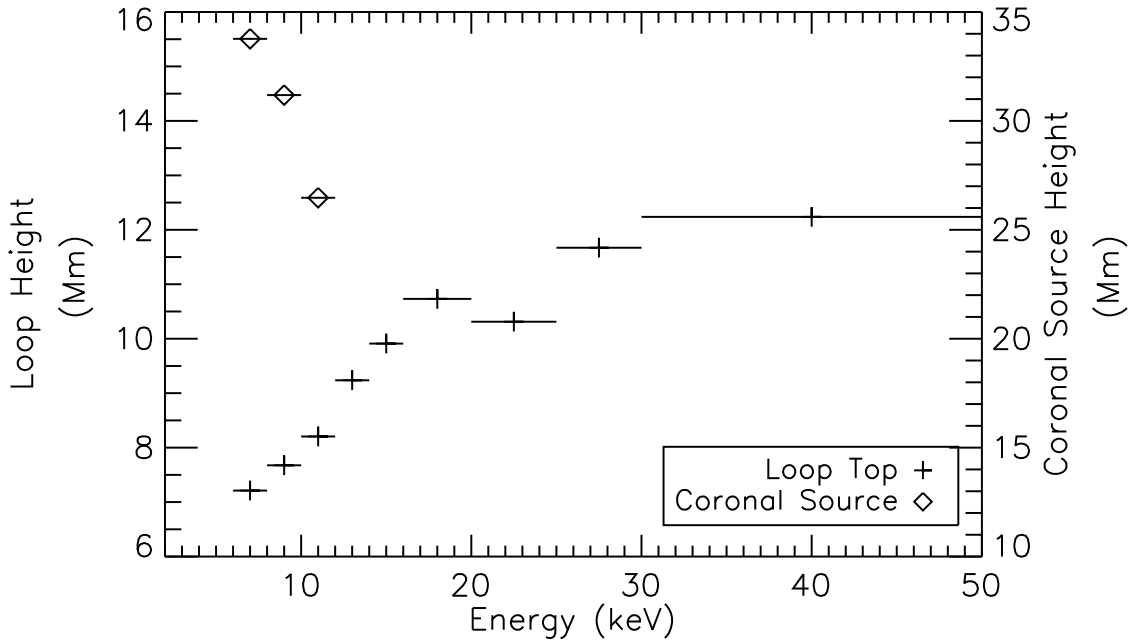

Figure 3.19: Same as Fig. 3.12, but for the 2002 April 16 flare at 13:04:20 UT.

at the HXR peak of the flare (23:11:20 UT). According to my knowledge, this is the first time that a cusp structure has been seen in microwaves. Note that only the cusp-related NoRH observations are presented here. More detailed analysis of the microwave observations is given by Sui et al. (2005).

The time profiles of the microwave fluxes at 17 and 34 GHz are shown in the lower panel of Figure 3.8. Evidently, the spikes at 17 GHz during the impulsive phase correlate with the spikes in the RHESSI 25-50 keV band, suggesting nonthermal radiation dominates at 17 GHz. It is striking that right before the impulsive rise (23:07-23:09:40 UT), even the very small increase in the RHESSI 25-50 keV flux corresponded to a 17 GHz flux increase at the same time. However, the 34 GHz flux did not increase above the preflare level until the impulsive phase started. After that, the 34 GHz flux increased gradually and steadily during most of the flare, except for a short spike during the period of 23:11–23:12 UT, which corresponded to the major peak in both the 17 GHz and the HXR flux at 25-50 keV, suggesting that nonthermal emission dominated during this peak.

During the rise and impulsive phases of the flare, most of the 17 and 34 GHz images indicate a flare loop and two footpoints, in agreement with the RHESSI observation. Besides the loop, the microwave images at both 17 and 34 GHz show a cusp-shaped structure during the impulsive phase. The cusp can be seen in the 34 GHz image at 23:11:20 UT (Fig. 3.20) and the 17 GHz image around the peak of the flare (Fig. 3.21).

The different radiation mechanisms cause differences in the appearance of the flare loop in X-rays and microwaves. In Figure 3.20, the 34 GHz image (darker contours) shows that the two footpoints of the loop are brighter than the rest of the loop, with the northern footpoint brighter than the southern one. This is also seen in the 17 GHz images in Figure 3.21. According to the measurement with the SOHO/Michelson Doppler Imager (MDI), the magnetic field at the northern footpoint is ∼100 Gauss stronger than

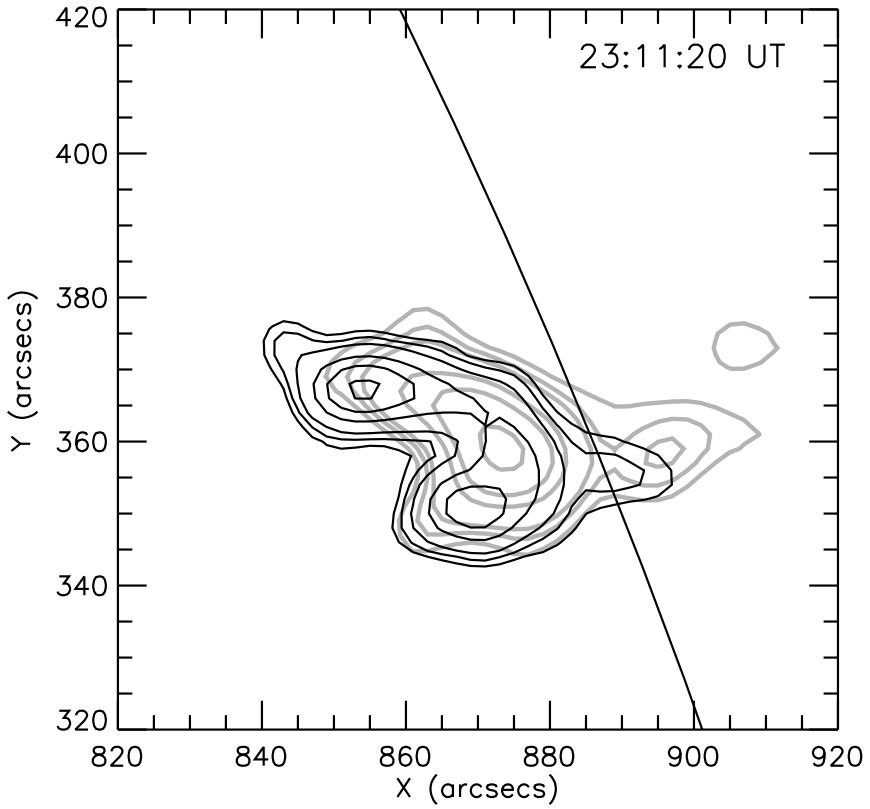

Figure 3.20: 34 GHz image at 23:11:20 UT (dark contours) overlaid on RHESSI 10-20 keV image at 23:11:06 UT (light contour). The contour levels are 17, 22, 30, 50, 70, and 95% of the peak flux for the 34 GHz image, and 15, 20, 25, 45, 60, and 90% of the peak flux for the RHESSI image.

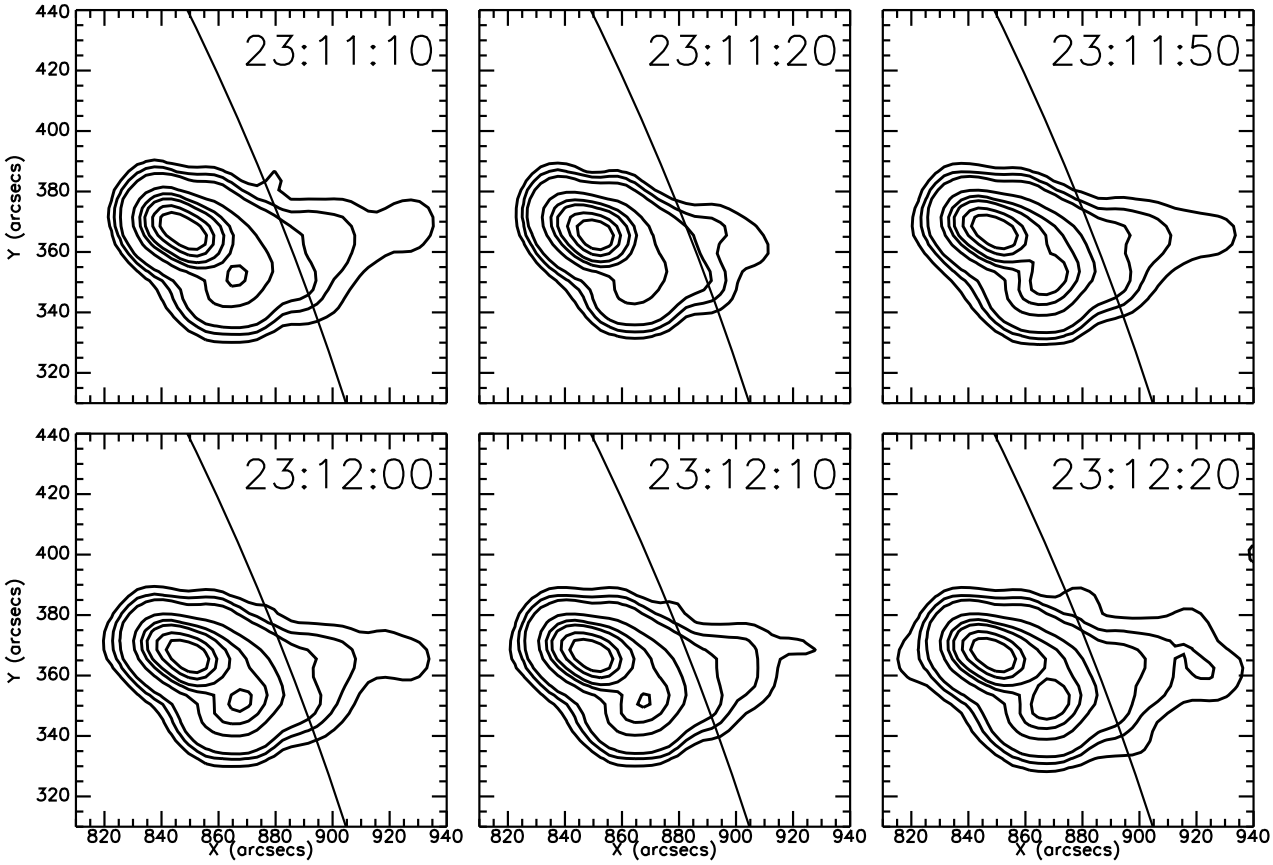

Figure 3.21: NoRH 17 GHz images near the peak of the flare. The contour levels are 0.5, 1, 2, 10, 20, 30, 50, and 70% of the peak flux in each image.

the southern one, leading to stronger gyrosynchrotron radiation near the northern footpoint. Unlike the 34 GHz image, the RHESSI 10-20 keV image (lighter contours) shows that the top of the loop is brightest. Because the SXR flare loop is produced by thermal bremsstrahlung, the bright looptop means either high temperature or high emission measure in the looptop region.

Besides the flare loop, a cusp-shaped coronal source, similar to the cusp often seen with Yohkoh/SXT (e.g., Tsuneta et al., 1992), can be clearly identified in the 34 GHz image in Figure 3.20. Unlike the 34 GHz image, the RHESSI 10-20 keV image shows a blob-like coronal source above the flare loop.

In Figure 3.21, the 17 GHz images around the major peak (from 23:11:00 to 23:12:30 UT) show mostly emission from the two footpoints of the flare loop. The northern footpoint is much brighter than the southern one as mentioned above. There may be some thermal emissions from the rest of the loop. A large cusp-like structure can be seen clearly in these images, extending $\sim$40″ above the solar limb. No such cusp structure can be identified in the 17 GHz images either before or after this period.

More detailed analysis indicates that the upper part of the cusp structure at 17 GHz in Figure 3.21 might be thermal free-free emission from the coronal source, which existed before the flare started above the active region. In the early rise phase, between 23:00 and

23:05 UT, the 17 GHz images showed some emissions from the active region and from the coronal sources above. The coronal source does not have an identified shape. To check whether or not the coronal source in the preflare phase contributed to the cusp at the peak, I subtracted the average of the 17 GHz images during 23:00-23:05 UT from the peak images in Figure 3.21, and found that the cusp disappeared in all the subtracted images. This suggests that the cusp structure might exist and be embedded in the coronal source even before the flare started. Therefore, the upper part of the cusp at 17 GHz could be active-region free-free emission in the same line of sight as the flare loop. Because of the projection effect, it looks like a cusp.

Similarly, I subtracted the average of the 34 GHz images during 23:00-23:05 UT from the 34 GHz image at 23:11:20 UT, and found that the cusp remained in the image. This is not surprising because during the rise phase, the 34 GHz images do not show any identifiable source (Sui et al., 2005). Therefore, the subtracted image will not be much different from the original image. This shows that the cusp in the 34 GHz images was produced by the flare, not by a pre-existing coronal feature.

The remaining question is whether the upper part of the cusp at 34 GHz is caused by thermal or nonthermal radiation. All the cusp structures reported so far (e.g., Tsuneta et al., 1992; Tsuneta, 1996) are believed to be produced by thermal emission, but microwave observations can show both thermal and nonthermal sources. Unfortunately, it is usually difficult to determine which source is thermal and which is nonthermal when they are both present simultaneously. Since there is only one image unambiguously showing the cusp at 34 GHz, I could not judge whether it is impulsive (i.e. most likely nonthermal) or not. If the cusp is thermal, because the blob-like coronal source in the RHESSI image was also thermal (T$\sim$30 MK) (Sui et al., 2005), it is most likely that the cusp is produced by cooler plasma than the plasma producing the coronal blobs above the loop seen in the RHESSI image. Quantitative verification of the argument that the plasma producing thermal emission observed in microwaves is cooler than the plasma producing X-rays observed by RHESSI is presented in Sui et al. (2005). If the upper part of the cusp is nonthermal, then it might be direct evidence indicating the transport of nonthermal electrons from above a flare loop.

3.4 Summary

In this chapter, I have presented three pieces of observational evidence for the existence of a large-scale current sheet above a flare loop:

(1) RHESSI observations of two of the three homologous flares between 2002 April 14 to 16 suggest the approximate location of the two ends of a large-scale current sheet. These observations show the hotter loops located higher than the cooler loops and the existence of a HXR looptop source, agreeing with previous findings (e.g., Tsuneta et al., 1992; Masuda et al., 1994). They suggest the lower tip of the current sheet is located at/above the HXR looptop. The observations also indicate that the hotter part of the coronal source is located lower than the cooler part, suggesting that the upper tip of the current sheet is located at or below the observed coronal source. It is likely that the coronal source was produced by the pileup of the upward ejecta from the current sheet as

it collided with the overlying magnetic field. The third flare that occurred on 2002 April 14-15 also had a coronal source above the flare loop. However, because the coronal source was very weak relative to the loop, the temperature distribution in the coronal source could not be determined.

(2) In the decay phase of the flare on April 15, several blob-like structures are found along the trajectory of the outward-moving coronal source. These sources are believed to be magnetic islands initiated by the tearing-mode instability when the current sheet is stretched and becomes unstable.

(3) Observations in microwaves indicate a cusp magnetic configuration, which is also direct evidence for the presence of a current sheet above the loop. In particular, if the cusp is nonthermal in origin, then it might be the first evidence for the transport of nonthermal particles from the current sheet.

These observations support the standard flare model, in which anti-parallel fields are reconnected in a current sheet above the flare loop.

Although there have been some earlier observations showing coronal sources above flare loops, this is the first time that the temperature distribution of the coronal source could be determined as a function of altitude. Considering the fact that the RHESSI Fourier-based imaging processes can introduce artifacts, care has to be taken in interpreting the RHESSI observations.

For the purpose of testing the observations, flare simulation with RHESSI imaging software is a very strong tool. My simulations have indicated that the energy distribution in the coronal source above the loop, with the high energy part located closer to the flare loop than the lower energy part, is not caused by the imaging process. Future work will include systematic simulations in order to exclude the possibility of artifacts.

Chapter 4

New Features in the Impulsive Phase of Flares

4.1 Loop Motions in Flares

The motion of flare ribbons and loops is one of the clearest signatures of magnetic reconnection in the solar atmosphere. Decades of flare observations have shown the separation of ribbons or footpoints and the apparent rise of flare loops. These motions have been interpreted as the continual propagation of the reconnection site to new, higher field lines (Kopp & Pneuman, 1976).

It is widely accepted that magnetic reconnection occurs in the corona to power eruptive solar events. Because the magnetic features in the corona are hard to observe directly, many chromospheric observations have been conducted and analyzed in order to study indirectly this coronal magnetic reconnection. The often-observed flare ribbon separation in Hα and footpoint motion in HXRs are believed to be the chromospheric signatures of the progressive magnetic reconnection in the corona. The apparent motions reflect a shift of emission to neighboring footpoints of newly reconnected field lines (Krucker, Hurford & Lin, 2003). The apparent velocity of the footpoints corresponds to the rate of magnetic reconnection in the current sheet. The model predicts that the speed of footpoint separation is directly related to the rate of magnetic reconnection in the corona. However, Sakao, Kosugi, & Masuda (1998) did not find a clear correlation between the speed of footpoint separation and the HXR flux in the 14 flares observed with Yohkoh/HXT. Several studies of the motion of footpoints in HXRs have been carried out with RHESSI. Fletcher & Hudson (2002) found systematic patterns of apparent footpoint motion, but the motions varied from flare to flare and did not resemble the simple increase of footpoint separation expected from 2D reconnection models. Krucker, Hurford & Lin (2003) studied the HXR source motions of the 2002 July 23 γ-ray flare. They found the motion of one foot point correlated with the time profile of the HXR flux for that footpoint, but the motion of the other footpoint was too complicated to interpret in this way.

Decades of observations have also revealed the apparent upward motion of flare loops (Bruzek, 1964; Švestka et al., 1987; Tsuneta et al., 1992; Švestka, 1996; Gallagher et al., 2002). The observed lifetime (tens of minutes to hours) of the growing loop system

in X-rays is much longer than the radiative and conductive cooling times (usually a few minutes). Therefore, new, higher loops must be successively forming to keep the growing loop system visible in X-rays. In the standard flare model (Kopp & Pneuman, 1976), successive loop formation is interpreted as resulting from the continuous pileup of newly formed magnetic loops as reconnection continues above the growing nest of loops. Therefore, the faster the reconnection rate, the faster the reconnection site moves upward.

Checking the correlation between the flare loop expansion rate and the HXR flux is an alternative test of the reconnection model. Testing this correlation has some advantages over studies of footpoint motions. When the flare images in X-rays do not show much footpoint emissions, such as the April 14-15 and 16 flares, the speed of footpoint separation is impossible to estimate. Moreover, the speed of footpoint separation is not only related to the magnetic reconnection rate, but also depends on the magnetic configuration in the footpoint areas. If the magnetic flux is high, so that magnetic field lines around the footpoints are very dense, then even at the peak of the flare, the separation speed could be very slow. If the magnetic flux is lower, as may be the case later in a flare, the continual reconnection would lead to a faster footpoint separation. By taking into account both the separation speed (V) and the normal component of the magnetic field strength (B), Qiu et al. (2004) found a temporal correlation in two flares between the HXR flux and $V \times B$, which was believed to be related to the magnetic reconnection rate (Forbes & Priest, 1984; Forbes & Lin, 2000).

Another interesting phenomenon is "loop shrinkage", first suggested by Švestka et al. (1987). Because of the short cooling time of hot, relatively dense plasma, the Hα loops were expected to be at heights very close to the heights of the X-ray loops. However, Švestka et al. found that the hot X-ray loops extend to much greater altitudes than the Hα loops. To explain this, they suggested that the hot X-ray flare loops shrink downward while cooling. The scenario they proposed starts with the magnetic field opening and subsequent field line reconnections. Immediately after reconnection, a cusp-shaped, non-potential loop is formed which subsequently shrinks to a potential configuration without a cusp. As the loops start to cool, the density increases due to chromospheric evaporation and the loops move to a lower altitude. Eventually the loop is observed in Hα at much lower altitudes. The shrinkage was revealed by comparing the height of nested flare loops seen at different wavelengths.

Forbes & Acton (1996) quantitatively studied the shrinkage of post-flare loops in two flares using observations obtained with Yohkoh/SXT. By using only SXR observations, they did not need to consider the possibility that the observed shrinkage is just the result of the plasma cooling as did Švestka et al. (1987). Instead, they interpreted the shrinkage seen in SXRs as rounding of the field line from a cusp to a more-circular shape. Although the whole flare loop system expands with time, they found that the individual field lines shrank by about 20 ($\pm$ 1)% and 32 ($\pm$ 1)% for the two events they studied. Note that although the individual loops shrank, the whole loop system grew upward in the observations.

In this Chapter, I present RHESSI observations of three flares, all of which show a downward looptop motion at the early impulsive phases of the flares and a stationary coronal source above the loops. These new features are believed to be related to the formation or development of a current sheet.

Table 4.1: Summary of the three flares.

Date	April 14-15	April 15	April 16
GOES Class	M3.7	M1.2	M2.5
Location (deg)	N20 W53	N22 W69	N21 W71
Start Time (UT)	23:50:00	23:00:00	12:50:00
SXR Peak (UT)	00:08:00	23:14:00	13:18:00
End Time (UT)	00:50:00	23:20:00	13:40:00
Peak Temperature (MK)	24	32	24
Peak Emission Measure ($10^{48} cm^{-3}$)	6	0.4	3.5
CME Association	No	Yes	No
CME Speed(km/s)	...	300	...

4.2 New Features in Loop Motions

As mentioned in § 3.2, three homologous flares occurred on 2002 April 14-15, 15, and 16 (see Tabel 4.1). They were all located close to the northwest solar limb. The peak plasma emission measure and temperature in the table are obtained from fitting RHESSI spectra over the energy range of 10–50 keV. Their light curves are plotted in Figure 3.7. I presented some of the observations of the April 15 and 16 flares in Chapter 3.

4.2.1 Loop Motions in the 2002 April 14-15 Flare

RHESSI X-ray light curves in two energy bands (6-12, 25-50 keV) are shown in Figure 3.7(a). The flare had a typical gradual rise and fall in SXRs. The impulsive phase in HXRs ($>$ 25 keV) had multiple spikes lasting $\sim$ 12 min. from 00:00 to 00:12 UT.

Four of the RHESSI CLEAN images (Hurford et al., 2002) at 12-25 keV around the start of the impulsive phase are shown in Figure 4.1. The RHESSI images in the 6-12 and 12-25 keV energy bands are interpreted as showing a flare loop with a bright looptop. In addition to the obvious flare loop, there is a faint coronal source above the loop in the first three images. The coronal source did not appear in the images before 00:00 UT on April 15 and its location did not change with time. Because the coronal source is very weak relative to the bright flare loop, I could not make images showing the coronal source at multiple narrower energy bands, as done for the April 15 and 16 flares in Chapter 3. This is the reason why the energy distribution in the coronal source cannot be obtained.

This faint coronal source is distinct from the Masuda-type looptop HXR coronal source (Masuda et al., 1994) in the following aspects: (1) the Masuda source appears in the HXR images at energies above the Yohkoh HXT M1-band (22-32 keV) (Masuda et al., 1995); (2) the Masuda source is located a few arcsecond above the SXR looptop, while the faint coronal source in Figure 4.1 is located much higher above the loop, almost 30″ away from the centroid of the looptop.

The RHESSI 25-50 keV images during the impulsive phase mostly show a bright looptop, which may be due to thick-target bremsstrahlung from electron beams collisionally

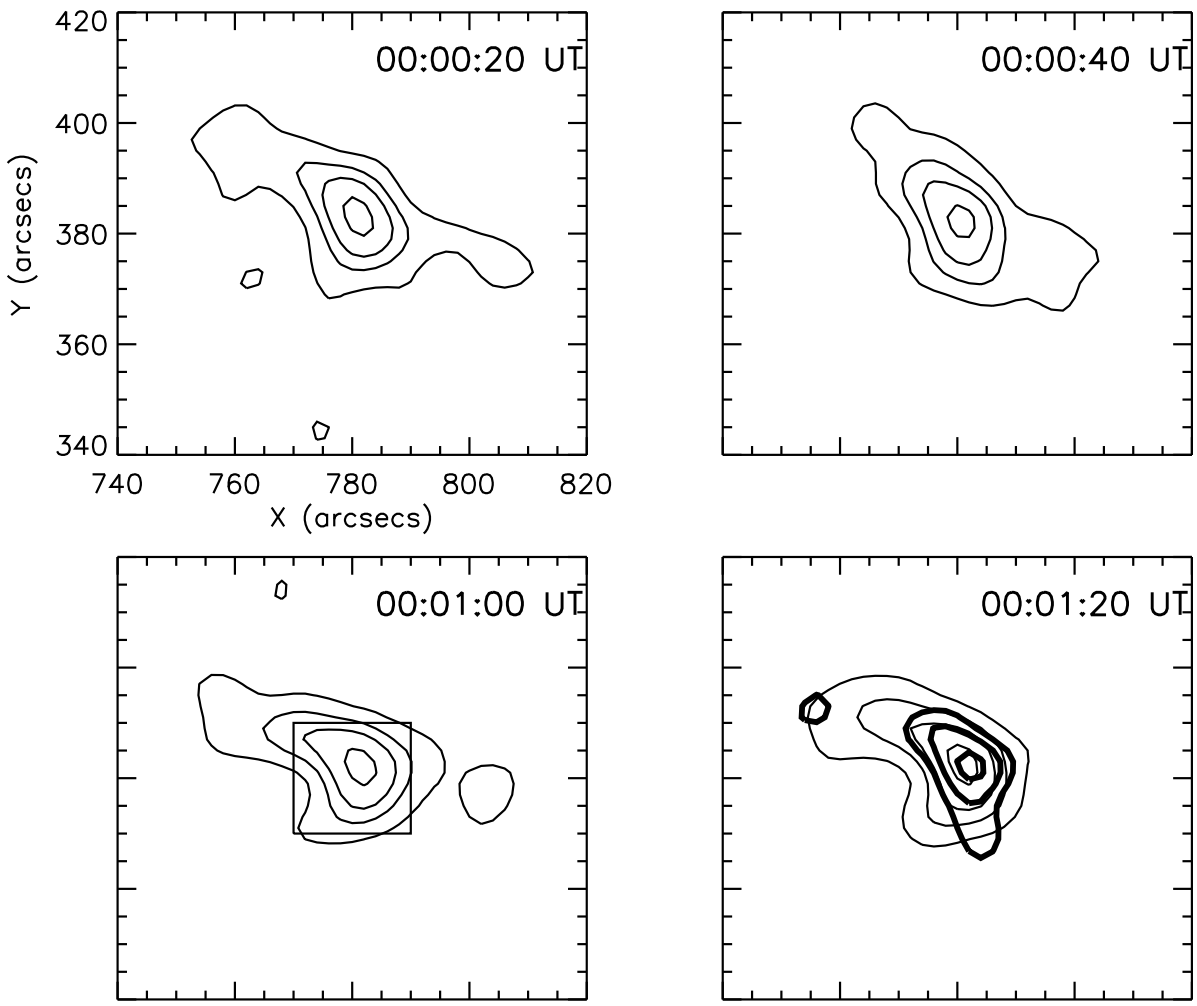

Figure 4.1: A sequence of 12-25 keV RHESSI images at the time of the impulsive rise of the 2002 April 14-15 flare. The time in each box is the start time of the 20 s integration time interval. RHESSI grids 3-9 were used, giving an angular resolution $\sim 7''$. The contour levels are 20, 40, 60, and 90% of the peak flux in each image. The box in the image at 00:01:00 UT delineates the size of the image in Fig. 4.3. The thick contours overlaid on the image at 01:20 UT are 40, 60, and 90% of the peak flux of the 25-50 keV image at that time.

stopped within the loop due to very high column densities in the loop (Veronig & Brown, 2004). Some of the 25-50 keV images also show very faint footpoints. A sample 25-50 keV image at 00:01:20 UT is plotted in Figure 4.1.

Because the flare loops in the 6-12 and 12-25 keV images consistently have a bright looptop, I have used the centroid of the flux within the 60% contour to quantify the location of the looptop source. The altitude of the looptop centroid is defined in the same way as used in § 3.2.1, i.e., the distance between the centroid of the looptop and the center of the line between the two footpoints. The altitude of the looptop centroid in the following two flares was obtained in the same way. The correction for projection effects is neglected because all three events occurred close to the northwest limb, giving only a 10-20% error assuming the flare loop is perpendicular to the surface of the Sun. Here I am interested only in the altitude variation of the centroids, so this error will not compromise the study. Figure 4.2 shows the altitude history of the looptop centroid. Due to the low count rate in the rise phase of the flare, the integration time of the images was 1 min. before 00:00 UT and 20 s after.

Although the resolution of the images in Figure 4.1 is 7″, the centroid can be determined with an accuracy of less than one arcsecond from RHESSI images. When the count rate was low in the rise phase of the flare, however, the loop morphology in the RHESSI images varied from frame to frame. This results in larger errors in determining the location of the looptop centroid. So far, I have not found a good way to estimate errors in determining the centroid location for RHESSI images, except for the Back-Projection images reconstructed with a single grid (Hurford et al., 2003). Image simulation using RHESSI simulation software might be a solution (Gordon Hurford, private communication). Therefore, I limit the study of the behavior of the looptop centroids to when the count rate was high enough ($\geq 10^3$ counts s^{-1}) so that RHESSI images with 20 s integration time showed stable and consistent loop structure.

There are several notable features in Figure 4.2:

(1) The altitude of the looptop centroid obtained from the 12-25 keV images is consistently higher than that from the 6-12 keV images. This indicates that hotter loops are located higher than cooler loops, in agreement with previous Yohkoh/SXT and RHESSI observations (Tsuneta et al., 1992; Tsuneta, 1996; Gallagher et al., 2002). This temperature distribution has been interpreted as evidence for energy release from magnetic reconnection above the top of the loop.

(2) Around the HXR impulsive rise of the flare (from 00:00 UT to 00:04 UT), the altitude of the looptop centroid decreased by 13% of the initial looptop altitude in the 6-12 keV images, and 20% in the 12-25 keV images. A linear fit gives downward speeds of 10 and 11 km s^{-1} for the 6-12 and 12-25 keV bands, respectively.

(3) After 00:04 UT, the looptop altitude increased continuously in both energy bands. The dashed line in the lower panel of Figure 4.2, which shows the speed of the looptop centroid in the 12-25 keV band, shows a correlation with the HXR flux at 25-50 keV. The speed of the looptop centroid is determined by taking the time derivative of the 12-25 keV altitude curve using the 3-point derivative function in IDL. The average speed is about 20 km s^{-1} in period 'A', which is faster than the speed of $\sim$10 km s^{-1} in period 'B', when the HXR flux is lower. A sudden increase of the speed in period 'C' to $\sim$40 km s^{-1} correlates with the sudden increase of the 25-50 keV flux in this period, although with a

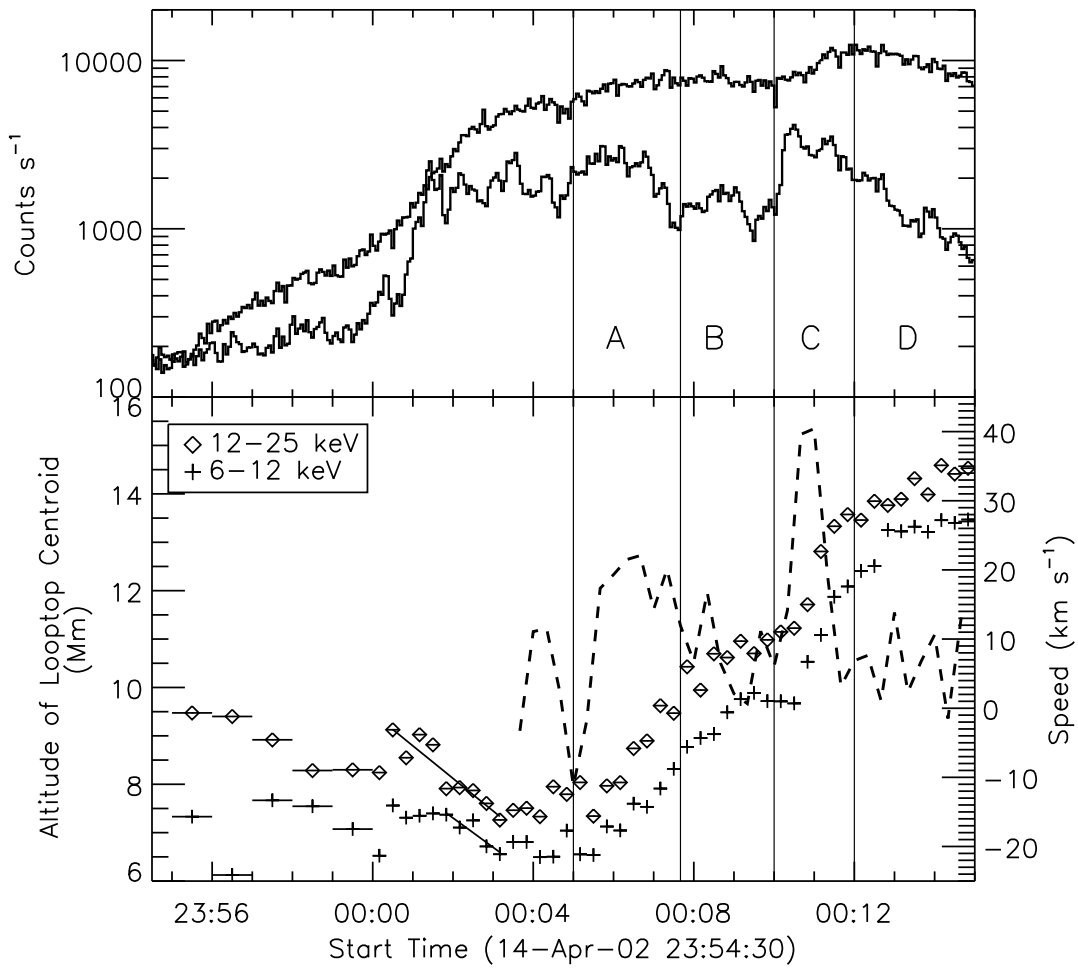

Figure 4.2: *Upper panel*: light curves in two energy bands (upper curve: 6-12 keV rate $\times 0.1$, lower curve: 25-50 keV rate $\times 1.0$) for the 2002 April 14-15 flare. The time resolution is 4 s. *Lower panel*: altitude of the looptop centroid within the 60% contour for the images in the 6-12 keV band (plus signs) and 12-25 keV band (diamonds). The horizontal bars on each point represents the integration time of the corresponding image. The solid lines show linear fits to the altitudes vs. time for two time ranges and two energy bands. The dashed line represents the apparent velocity of the looptop, determined by taking the (3-point) time derivative of the 12-25 keV altitude curve after 00:03:50 UT.

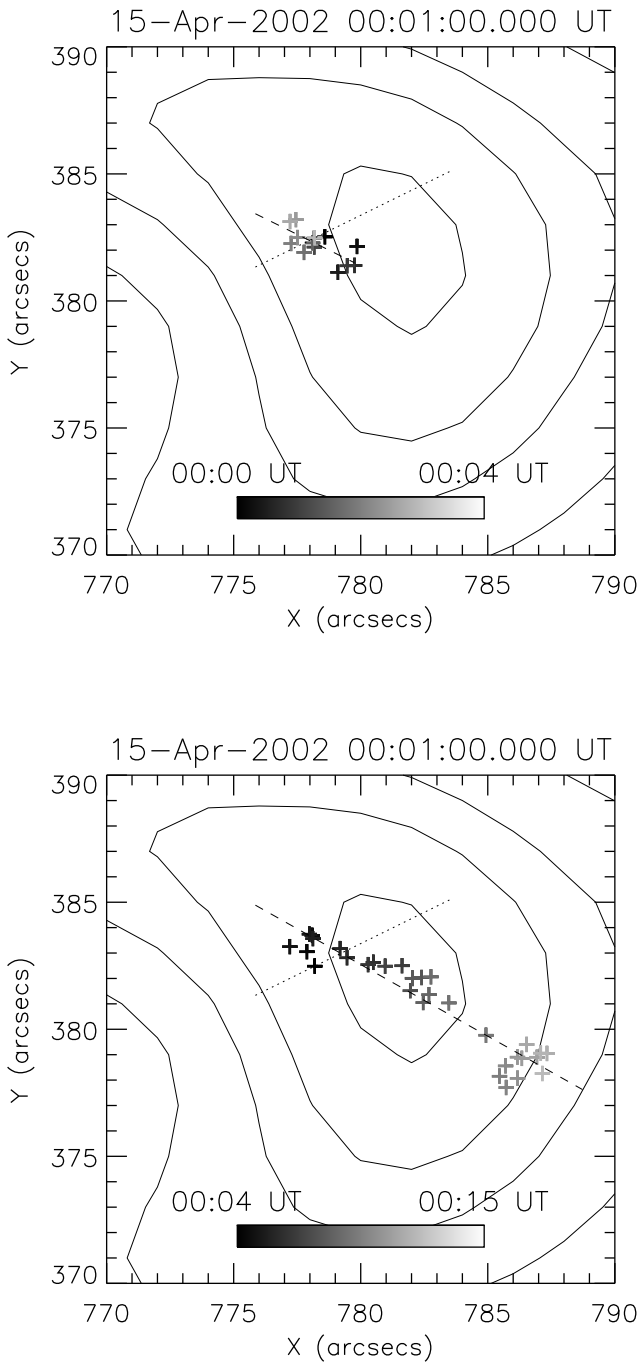

Figure 4.3: Looptop centroids (plus signs) overlaid on the looptop region contours of the 12-25 keV image of the April 14-15 flare at 00:01:00 UT shown in Fig. 4.1. The *upper panel* and the *lower panel* show the centroids moving downward before 00:04 UT and upward after 00:04 UT, respectively. In both panels, the dotted lines represent the radial direction, while the dashed lines, which are from a linear fit to the centroid locations, represent the direction of motion. The angles between the radial direction and the direction of motion are 53° (*upper panel*) and 56° (*lower panel*).

delay of 20-40 s. The speed quickly decreased down to 5 km s^{-1} in period 'D' when the HXR flux was decreasing.

The first downward and then upward motions of the looptop centroids are also illustrated in Figure 4.3, where the locations of the looptop centroids, gray-coded by time, are plotted on the central region of the 00:01 UT 12-25 keV image shown in Figure 4.1. Notice that the looptop centroids in both the downward and the upward motions are clustered on a line whose direction is far (about 53-56°) from the radial direction. The centroid initially moved away from the coronal source above the loop, and then moved toward the coronal source above the loop after 00:04 UT. The downward and then upward source motion is similar to that observed for the following two flares.

4.2.2 Loop Motions in the 2002 April 15 Flare

The second flare occurred at the end of April 15, almost 24 hours after the first flare. RHESSI X-ray light curves in two energy bands (6-12, 25-50 keV) are shown in Figure 3.7 (*middle panel*). They are strikingly similar to those for the first flare in almost all aspects, except that the impulsive phase was shorter by a factor of ∼3 (4 min. vs. 12 min.).

RHESSI images at 10-20 keV are shown in Figure 3.9. Like the first flare, all the images at energies between 6 and 25 keV show a flare loop with a bright looptop. As discussed in § 3.2.1, besides the flare loop, the images before the impulsive phase show a cusp-shaped coronal source with a rounded tip connected with the loop below. When the impulsive phase started, the coronal source separated from the underlying flare loop. The coronal source then stayed stationary for about 2 minutes before moving outward at a speed of about 300 km s^{-1} soon after the major HXR peak of the flare at 23:11:40 UT.

Figure 4.4 shows the history of the looptop altitude obtained from the 6-12 and 12-25 keV images. The altitudes of the coronal source, obtained in the same way as the looptop altitude, are also plotted in Figure 4.4. In this figure, I find: (1) The loops in the 12-25 keV images are located consistently higher than at 6-12 keV, in agreement with Figure 4.2. (2) The looptop altitude in both energy bands decreases from the time of the HXR impulsive rise until the peak in SXRs at around 23:12 UT. The altitude decreased about 24% of the initial looptop altitude in the 6-12 keV images, and 23% in the 12-25 keV loops. The indicated linear fits give downward speeds of 15 and 23 km s^{-1} for the 6-12 and the 12-25 keV bands, respectively. (3) Around the 6-12 keV peak of the flare at 23:12 UT, the looptop centroid started to move upward at speeds of 15 and 20 km s^{-1} for 6-12 and 12-25 keV, respectively. (4) The coronal source stayed stationary at an altitude of ∼25 Mm when the looptop altitude was decreasing. It then moved outward at ∼300 km s^{-1} starting at 23:12 UT, the same time as the start of outward motion of the looptop centroid.

The downward and upward motions of the looptop centroids are also illustrated in Figure 4.5. Although the centroids showing the downward motion are more scattered, the looptop centroids in both downward and upward motions are still clustered on a line. The direction of the upward motion (13° from the radial direction) is closer to the radial than the downward motion (30° from the radial direction). Notice that the coronal source also changed its direction of motion to be more radial (see Figure 3.9) when it started to move outward after 23:12 UT. This indicates that the looptop centroid first moved away

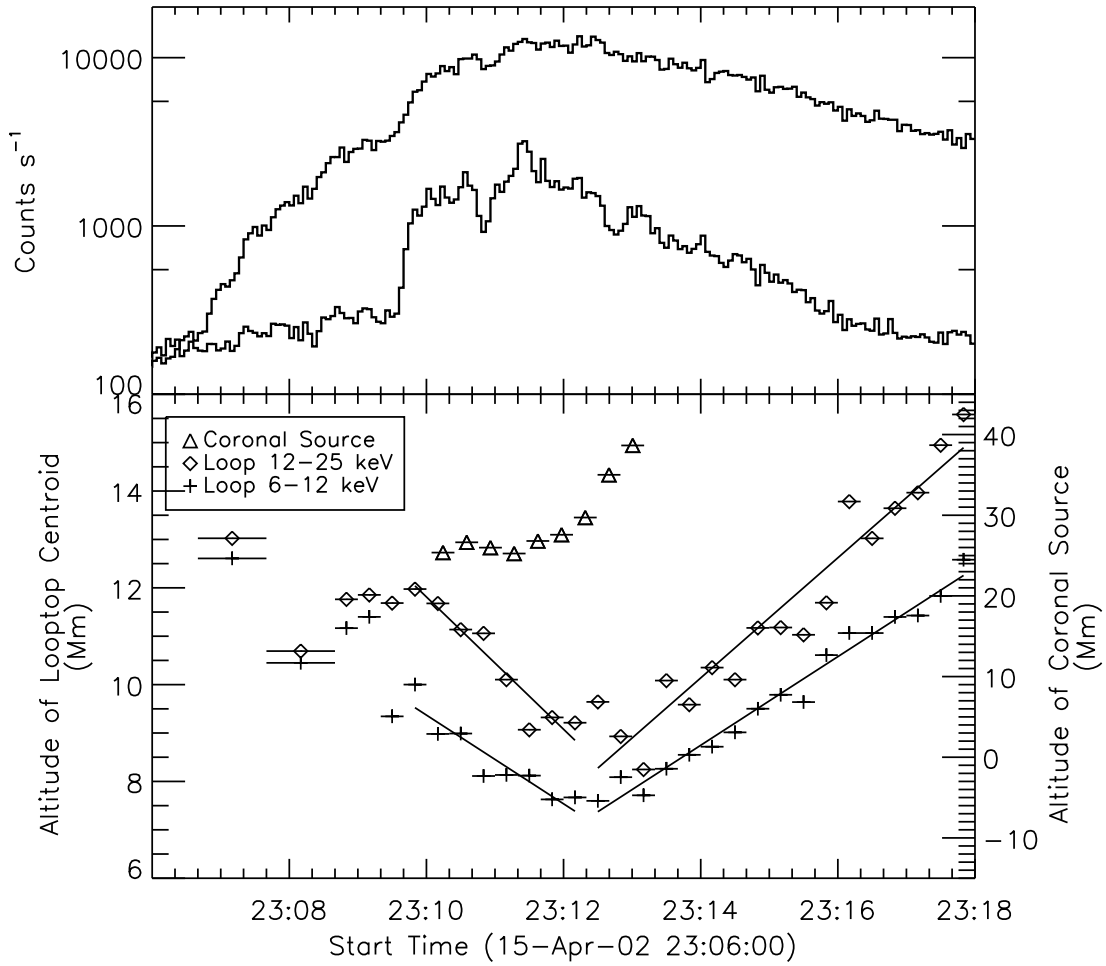

Figure 4.4: *Upper panel*: light curves in two energy bands (upper curve: 6-12 keV rate $\times 0.5$, lower curve: 25-50 keV $\times 1.0$) of the 2002 April 15 flare. *Lower panel*: altitude of the looptop centroid obtained using the 60% contour for the images in the 6-12 keV band (plus) and 12-25 keV band (diamond). The triangles show the altitude of the coronal source above the flare loop. The horizontal bars on each point represents the integration time of the corresponding image. The lines show linear fits to the altitudes vs. time for two time ranges and two energy bands.

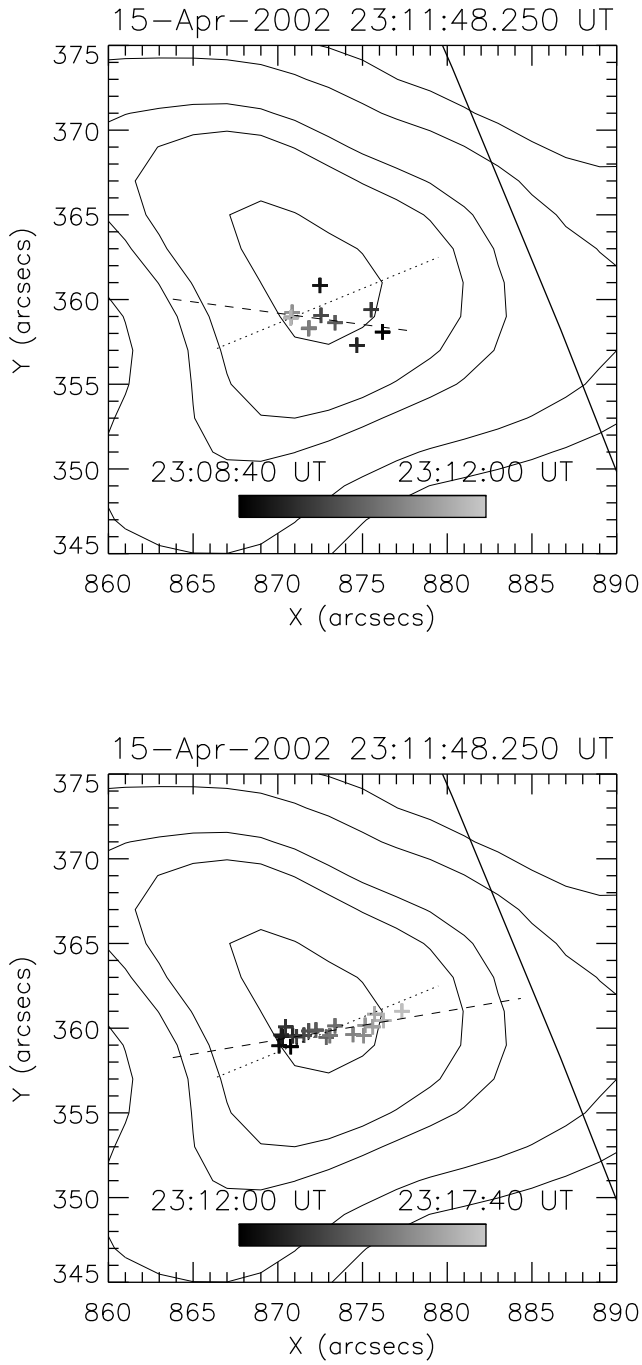

Figure 4.5: Looptop centroids (plus signs) overlaid on the looptop region of the 10-20 keV image of the April 15 flare at 23:11:48.25 UT shown in Fig. 3.9. The other aspects of the figure are the same as for Fig. 4.3. The angles between the radial direction and the direction of motion are 30° (*upper panel*) and 13° (*lower panel*).

from and then towards the coronal source above the loop, which is consistent with the observations of the April 14-15 flare.

4.2.3 Loop Motions in the 2002 April 16 Flare

The RHESSI X-ray light curves of this flare in two energy bands are shown in Figure 3.7 (*bottom panel*). They are very similar to those in the earlier two flares. There was a pre-impulsive burst at 13:03 UT. The impulsive phase lasted ∼14 min.

A time sequence of 6-12 keV images are plotted in Figure 3.17. Like the two earlier events studied above, RHESSI images below 25 keV show a flare loop with a bright looptop. The images between 13:03:20 and 13:08:20 UT show a coronal source above the flare loop.

Figure 4.6 shows the altitude-time profile of the looptop centroid and the coronal source above the looptop. Before the HXR impulsive rise at 13:06 UT, the altitude of the looptop centroid increased steadily in both the 6-12 and 12-25 keV bands. This large increase in altitude can also be seen clearly in Figure 3.17. The earlier RHESSI images show that loop emission came mainly from much lower altitudes than the loops in the later images. When the impulsive phase started, the looptop centroid in the two energy bands stayed at the same altitude for about 2 to 3 min. before moving downward. That the loops maintain their altitudes around the impulsive rise was also suggested in the earlier two flares (see Fig. 4.2 and Fig. 4.4). I also noticed that the altitude decrease in the two energy bands did not start simultaneously. The looptop altitude in the 12-25 keV band started to decrease about 1 min. earlier than in the 6-12 keV band. This non-simultaneity in two energy bands is also indicated in the April 14-15 flare (see Fig. 4.4).

The looptop altitude in both energy bands decreased until 13:11:40 UT. The altitude of the looptop decreased about 16% of the initial altitude for the 6-12 keV loops, and 30% for the 12-25 keV loops. Linear fits give speeds of 8 and 12 km s^{-1} for 6-12 and 12-25 keV, respectively. Immediately after the major HXR peak at 13:11:40 UT, the looptop altitude in both energy bands started to increase with average velocities of 3 and 4 km s^{-1} for 6-12 and 12-25 keV, respectively. This is much slower than for the earlier two flares. Because of the relatively low velocities and the scatter in both energy bands, the correlation between the loop expansion rate and the HXR flux cannot be determined as it was for the April 14-15 flare. Figure 4.7 shows the location of the looptop centroids for the 12-25 keV band plotted on the central region of the 6-12 keV image at 13:08:40 UT. Like the two earlier flares, the looptop centroids in both the downward and the upward motions are clustered along a line between 24° and 30° from the radial direction, and they moved first away from and then towards the coronal source above the looptop.

In this flare, the coronal source above the flare loop behaved somewhat differently from that in April 15 flare. Compared with the earlier analysis by Sui, Holman, & Dennis (2004), more 6-12 keV images have been found to show the coronal source. Moreover, the quality of the coronal sources in the images constructed with 'natural weighting' has been improved with respect to those constructed with 'uniform weighting' by Sui, Holman, & Dennis (2004). Therefore, the motion of the coronal source can be studied in more detail. Figure 4.6 indicates that right before the impulsive phase started, the coronal source seems to move slowly at ∼15 km s^{-1}. After the impulsive rise from 13:06:20 to 13:07:40 UT, the

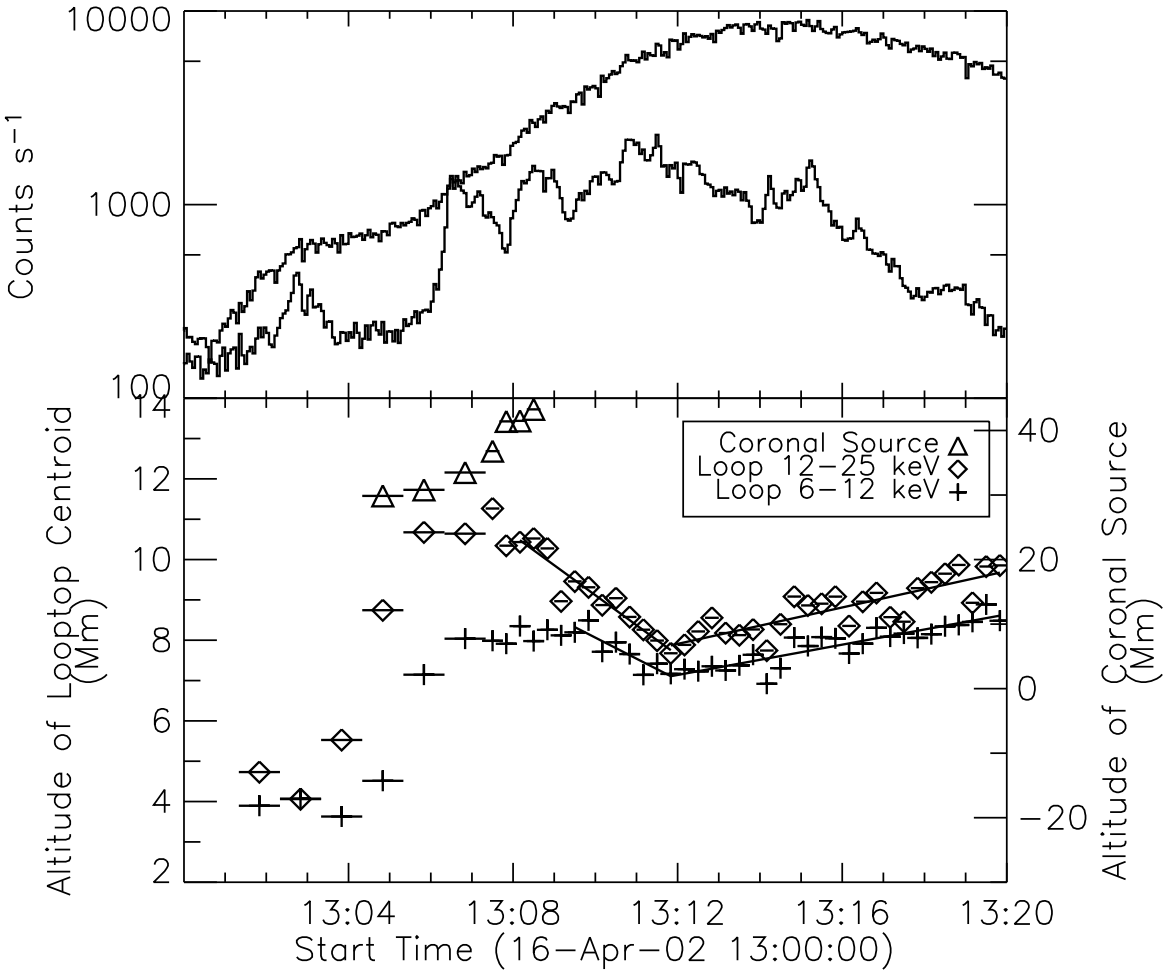

Figure 4.6: *Upper panel*: Light curves in two energy bands (top curve: 6-12 keV, bottom curve: 25-50 keV) for the 2002 April 16 flare. The scale factors are 0.25 (6-12 keV) and 1.0 (12-25 keV). *Lower panel*: Altitude of the looptop centroid obtained in the 6-12 keV band (plus signs) and 12-25 keV band (diamonds). The horizontal bars on each point represent the integration time of the corresponding image. The lines show linear fits to the altitudes vs. time for two time ranges and two energy bands. The triangles show the altitude of the coronal source above the flare loop.

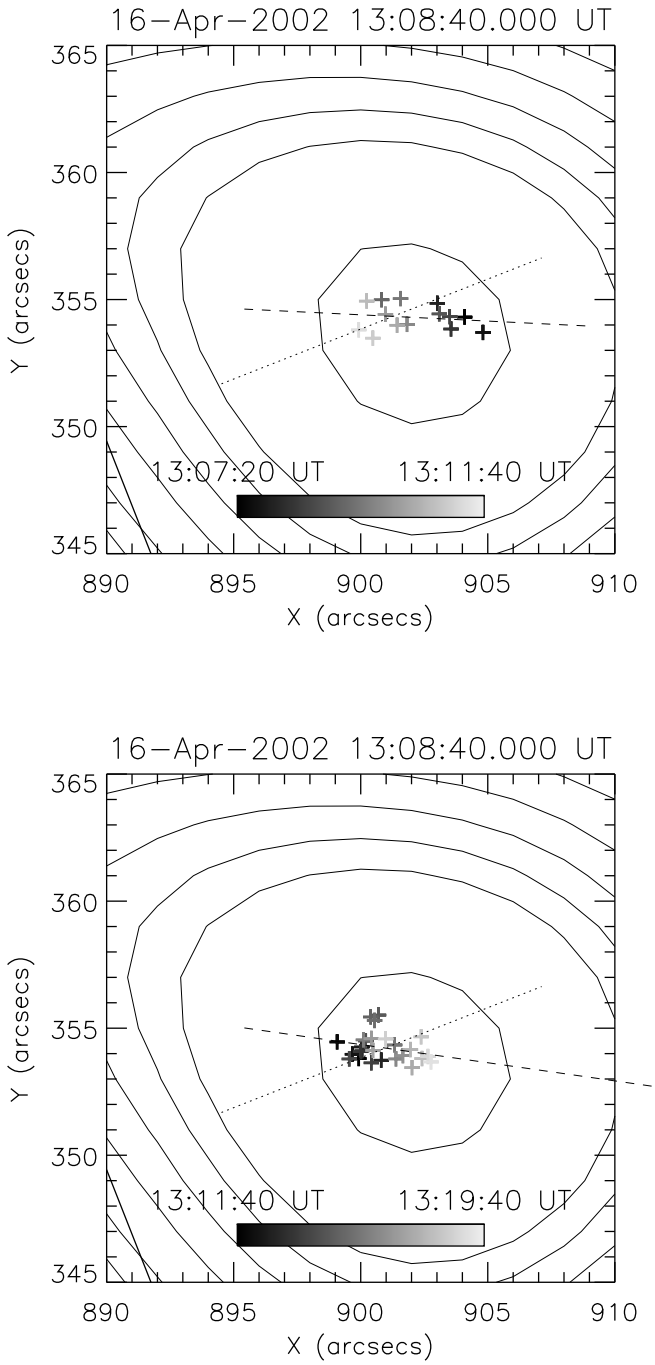

Figure 4.7: Looptop centroids (plus signs) overlaid on the looptop region of the 12-25 keV image of the April 16 flare at 13:08:40 UT in Fig. 3.17. The other aspects of the figure are the same as in Fig. 4.3. The angles between the radial direction and the direction of motion are 24° (*upper panel*) and 30° (*lower panel*).

Table 4.2: Summary of the RHESSI observations of the three flares. The first and second numbers in looptop columns are for 6-12 and 12-25 keV, respectively. The speed ranges of the upward motion for the April 14-15 flare reflect the variation shown in Fig. 4.2.

Date	Looptop (Downward)			Looptop (Upward)	Coronal Source	
	Initial Altitude (Mm)	Decrease (%)	Speed (km/s)	Speed (km/s)	Initial Altitude (Mm)	Speed (km/s)
April 14-15	7.5 / 9	13 / 20	10 / 11	3∼35/5∼40	27	...
April 15	10 / 12	24 / 23	15 / 23	15 / 21	25	300
April 16	8.5 / 11	16 / 30	8 / 12	3 / 4	31	140

speed of the coronal source increased to ∼140 km s^{-1}. In the same period, the looptop centroid remained at the same altitude. From 13:07:40 to 13:08:20 UT, the coronal source seems to stay almost stationary, while the altitude of the looptop centroid started to decrease, which is similar to the two flares presented above. Because the coronal source disappeared from the later images, it is very difficult to judge what happened to it. As discussed in § 3.2.2, the disappearance of the coronal source could be due to the limited image dynamic range.

4.3 Summary and Discussions

I have presented RHESSI observations of three homologous flares from the same active region. Results are summarized in Table 4.2. The three flares share the following common features:

1. The centroid altitudes of the looptops seen at higher energies were at a higher altitude than those of loops seen at low energies, indicating that the hotter loops were above the cooler loops.

2. Around the start of the HXR impulsive phase, the altitude of the looptop centroid started to decrease with time, with the altitude in the 12-25 keV band decreasing more (except for the April 15 flare) and faster than that in the 6-12 keV band.

3. Some time later near the SXR peak the altitude of the looptop source began to increase with velocities up to 40 km s^{-1}.

4. A separate coronal source appeared above the flare loop around the start of the impulsive phase, and it stayed stationary for a few minutes.

5. The looptop centroid always moved along a direction which is either away from or toward the coronal source above the loop.

Some of these features have been seen before. The altitude increase of flare loops has been reported by Bruzek (1964), Švestka et al. (1987), Tsuneta et al. (1992), and Švestka (1996). The temperature distribution of loops was seen by Moore et al. (1980), Švestka et al. (1987), and Tsuneta et al. (1992). The altitude increase of the looptop leads to the interpretation that the energy release occurred at higher and higher altitudes in the corona. The observations of higher temperature loops located higher in altitude than cooler loops support the scenario of energy release above the top of the flare loops.

In the flare of April 14-15, I found a correlation between the loop growth rate and the HXR (25-50 keV) flux of the flare (Fig. 4.2), as expected in the standard reconnection model (Carmichael, 1964; Sturrock, 1966; Hirayama, 1974; Kopp & Pneuman, 1976). The faster the reconnection site moves up, the faster the reconnection rate. More electrons are accelerated and, therefore, more HXR emission is observed. I found that the increase in the upward speed of the looptop source was delayed by 20-40 s with respect to the rise in the HXR flux. This time delay could be the time scale of the chromospheric evaporation. Observations have indicated that the speed of chromospheric evaporation at the impulsive phase of the major eruption varies from 300 to 800 km s^{-1} (Antonucci, Dodero, & Martin, 1990, and references therein). For the April 14-15 flare, the loop height is about 30 arcsec (or 2.0×10^4 km), so it would take 20-60 s to fill a loop, in agreement with the RHESSI observation. Therefore, the flare loops may be formed by plasma evaporation due to an electron beam striking the lower atmosphere (for the flares with copious footpoint emission in HXRs, such as the April 15 flare). Alternatively, the plasma evaporation may be due to thermal conduction (for the flares with much less footpoint emission, such as the April 14-15 flare and the April 16 flare).

Previous observations indicated a continuous expansion of the flare loops (Bruzek, 1964; Švestka et al., 1987; Tsuneta et al., 1992; Švestka, 1996). The observations I present here show a different scenario. Early in the impulsive phases of the three flares, the looptop centroids move downward instead of upward. One possible explanation for this apparent downward motion is that the reconnection site moved horizontally along loops in an arcade toward Sun-center, giving the impression of an altitude decrease. However, the following points argue against this possibility:

(1) By checking the time history of the footpoint centroids in the April 15 flare, which is the only flare with consistently strong footpoint emission in the impulsive phase, I did not find any systematic footpoint motion.

(2) For all three events, the altitude decrease and the speeds of downward motion are often significantly different in the 6-12 and 12-25 keV bands (see Table 4.2). This is in conflict with the assumption of motion along an arcade.

(3) The non-simultaneous start of the downward motion of the looptop source in the 6-12 and 12-25 keV bands for both the April 14-15 flare and the April 16 flare is also in disagreement with this kind of motion along an arcade.

My preferred explanation for the change in the measured position of the centroid is that the sources did, in fact, decrease in altitude early in the impulsive phases of all three flares. Based on the observational results, I propose two possible scenarios to explain this initial apparent fall of the looptop sources. Of course, some combination of these two scenarios could also be operating. Both scenarios assume that the energy is released above the loops by magnetic reconnection in the standard flare model, but use different

mechanisms to explain the apparent downward motion.

In the first scenario, the downward motion results from the relaxation of the newly reconnected field lines from a sharp cusp to a more semi-circular shape. This is similar to the model proposed by Švestka et al. (1987) and Forbes & Acton (1996) but on a much shorter time scale. The ∼2-4 min. duration of the decrease in altitude in all three flares is consistent with the time taken for the loops to change their shape in this way (Lin et al., 1995; Lin, 2004).

In the second scenario, the initial downward motion results as the reconnection changes from slow X-point to the much faster Petschek-type (Petschek, 1964). As this change takes place, not only would the energy release rate increase dramatically, consistent with the start of the impulsive phase, but also the lower bound of the current sheet would be pushed downwards, consistent with the observed initial decrease in altitude of the looptop source.

In both scenarios, once the looptop source has reached a stable lower altitude where it can go no lower, the general rise of the current sheet would dominate over the other effects, and the centroid of the source would rise monotonically as higher and higher loops are created, in agreement with the observations for all three flares. In two of the flares (the flares on 15 and 16 April), this upward motion starts as the 25-50 keV flux begins to decay, suggesting a further transition in the reconnection process to the slower Sweet-Parker type (Parker, 1957; Sweet, 1958).

The downward motion of the looptop centroid early in the impulsive phase of the flares has only recently been recognized. The coronal source in the 2002 July 23 γ-ray flare also shows a noticeable downward motion early in the flare (see the right panel of Fig. 3, Krucker, Hurford & Lin 2003). The recent event analyzed by Liu et al. (2004) using RHESSI data shows a similar downward motion, suggesting that the downward motion of the looptop may be a common feature. Ultimately, the best way to show that the observed downward motion of the looptop centroid is a change in altitude is to search for similar effects in other flares at different locations on the solar disk. More events will be studied in future work.

A stationary coronal source above the flare loops has never been observed before. A moving coronal source or plasma blob above flare loops has been observed (see review by McKenzie, 2002). The velocity of the coronal sources is in the range of 30–400 km s^{-1} (Shibata et al., 1995). In the standard reconnection model, magnetic fields of opposing directions cancel out in the current sheet, and the tension that exists in the resulting non-potential field causes the expulsion of two oppositely directed jets. One jet appears as a plasmoid with embedded magnetic field moving upward, while the other downward directed jet piles up to form the arcade.

Here I present a somewhat more complicated scenario. In the three events, a coronal source appeared near the time of the HXR impulsive rise, and was observed to stay stationary for 1∼2 min. before disappearing from the images (for the April 14-15 flare), or move outward continuously (for the April 15 and 16 flares). Because the three flares occurred in the same active region and seem homologous, it is reasonable to assume that the coronal source in the April 14-15 flare would also have eventually moved outward. As discussed above, the reason I do not see it moving outward may be due to the limited dynamic range of the RHESSI images.

Because the stationary coronal sources are usually much weaker than the flare looptops, I must consider the possibility that these coronal sources are artifacts of the image reconstruction process. The systematic variation of these sources with time and energy argues against this. Simulations using RHESSI imaging software will be pursued in the future to determine at what level the artifacts might become important.

There are many models of solar eruptive events: the kink instability and filament eruption model (Cheng, 1977; Hood & Priest, 1979), the tether cutting model (Moore & Roumeliotis, 1992), the flux rope model (Priest & Forbes, 1990; Forbes & Priest, 1995; Lin & Forbes, 2000; Lin, 2002), the magnetic breakout model (Antiochos, 1998; Antiochos, Devore, & Klimchuk, 1999), the quadruple magnetic source model (Uchida et al., 1999; Hirose et al., 2001), etc. For the purpose of interpreting the observations, I use the flux rope model because it not only predicts magnetic reconnection in a current sheet above the observed hot flare loops, but it also predicts the evolution of the extended, long-lived current sheet. In their model, Forbes & Priest (1995) proposed that the converging photospheric flow or flux emergence leads to the formation of a sheared arcade field containing a flux rope. Two photospheric field sources approach each other until a catastrophe point is reached and the pre-existing flux rope erupts. The eruption drives reconnection in a current sheet below the flux rope. If the rate of reconnection is fast enough, the upward velocity can become high enough to allow the flux rope to escape and become a CME. The elongated current sheet can last for several hours and extend many solar radii into the outer corona.

Some of the predictions from the flux rope model agree with the observations. I interpreted the coronal source above the flare loop as the upper tip of a large-scale current sheet in the flux rope model. This was based on the temperature distribution of the coronal sources in the April 15 and 16 flares, i.e., the higher temperature part located lower in altitude than the low temperature part. The model predicts that the speed of the upper tip of the current sheet is in the range of 200-700 km s^{-1} (Jun Lin 2003, private communication), in agreement with the observed speed (300 km s^{-1}) of the outward moving coronal source. I also observed the predicted upward motion of the looptop centroid later in the flares, suggesting the flare loops were formed continuously at higher and higher altitudes. Although the angle between the direction of the upward motion and the radial direction varies (see the lower panels of Fig. 4.3, 4.5, and 4.7), the loop always expanded toward the coronal source, agreeing with the flux rope model.

There are some observations which cannot be explained by the flux rope model or any of the other models in the literature. In the April 15 flare, when the HXR impulsive phase started, the coronal source separated from the underlying loop (Fig. 3.9). It is reasonable to assume that the system had lost its equilibrium at this point. The model predicts that the flux rope is continuously thrust upward after that time. However, the coronal source was observed to stay stationary for about 2 min. before moving outward. So, what kept the plasma from moving outward early in the flare?

Because the downward motion of the looptop centroid occurs over the same time range that the coronal source remains stationary, I believe they are related to each other, and may be associated with the formation or development of the current sheet. So far, most of the models and simulations focus on the magnetic reconnection after it starts, and do not address how the current sheet is dynamically formed and evolves with time. Hopefully,

the observations of the three flares presented here will be an incentive for more theoretical work in this regard.

Chapter 5

Low-Energy Cutoff of Nonthermal Electrons

5.1 Overview of Studies of the Low-Energy Cutoff

5.1.1 Difficulties in Determining the Low-Energy Cutoff

All flare HXR spectra have a negative slope (Dennis, 1985; Lin et al., 1987; Dennis, 1988; Winglee et al., 1991). Although a thermal bremsstrahlung model with multiple temperatures can always be used to fit the data (Brown, 1974; Emslie & Brown, 1980; Brown & Emslie, 1987), power-law photon spectra are generally believed to be produced by bremsstrahlung emission from nonthermal electrons that themselves have a power-law energy distribution. Striking support for this nonthermal, thick-target bremsstrahlung interpretation comes from the observation of simultaneous impulsive HXR emissions from the two footpoints of a flare loop (e.g., Sakao, 1994), as would be expected from the interaction of electron beams with the chromosphere. In order to ensure that the energy in nonthermal electrons is finite, there must be a low-energy cutoff in the electron distribution.

Determination of the low-energy cutoff in the electron distribution is critical in estimating the total energy of the nonthermal electrons and thereby providing an important constraint on electron acceleration mechanisms (Miller et al., 1997). Most previous estimations of the total electron energy have been made with assumed (arbitrary) cutoff energies in the range of 20-30 keV (Dennis et al., 2003, and references therein). The total energy of the injected electrons is very sensitive to the low-energy cutoff, particularly for flares with steep (soft) spectra. For instance, if the electrons have a distribution $f(\varepsilon) \sim \varepsilon^{-\delta}$, where δ is typically in the range of 3–8 Dennis (1985), say δ is 6, assuming thick-target interactions, then the total electron energy ($\int_{\varepsilon_c}^{\infty} f(\varepsilon)\ \varepsilon\ d\varepsilon \propto \varepsilon^{-\delta+2}$, where ε_c is the low-energy cutoff of nonthermal electrons) with a cutoff at 10 keV is almost two order of magnitude larger than that with the cutoff at 30 keV, i.e., $(\frac{10}{30})^{-6+2} = 81$.

Bremsstrahlung spectra flatten at photon energies below the low-energy cutoff of the nonthermal electrons. However, because of the high minimum photon energy detectable by the HXR spectrometers (typically $\geq$20 keV before RHESSI), and the presence of strong thermal bremsstrahlung at low energies, the low-energy cutoff in the electron distribution

has been difficult to determine. Holman & Benka (1992) argued that the low-energy cutoff can in fact be determined by the spectral transition from thermal to nonthermal bremsstrahlung. Low-energy cutoffs ranging from 20-40 keV were obtained with this hybrid thermal/nonthermal model (Benka & Holman, 1994). Gan (2001) and Gan et al. (2002) have found that many of the double-power law spectra obtained from BATSE on the Compton Gamma Ray Observatory (CGRO) were consistent with the flattening that results from a low-energy cutoff ranging from 45-97 keV. A low-energy cutoff as high as 73 keV has also been found for the 2003 July 23 γ-ray line flare (Holman et al., 2003). Recently, Kasparova et al. (2004) found a very flat RHESSI spectrum (with a power-law index of $\sim$1.8), which can be fit with an electron distribution with a low-energy cutoff as high as 81 keV.

All the studies introduced above have demonstrated that the electron bremsstrahlung model with a certain low-energy cutoff could fit a power-law photon spectrum. However, the low-energy cutoff is not uniquely determined. Other cutoff energies are able to fit the same spectrum equally well. RHESSI spectra during the impulsive phase of a flare typically show two components: an exponential (thermal) component at low energies and a flatter power-law or double power-law (nonthermal) component at higher energies. The two components merge smoothly together. In these cases, an upper limit of the low-energy cutoff can be decided with the spectral fitting. Any cutoff energy below that upper limit can still fit the data equally well because at low energies, the fluxes contributed from the nonthermal bremsstrahlung are usually much less than those from the thermal bremsstrahlung. For example, in the C7.5 flare on 2002 February 20 (see § 2.3), the low-energy cutoff was chosen to be 15 keV to minimize the total number of nonthermal electrons. Any energy below 15 keV can be used to fit the data equally well. There have been other ways proposed to give a better estimate of the cutoff energy. Holman (2003) pointed out that after knowing the effects of the low-energy cutoff on both microwave and HXR spectra from the same flare, we may be able to find a cutoff energy consistent with both data sets.

5.1.2 Flare Energetics

It has been of interest for decades to compare the total energy of nonthermal electrons with the thermal energy of the hot plasma. The comparison allows us to know what fraction of the flare energy is deposited into the electron beams. Such study is critical to an understanding of the mechanism of particle acceleration and plasma heating in flares. Early observations indicated that a considerable fraction of the flare energy (perhaps as high as 50%) is converted to accelerate electrons (Brown, 1971; Lin & Hudson, 1976) and ions (Ramaty et al., 1995). Dennis et al. (2003) reported the energetics of over 30 flares, observed with the Hard X-ray Imaging Spectrometer (HXIS) and the Hard X-Ray Burst Spectrometer (HXRBS) of the Solar Maximum Mission (SMM). For most of these flares there was considerably more energy in the electrons (above 25 keV) than in the thermal plasma.

The evaluation of the energy partition in flares is hampered by observational limits. Two of the main uncertainties in the measurements compromise the study of the energy budget: the filling factor of the thermal plasma and the low-energy cutoff in the nonther-

mal electron distribution. The filling factor is the fraction of the observed source volume that contains the hard X-ray emitting plasma. Theoretically, the filling factor is ≤ 1. There are some observations indicating that the filling factor could be as low as 10^{-4} for some coronal loops (e.g., Porter & Klimchuk, 1995; Cargill & Klimchuk, 1997).

The plasma thermal energy (E_{therm}) is equal to $3N_ekT$, where $N_e = n_eV_{real}$ is the total number of emitting electrons in the plasma, n_e is the plasma density, and V_{real} is the real source volume of the thermal plasma. Since the emission measure of the thermal plasma, $EM = n_e^2V_{real}$, can be obtained from spectral fitting, the thermal energy can be calculated from the following expression:

$$E_{therm} = 3 \cdot k \cdot T \cdot \sqrt{EM \cdot V_{real}} = 3 \cdot k \cdot T \cdot \sqrt{EM \cdot V_{measured} \cdot f} \tag{5.1}$$

Where $V_{measured}$ is the source volume estimated from the images, EM and T are the emission measure and temperature, f is the filling factor, and k is Boltzmann's constant. Therefore, the thermal energy is proportional to the square-root of the filling factor.

As discussed above, the uncertainty in the low-energy cutoff severely affects our ability to determine the nonthermal energy. The 25 keV reference energy in the study of SMM flares was set to be equal to the lower energy threshold of the HXRBS scintillation detector (Dennis et al., 2003). If a 10-keV cutoff was used instead, the total nonthermal energy in those SMM flares would be an order of magnitude larger on average. In one flare observed with RHESSI, Saint-Hilaire & Benz (2002) found that the thermal energy content of the hot flare plasma is considerably less than the energy in the nonthermal beam above 10 keV. In the 2003 July 23 γ-ray line X4.8 flare, Holman et al. (2003) obtained upper limits on the low-energy cutoffs by fitting the RHESSI spectra, thus giving a minimum total energy in the nonthermal electrons that was of the same order as the energy in the thermal plasma. An analysis of the flare energetics for the X1.2 flare observed with RHESSI on 2002 April 21 yielded similar results (Emslie et al., 2004).

5.1.3 Comparison of CME and Flare Energies

Solar flares and CMEs are the most powerful events in the solar system. In most models, they are two different manifestations of the same energy release process (i.e., magnetic reconnection) in the solar corona. Therefore, a reliable estimate of energy partition between the flare and CME would provide constraints on the energy release process (Emslie et al., 2004). A statistical study of 249 CMEs observed with the Solar Maximum Mission Coronagraph (Hundhausen, 1999) indicated that the kinetic energy of CMEs correlated poorly with the SXR peak intensities of associated flares. Hundhausen (1999) pointed out that, given the intensity of a flare, the kinetic energy of its associated CME can still be spread over a range of at least three orders of magnitude. Recently, Emslie et al. (2004) found that the CME has the dominant component of the released energy in the two big events analyzed, and both electron and ion energies are half to a whole order of magnitude smaller than the energy contained in the CME.

The photon spectra of the April 15 flare are found to have a distinctive feature so that the low-energy cutoff can be more accurately determined than has previously been possible. In the following sections, I explain how the low-energy cutoff is obtained, and

how the flare and CME energetics are evaluated.

5.2 Determination of the Low-Energy Cutoff

In the April 15 flare, before the HXR impulsive rise at 23:09:40 UT, the RHESSI spatially integrated spectra are well fitted with a model consisting solely of an isothermal bremsstrahlung spectrum (i.e., with an exponential form) in the energy range between 10 and 20 keV. Figure 5.1(a) shows one such spectrum just before the impulsive phase. The temperature of the thermal plasma derived from the fit is 30 MK and the emission measure is $2 \times 10^{47}\ cm^{-3}$. The RHESSI thin attenuators were in throughout the flare observation. When the thin shutters are in, the effective area of the detectors drops rapidly at photon energies below 10 keV (Smith et al., 2002). The current uncertainty in the instrument response matrix is large at these energies, so fluxes below 10 keV were not included for spectral fitting. In addition, the counts below ∼5 keV are dominated by higher energy photons that suffer K-escape when they are photoelectricaly absorbed in the germanium detectors (Smith et al., 2002). Thus, no information about the incident photon flux below this energy can be determined from the RHESSI observations with the attenuators in place.

As shown in Figure 5.1(a), the spectral data below 10 keV are not well fit by the isothermal bremsstrahlung model. There is an iron line complex at ∼6.7 keV (Phillips, 2004). The model-predicted fluxes at ∼7 keV, calculated with the function 'mewe_kev.pro' (in Solar Software) based on the Mewe atomic model (Mewe et al., 1985), are lower than the data points. This could be due to the fact that the iron abundance used by 'mewe_keV.pro', i.e., $\sim 3.9 \times 10^{-5}$, is too low for this coronal flare source. By varying the iron abundance to fit the data, I found that it needs to be increased by a factor of ∼4. The Chianti code, based on the Chianti atomic model Young et al. (2003), will be used for comparison purposes when it is available. Another possibility is that a second thermal component with a plasma temperature lower than 30 MK is needed to fit the data below 10 keV. In other words, a multi-temperature bremsstrahlung model may be needed to fit the thermal component of the spectral data. In that case, the plasma temperature and emission measure I obtained would be for the higher-temperature component.

During the impulsive phase, all the flare spectra have a power-law component at high energies. One such spectrum is shown in Figure 5.1(b). Because of its steep power-law, if a very low cutoff energy (say 10 keV) is allowed, the flux contributed from the nonthermal, power-law component at low energies would be higher than that from the thermal component. However, the RHESSI images shown in Fig. 3.11 already suggested that the low-energy photon fluxes (<20 keV) are thermal since they come from a coronal source. Moreover, the smooth lightcurves at low energies (Fig. 5.2a) are also consistent with a thermal interpretation at those energies. Therefore, there must be a lower limit for the low-energy cutoff, below which the nonthermal thick-target bremsstrahlung would not dominate at low energies in the spectra.

To fit the spectra in the impulsive phase, I used a model consisting of both a thermal bremsstrahlung component and a nonthermal thick-target bremsstrahlung component. The nonthermal electrons have a single power-law distribution with a fixed low-energy

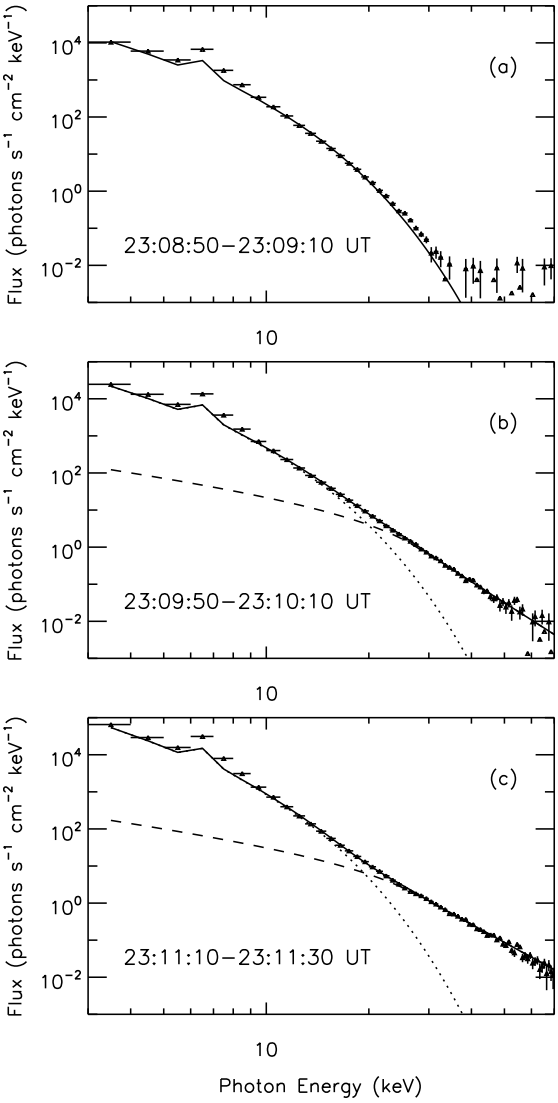

Figure 5.1: Three RHESSI spatially integrated spectra with background subtracted. *(a)*: spectrum in the time interval 23:08:50-23:09:10 UT (before the impulsive rise) fitted in the range 10-20 keV. *(b)*: spectrum at 23:09:50-23:10:10 UT (soon after the impulsive rise) fitted in the range 10-50 keV. *(c)*: spectrum at 23:11:10-23:11:30 UT (at the major peak of the flare) fitted in the range 10-50 keV. The plus signs with error bars represent spectral data. The lines represent model spectra fits: the dashed lines are for nonthermal thick-target bremsstrahlung (using f_vth_thick.pro)from a power-law electron spectrum with a low-energy cutoff; the dotted lines are for thermal bremsstrahlung (using mewe_kev.pro); the solid lines are the summations of the two.

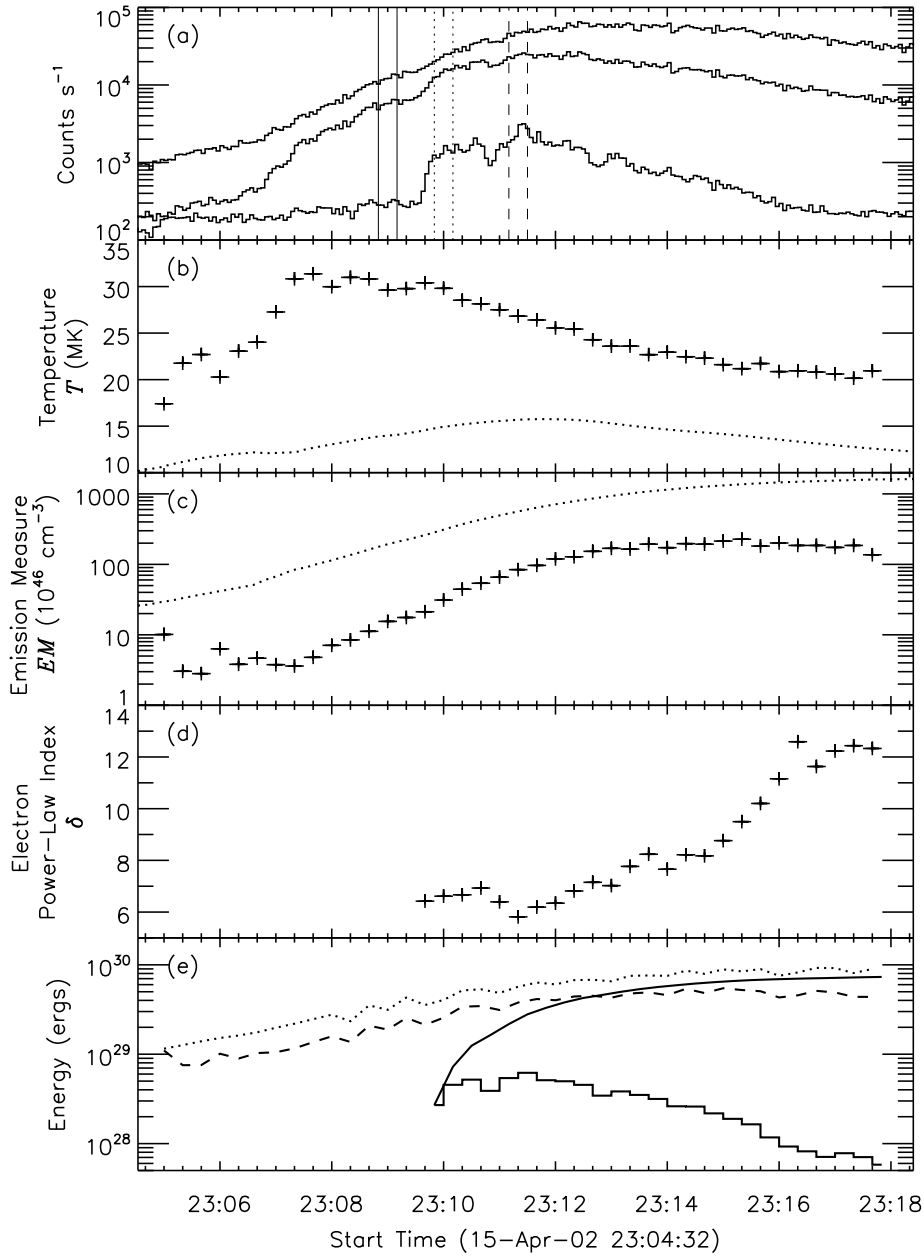

Figure 5.2: RHESSI spectral fitting results with a 28 keV electron low-energy cutoff. *(a)*: RHESSI light curves at energy bands (from top to bottom): 6-12, 12-25, and 25-50 keV. The scale factors are 2., 1. and 1., respectively. The three time intervals indicated in the plot are for the three spectra in Fig. 5.1. *(b)*: Plasma temperatures from RHESSI (plus signs) and GOES (dotted line). *(c)*: Plasma emission measures from RHESSI (plus signs) and GOES (dotted line). *(d)*: Electron power-law indices obtained with the thick-target bremsstrahlung model. *(e)*: Thermal plasma energy from RHESSI (dashed line) and GOES (dotted line). The solid line represents the accumulated nonthermal electron energy. The histogram represents the nonthermal electron energy deposited into a thick target in each time interval. All these fitting results are based on a low-energy cutoff of 28 keV in the electron spectrum of the nonthermal thick-target bremsstrahlung model.

cutoff. The determination of the low-energy cutoff has to ensure that the following three conditions are satisfied:

(1) The spectral fitting must give satisfactory values for the reduced chi-squared ($\sim$1).

(2) When the impulsive phase starts, the thermal parameters, i.e., temperature and emission measure, must not decrease suddenly. Therefore, the time profiles of thermal parameters must have a smooth and gradual evolution over the transition from the rise to the impulsive phase of the flare.

(3) Thermal emission must dominate at photon energies below 20 keV and nonthermal emission must dominate at energies above 25 keV (so as to be consistent with RHESSI images and lightcurves).

Figure 5.3 shows the time profiles of emission measure and temperature of the thermal plasma obtained from spectral fitting with different low-energy cutoffs. The thick solid lines indicate results for a 28 keV low-energy cutoff. The dotted lines are for low-energy cutoffs lower than 28 keV, and thin solid lines for low-energy cutoffs higher than 28 keV. In the rise phase, no nonthermal component was needed, and hence only an isothermal bremsstrahlung model was used with the best fit T and EM as shown. When the impulsive phase started at 23:09:40 UT, a nonthermal thick-target bremsstrahlung model was added to the isothermal bremsstrahlung function in order to fit the spectra.

To check the spectral fitting results with the three requirements listed above, I found:

(1) Spectra with low-energy cutoffs $\leq$30 keV give equally good values of reduced chi-squared ($\sim$1.0). The value of the reduced chi-squared increases when low-energy cutoffs increase, indicating that the fitting gets worse for low-energy cutoffs above 30 keV. For instance, spectral fitting with a 36 keV low-energy cutoff doubles the reduced chi-squared ($\sim$2.3) obtained with the $\leq$ 30 keV low-energy cutoffs. As pointed out in § 2.3, the reduced χ_r^2 is based on the 1σ statistical error and a 5% of systematic errors. Since the exact systematic error is unknown for RHESSI, the value of χ_r^2 can only be used for relative comparison purposes.

(2) From Figure 5.3, a low-energy cutoff at 28 ($\pm$2) keV gives a smooth time profile for both emission measure and temperature over the transition from the rise to the impulsive phase of the flare. The low-energy cutoffs of 22 and 24 keV cause a sudden decrease in temperature at the start time of the impulsive phase, which is improbable with the consideration of intensive energy release at that time. On the other hand, the low-energy cutoffs above 30 keV causes a sudden increase in temperature at the impulsive rise. This may be possible with consideration of the Neupert effect (Neupert, 1968; Dennis, 1993). However, these values of the low-energy cutoff cause a sudden decrease in emission measure, which is not likely. Simultaneous increases in both temperature and emission measure during the impulsive phases of flares have been seen before (e.g., Holman et al., 2003). I believe that this kind of sudden increase in temperature accompanied by a sudden decease in emission measure is solely caused by spectral fitting with an incorrect low-energy cutoff.

(3) The spectral fitting with this 28 ($\pm$2) keV low-energy cutoff (one such spectrum is shown in Fig.5.1b) indicates that the two thermal and nonthermal components are equal at $\sim$20 keV, below and above which the thermal and nonthermal component dominates, respectively. This is consistent with the RHESSI lightcurves and images. The RHESSI spectrum at the HXR peak (23:11:10–23:11:30 UT), fitted with the 28 keV low-energy cutoff, is shown Figure 5.1(c). Because the power-law nonthermal spectrum is hardest at

the HXR peak, a thermal component is clearly evident at low energies.

The time profiles of the spectral fitting parameters with the 28 keV low-energy cutoff are plotted in Figure 5.2. For comparison purposes, the GOES temperature and emission measure, obtained with the GOES Workbench in Solar Software, are also plotted. Because the GOES SXR instrument is more sensitive to lower temperature plasma than RHESSI, the plasma temperatures obtained from GOES are consistently lower than those from RHESSI, while the emission measures are larger. The current GOES Workbench also uses the Mewe atomic model (Mewe et al., 1985). Recently, White et al. (2004) found that the code using the Chianti atomic model (version 4.2, see Young et al., 2003) give temperatures of ∼1-2 MK higher and emission measures up to a factor 4 smaller compared to the results with the Mewe model. The time profile of the electron power-law index shown in Fig. 5.2(d) indicates a "hard-soft" pattern, rather than a typical "soft-hard-soft" pattern (e.g., Dennis, 1985). This may suggest that, because of the poor resolution of spectra before RHESSI, some thermal spectra could have been incorrectly interpreted as "soft" power-law spectra. I will pursue this subject in future studies.

5.3 Thermal and Nonthermal Energies

To calculate the total energy in the nonthermal electrons, I first obtained the nonthermal energy input at each time interval (the histogram in Fig. 5.2e) by integrating the power-law distribution of nonthermal electrons (above 28 keV). The resulting nonthermal energies are then accumulated in time (solid curve in Fig. 5.2e) to give a total of 7 (± 3) $\times 10^{29}$ ergs. The uncertainty estimation is based on the 2 keV uncertainty of the electron low-energy cutoff. Since the 28 keV low-energy cutoff for the nonthermal electrons was not arbitrarily selected, I believe that the nonthermal energy obtained here is more reliable than any previously obtained.

The thermal energy (Fig. 5.2e, dotted line for GOES, dashed line for RHESSI) is calculated using equation (5.1). The filling factor was set to 1, giving an upper limit to the thermal energy. The emission measure and temperature from GOES and RHESSI are given in § 5.2. The source volume at each time interval is estimated from the source area in the RHESSI images, similar to that used by Emslie et al. (2004), i.e., $V_{measured} = A^{3/2}$, where A is the area inside the 50% contour of the 10-20 keV image at each time interval. The images are obtained with the CLEAN algorithm using detectors from 3–9. Because of the low count rate, the image quality in the early rise phase (from 23:05 to 23:07:40 UT) is not good enough for the area estimation method. I set the area values before 23:08 UT to be the same as the area obtained from the image at 23:08 UT. Because GOES does not obtain images, the source volume for GOES-observed plasma is assumed to be the same as the volume obtained from RHESSI. The estimated source volume varies from 3000 to 6000 arcsec^3. The thermal energy of the flare is taken to be the peak value of the energy content of the thermal plasma. As indicated in Fig. 5.2(e), the peak thermal energy derived from GOES using a volume of ∼5500 arcsec^3 is $\sim 9 \times 10^{29}$ ergs at 23:18 UT, the end of the RHESSI observations, and 5.4 (± 0.3)$\times 10^{29}$ ergs (with a volume of 4500 arcsec^3) for RHESSI at 23:15:00 UT, 3 minutes before the GOES peak. This again supports the conclusion that RHESSI is seeing higher-temperature plasma. The error estimation for the

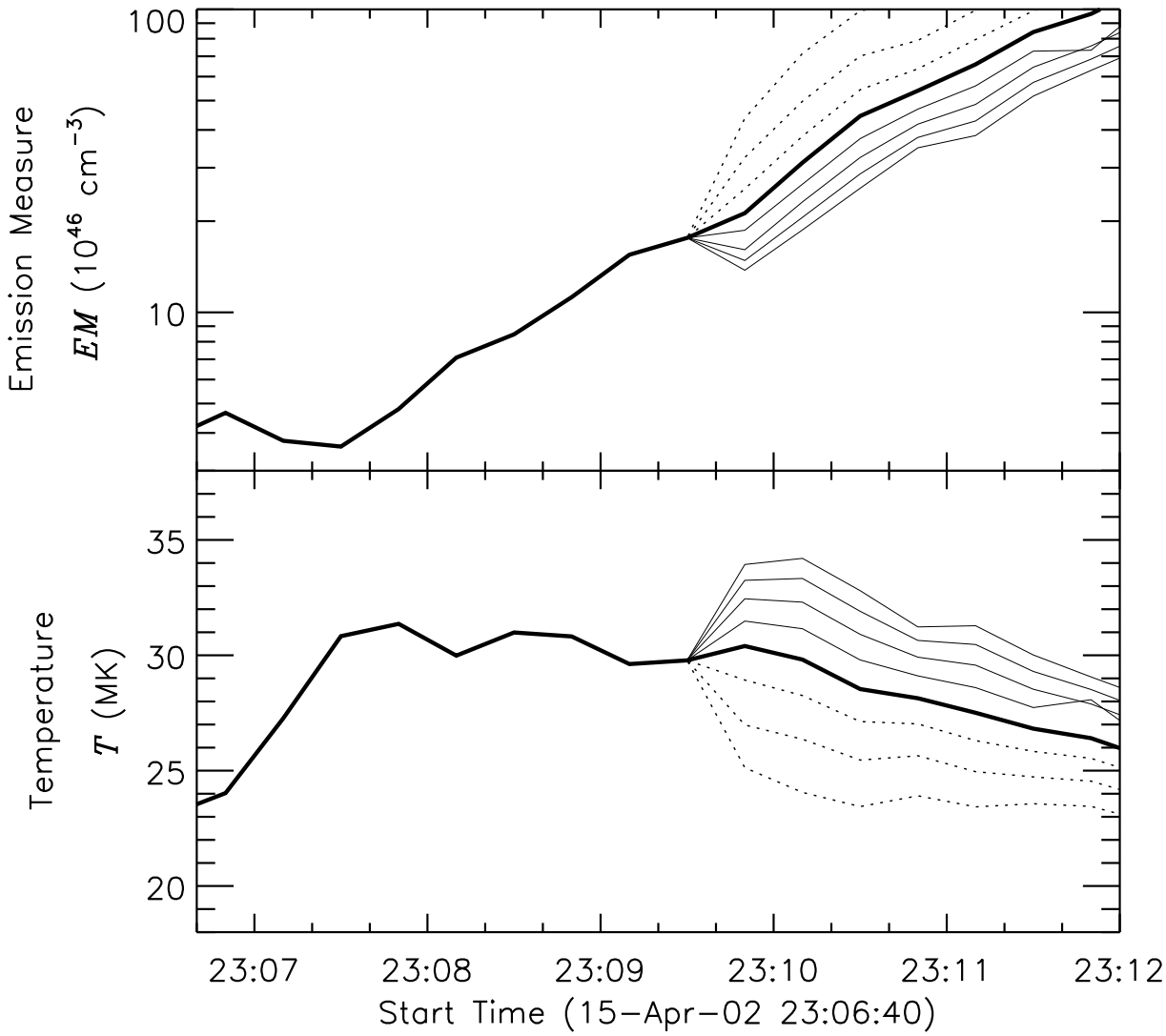

Figure 5.3: Time profiles of emission measure (*upper panel*) and temperature (*lower panel*) of the thermal plasma obtained from RHESSI spectral fitting with different electron low-energy cutoffs. During the rise phase of the flare (before 23:09:40 UT), only an isothermal bremsstrahlung model is used, so no low-energy cutoff is needed. In the impulsive phase, a thick-target bremsstrahlung component with different electron low-energy cutoffs is added to fit the spectra. In the upper panel, the lines represent the plasma emission measure obtained with electron low-energy cutoffs (from top to bottom) from 22 to 36 keV, in steps of 2 keV. In the lower panel, the lines represent the plasma temperature obtained with electron low-energy cutoffs (from top to bottom) from 36 to 22 keV, in steps of 2 keV. In both panels, the low-energy cutoff for the thick-solid lines is 28 keV.

thermal energy from RHESSI is based only on the uncertainties in the temperature and emission measure caused by the ±2 keV electron low-energy cutoff. It does not include the uncertainty in the estimation of the source volume or the filling factor. Consequently, the uncertainty in the thermal energy is still as large as one order of magnitude if the filling factor could be as small as 0.01. Evidently, the total nonthermal energy is comparable to the thermal energies estimated from both GOES and RHESSI, agreeing with the recent results of Holman et al. (2003) and Emslie et al. (2004). Because I do not account for thermal energy loss due to plasma cooling and any heating at later times, the obtained thermal energy is a lower limit. On the other hand, if the filling factor of the thermal plasma is less than 1, the thermal energy is over estimated.

5.4 Kinetic Energy of Associated CME

As discussed in § 3.2.1, this flare was associated with a CME observed with the LASCO C2 and C3 detectors (Fig. 3.10). Using the method proposed by Vourlidas et al. (2000), the mass of the ejected large coronal loop in Figure 3.10 is estimated to be 5.1×10^{10} grams. The mass uncertainty is about a factor of 2 for CMEs that are $\leq$ 40 degrees from the plane of the sky (Vourlidas et al., 2000). The projected velocity of the CME is ~300 km s^{-1}. Therefore, the kinetic energy is estimated to be $\sim 3 \times 10^{28}$ ergs.

Compared with the thermal energy of the plasma and the nonthermal energy in the accelerated electrons, the kinetic energy of the CME is about one order of magnitude less. This result is opposite to the results for the two big events analyzed by Emslie et al. (2004), and therefore supports the conclusion obtained by Hundhausen (1999) that flare intensities do not correlate well with CME kinetic energies.

5.5 Summary and Discussion

The electron low-energy cutoff is generally decided by the lower-energy limit of the spectrometer or set to some arbitrary value. This leads to a big uncertainty in estimating the total nonthermal energy in flares. In the flare on April 15, 2002 presented here, the low-energy cutoff, for the first time, is determined with an accuracy of ±2 keV from a combination of spectra, images, and lightcurves derived from RHESSI data alone.

Because the power-law spectra in the impulsive phase of the flare are steep, if the low-energy cutoff for the nonthermal electrons is assumed to be very low, the fluxes of the nonthermal power-law component would be as high as the thermal component at lower energies. This is contradictory to the fact that thermal emission appears to dominate at low energies (<20 keV) in RHESSI images and lightcurves. To ensure the dominance of the thermal flux at low energies and a smooth evolution of the thermal parameters (i.e., plasma temperature and emission measure) over the transition from the rise to the impulsive phase of the flare, I found the low-energy cutoff of the nonthermal electrons must be 28 (± 2) keV. As a result, the total energy in the nonthermal electrons is calculated to be 7 $(\pm3)\times10^{29}$ ergs, compared to the total thermal energy in hot plasma of $\sim 9 \times 10^{29}$ ergs from GOES, and 5.4 $(\pm0.3) \times 10^{29}$ ergs from RHESSI, in agreement

with recent findings (e.g., Holman et al., 2003; Emslie et al., 2004). Moreover, the kinetic energy of the flare-associated CME is found to be one order of magnitude less then the thermal and nonthermal energies in the flare, opposite to the findings of Emslie et al. (2004). This suggests that flare and CME energies are poorly correlated.

This event might be special because of its steep power-law spectrum. For many flares, the power-law component will not dominate over the thermal component at lower energies even for a low-energy cutoff as low as 1 keV. Therefore, the method I used to estimate the low-energy cutoff for this event may not be appropriate for all events. However, I did learn the following useful points from this analysis:

(1) Instead of fitting only one or a few spectra, we should fit multiple spectra throughout the flare to find the most reasonable model(s). In fact, some of the spectra during the impulsive phase of the flare can be fitted with just a single power-law function all the way down to 7 keV. However, this kind of fitting scenario is contradictory to the spectral fits in the rise phase, which indicate that the spectra at lower energies are thermal. In § 2.3, I have pointed out that multiple models could be used to fit the same RHESSI spectrum. Therefore, the difficulty is in determining the appropriate model(s). Certainly, fitting multiple spectra throughout the flare to check for consistency will offer some help. We can also try to utilize other sources of information, such as checking the effect of a low-energy electron cutoff on microwave spectra as proposed by Holman (2003), and checking plasma temperatures independently determined from the two iron line complexes at $\sim$6.7 and $\sim$8 keV in RHESSI spectra (Phillips, 2004).

(2) The spectral fitting results should be checked against RHESSI images for consistency. Usually the flare loops are due to thermal bremsstrahlung emission, and footpoints are due to nonthermal bremsstrahlung emission. However, we have to be careful in judging which sources are thermal or nonthermal in the RHESSI images. For instance, Holman et al. (2003) found that an extended coronal source in the rise phase of the 2002 July 23 X4.8 flare could not be fitted by an isothermal bremsstrahlung model. Instead, it could be fitted with a broken power-law model, leading to a nonthermal thick-target interpretation (Lin et al., 2003b). Veronig & Brown (2004) found that the HXR coronal sources (>25 keV) in the April 14-15 and April 15, 2002, flares analyzed in this thesis can be interpreted with nonthermal thick-target emissions. But they did not specify above what energies the emissions were nonthermal.

My preliminary spectral analysis of the other two homologous flares on 2002 April 14-15 and 16 indicates that they have the same characteristics as this event. Therefore, the techniques developed here will be applied to other events in future studies.

Chapter 6

Conclusions and Future work

6.1 Conclusions

The steady-state flare transport model has difficulty in explaining the spectrum of a HXR looptop source in a flare on 2002 February 20 (Chapter 2). With simulations, I have demonstrated that a transport model, in which accelerated electrons with a power-law energy distribution are injected steadily into a flare loop, could basically explain the existence of a HXR looptop source. However, the model-predicted looptop spectrum is steeper than that obtained from the observations. In order to produce a HXR looptop source with a flatter spectrum, a new model should allow a flatter electron spectrum than the transport model offers. One likely solution is that suprathermal electrons are accelerated in the looptop region, rather than injected into the loop after being accelerated above it (e.g., Aschwanden et al., 1996). Thus, the acceleration process will interfere with particle transport so that low-energy electrons escape from the looptop region faster than the current transport model predicts. As a result, the electron spectrum in the looptop region will be flatter.

The RHESSI observations of two flares on 2002 April 15 and 16 provide strong evidence for the existence of a large-scale current sheet above the flare loops (Chapter 3). The observations indicate that in both flares a coronal source separated from the underlying flare loop around the time of the HXR impulsive rise. Further analysis indicates that the temperature of the loop increased towards higher altitude, while the temperature of the coronal source increased towards lower altitude. In the April 15 flare, blob-like sources along the trajectory of the outward moving coronal source during the decay phase of the flare are consistent with magnetic islands initiated by the tearing-mode instability in a stretched current sheet. Finally, a cusp structure, which is expected to be located below a current sheet in MHD models, was seen in the microwave images of the April 15 flare. All of these observations strongly support the standard flare model (Carmichael, 1964; Sturrock, 1966; Hirayama, 1974; Kopp & Pneuman, 1976; Shibata et al., 1995; Forbes & Priest, 1995; Lin & Forbes, 2000).

RHESSI observations of the three homologous flares that occurred on 2002 April 14–16 share two new features (Chapter 4): (1) A separate coronal source up to $\sim 30''$ above the flare loop appeared in the early impulsive phase and stayed stationary for several minutes.

(2) Before the flare loop moved upward, as previously reported by others, the flare looptop centroid moved downward for 2-4 minutes during the early impulsive phase of the flare, falling by 13-30% of its initial height with a speed between 8 and 23 km s^{-1}. The loop downward motion may be a common feature of flares. These features are believed to be related to the formation or development of current sheet. However, they are not predicted in the standard flare model.

For the flare on 2002 April 15, a low-energy cutoff of 28 ($\pm$2) keV for the accelerated electrons was determined with greater certainty than any previously obtained (Chapter 5). This was achieved by the RHESSI spectroscopy capability together with the impulsive nature of the HXR light curve to separate the thermal and nonthermal sources. As a result, the nonthermal energy of the electrons is found to be comparable to the energy in the thermal plasma, and one order of magnitude larger than the kinetic energy of the associated CME. These results support previous conclusions (e.g., Saint-Hilaire & Benz, 2002; Holman et al., 2003; Emslie et al., 2004) that accelerated particles carry a large amount of the flare energy. Considering the recent results by Emslie et al. (2004) that the energies of the nonthermal electrons in two large flares are one order of magnitude smaller than the kinetic energies of the associated CMEs, the results from this event indicate that there may be no correlation between flare and CME energies.

6.2 Future work

6.2.1 Future Study on Modeling Flares

The detailed comparison of imaged spectra generated from the particle transport flare model with those determined from RHESSI observations has given us some preliminary results on particle acceleration and transport in flares. In order to extend this study, I plan to expand and revise the current model by including the following aspects:

(1) Application of the model to more events observed with RHESSI. In this thesis, I have applied the model to only one event showing a very weak HXR looptop source. There might be over 100 similar cases in the RHESSI event list. To further test the model, I will study more events that have HXR looptop sources shown in multiple energy bands so as to give reliable looptop imaged spectra.

(2) Consideration of other particle acceleration models. An acceleration model accounting for particle acceleration by turbulence in the flare looptop region has been proposed by Petrosian & Liu (2004). The model can vary the electron spectrum in the looptop region by adjusting the turbulent wave spectrum (see discussion in § 2.5). I plan to test this model against the observational data in future studies. I also plan to search for other flare models with similar capabilities.

(3) Expanding the geometry of flare loops. Currently, the model can be used only to simulate flares with semi-circular loops. The loop geometry in the model will be expanded to be more flexible, such as asymmetrical loop structure and asymmetrical footpoint size. Moreover, only a single loop is assumed in the current model. More realistic multiple loops (e.g., Hori et al., 1997, 1998; Reeves & Warren, 2002) will be explored in future studies.

One big challenge for the study of HXR looptop sources results from the difficulty of obtaining reliable imaging spectroscopy of looptop sources. Several factors can affect the quality of the imaging spectroscopy: (A) Limited image dynamic range. The image dynamic range can be affected by the number of counts in images, location of sidelobes and their amplitude, time variability of flux during the image intervals, knowledge of the grid transmission, number of harmonics used for image reconstruction (presently only the fundamental is used), and so forth. The current image dynamic range is ∼20:1 (Hurford et al., 2002). Due to this limited dynamic range, the HXR looptop source may appear in images in only one or two energy bands, giving inadequate looptop spectra. (B) Lack of knowledge of the uncertainties in the fluxes obtained from the RHESSI images. Without a correct estimation of uncertainties, it is very difficult to compare the model-predicted results with the observations effectively. In future study, I will explore solutions to these problems with help from the RHESSI team.

6.2.2 Future study of Magnetic Reconnection

The RHESSI observations in Chapters 3 and 4 offer a glimpse of the possibilities with the RHESSI observations for establishing magnetic reconnection as the basic process of flare energy release. The current standard flare model is successful in explaining many observations of flares. However, there are many other observations beyond the explanations of the standard model (see discussion in § 1.4). In this thesis, I have presented RHESSI observations predicted by the standard models as well as observations not predicted. Before looking for other new models, I plan to further test the standard models with RHESSI observations:

1. Verify the Reality of Weak Sources

The weak coronal sources above the flare loops are critical in establishing the existence of magnetic reconnection in current sheets above the magnetic loops visible in SXRs. From the previous observations with Yohkoh/SXT (Shibata et al., 1995; Ohyama & Shibata, 1998) and RHESSI observations presented in Chapter 3 and 4, it is known that the coronal sources or plasma blobs above the flare loops are usually weaker than the loops themselves. Because of the limited dynamic range of RHESSI reconstructed images, care has to be taken in interpreting such weak sources in the presence of the much stronger loop sources. I have indirectly verified the credibility of the weak sources by checking the consistency among the images made with different imaging algorithms at different time intervals and in difference energy bands, in order to directly improve the credibility of the weaker sources in RHESSI images. Nevertheless, the current dynamic range of the images has to be enhanced. Fortunately, members of the RHESSI team are making progress in this regard. For example, the flat-fielding algorithm has recently been improved (Hurford and Schmahl, private communication), with a resulting decrease in the frequency and intensity of artifacts in the RHESSI images.

RHESSI simulation software provides us with an alternative way to test the reality of weak sources. Similar to the simulations in Chapter 2, I can use either predicted X-ray flare images or real RHESSI images as input models for the simulation process, then

construct the model images with almost the same imaging parameters as those for the real RHESSI images, including the imaging algorithm, the aspect solution, data gaps (not implemented yet), and background. By comparing the input and output model images, I can estimate the dynamic range, identify false sources in the images, and detect other artifacts of the imaging process. My preliminary simulations indicate that the temperature distribution of the coronal source in the April 15, 2002 flare was not likely to have been caused by the imaging process itself. However, in the presence of a bright flare loop, the intensities of weak coronal sources were found to be lower than their true intensities by as much as 50% in images reconstructed using the CLEAN algorithm.

2. Search for Events With a Coronal Source Above the Flare Loops

I will search the RHESSI database for events with coronal X-ray sources above flare loops. Shibata et al. (1995) found that eight impulsive limb flares with compact loops selected from an unbiased sample showed faint X-ray plasma ejections above the SXR loop. All the flares in their data set were between GOES class M2 and M8. The three homologues flares I analyzed were also M-class flares (i.e., M3.7, M1.2, and M2.5). To reduce the size of the database, I will set some specific criteria for flare selection in the RHESSI database. Initially, I will investigate only M-class limb flares with significant HXR fluxes above 25 keV in the impulsive phase. I also plan to broaden the flare selection criteria to study flares on the solar disk. RHESSI flares of other GOES classes, such as C or X flares, will be examined after this initial study.

To look for possible magnetic islands in current sheets, I will search for the blob-like sources similar to those shown in Figure 3.15. With improvements in the dynamic range of the RHESSI images, I will be able to identify these weak sources with greater confidence, and learn more about their frequency of appearance and lifetime.

3. Statistical Study of the Downward Motion of the Looptop Centroid

The observation of the downward motion of the looptop centroid is not predicted by any of the standard models of solar flares. Therefore, study of this feature will be beneficial in refining the current models or in creating a new model.

I will first determine how common this feature is by investigating more flares in the RHESSI database. I will establish an unbiased sample including flares having multiple spikes in the impulsive phase (usually lasting several to more than 10 min), flares having just a single spike in the impulsive phase, and gradual, long-duration events. The speed, start time, and altitude decrease of the downward motion of the looptop centroid in different energy bands will be investigated for all flare types. I will search for flares from different active regions and at different locations on the solar disk to differentiate between vertical and horizontal motion on a statistical basis.

I will study the timing of when the looptop centroid changes from downward to upward motion. Among the three homologous flares I have studied, the turnover time of the looptop centroid occurred soon after the major peak of the two flares (i.e., the April 15 and April 16 flares; the April 14-15 flare did not have an obvious major peak). Is this timing a coincidence? If not, then the downward motion is closely related to the energy

release process and is most likely associated with the formation and early development of the current sheet.

4. Statistical Study the Correlation Between the Loop Rise Speed and the HXR Flux

The correlation between the loop rise speed and the HXR flux in the April 14-15 flare implies that the faster the magnetic reconnection rate, the higher the flux of accelerated electrons. This observation supports the standard reconnection scenario. However, such an important model prediction needs more thorough observational scrutiny.

I will first establish a method for determining the uncertainty in the position of the source centroid in RHESSI images so that I can assess the significance of small displacements. Currently, there is no way to accurately determine the uncertainty in RHESSI source centroids.

I will then investigate RHESSI flares for this correlation. Flares showing clear-cut loops and having multiple spikes in the impulsive phase will be preferably selected for this study. In particular, I will determine the time delay between the increase in the upward speed of the looptop source and the rise in the HXR flux, and then check whether or not the delays are consistent with the time scale of chromospheric evaporation. In well-observed flares, I will also compute the evolution of the energy in accelerated electrons and in the hot thermal plasma, and compare these with the evolution of the looptop centroid and, when possible, with the separation between the loop footpoints. On the other hand, a recent study of a flare by Ji et al. (2004) indicates that some flares may show a decrease in the height of the looptop centroid with the rise of the X-ray flux in individual spikes, as in the primary rise phase of the April flares. I hope to clarify and better understand these disparate observational results.

5. Search for Features Predicted by Flare Models

Previous observations in X-rays have shown that a typical flare has a compact SXR loop or an arcade of loops, with HXR emission at their footpoints and, in some cases, above their summits. However, there are other weak sources or less common features that are observed, such as the plasma blob above the loops (Shibata et al., 1995; Ohyama & Shibata, 1998) and supra-arcade downflows (McKenzie & Hudson, 1999). Some of these features can be very helpful in distinguishing between models. As reported by Uchida (1996), careful study of the February 21, 1992, flare, which showed a "candle-flame" shape of X-ray loops with a dark tunnel below and was claimed as excellent support for the classic bipolar model (Tsuneta et al., 1992), revealed that there is a vertical partition-like bright feature in the middle of the tunnel below the arcade. Furthermore, in the pre-flare stage there existed a large loop connecting to the top of the preflare "core". These new features support the quadrupolar model (Uchida et al., 1999; Hirose et al., 2001) instead of the simpler bipolar model.

The break-out model (Antiochos, 1998; Antiochos, Devore, & Klimchuk, 1999) also involves a quadrupolar magnetic topology, with the inclusion of a horizontal current sheet high in the corona where magnetic reconnection allows the escape of the underlying "plas-

moid". The structure of the plasmoid and the underlying flare loops is similar to that of the dipole model, but signatures of electron acceleration in the upper current sheet may be observable, most likely as weak X-ray emission from the outer magnetic poles or footpoints. Extended, weak thermal emission in the corona may also be observable. I will search for these sources.

Besides RHESSI, observations in other wavelengths, such as Hα, EUV, and radio will also be used. Flare models not only differ from each other during the energy release process (when emissions in X-rays are prominent), but also (maybe more importantly) differ in the energy build-up and initiation process when the signatures in X-rays are weak or absent, but the signatures in Hα or EUV may be abundant. For instance, filament eruptions often observed in Hα or EUV before flares and/or CMEs, which are believed to be the trigger of the events (e.g., Uchida et al., 1999; Hirose et al., 2001), cannot be observed with RHESSI. Moreover, RHESSI was not designed to provide images with the kind of morphological richness and detail that we have come to appreciate from TRACE, SOHO/EIT and other direct-imaging instruments (Hurford et al., 2002). Therefore, observations in other wavelengths will yield a more complete picture of a flare.

6.2.3 Future Studies of the Low-Energy Cutoff and Flare Energetics

With the broad energy coverage (3 keV – 17 MeV) and excellent energy resolution of RHESSI spectra, we still cannot determine the low-energy cutoff of nonthermal electrons in general. The low energy range of a spatially-integrated flare spectrum is always dominated by thermal bremsstrahlung. Therefore, the spectral flattening due to the low-energy cutoff will be covered up by this thermal component. For flares with abundant emission from the footpoints, theoretically, we can use the footpoint spectra to determine the low-energy cutoff, because most of the nonthermal emissions are produced at the footpoints. Because there is not much thermal emission at the footpoints, we should be able to see spectral flattening at low energies. Unfortunately, the low energy ranges of footpoint spectra usually are still dominated by thermal fluxes contributed from the contamination of strong coronal thermal sources in the same field of view. In order to solve the problem, I need to explore ways to subtract the contaminated thermal fluxes from the footpoint spectrum.

As demonstrated in this thesis, the study of low-energy cutoffs and flare energetics heavily depends on RHESSI spectral fitting. However, currently, RHESSI spectral fitting suffers from the following problems:

(1) Despite the fact that RHESSI can provide spectra to energies as low as 3 keV, it has proven to be very difficult to obtain accurate spectra at energies below $\sim$8 keV when the RHESSI thin attenuators are in or below $\sim$15 keV when both the thin and thick attenuators are in. This is mainly caused by our imperfect knowledge of the strong attenuation of the incident photon flux at these energies by the material between the detectors and the Sun, including the attenuators when they are in place. At energies below $\sim$5 keV, the counts from photons with these energies are strongly reduced by the RHESSI attenuators (with fractional transmission as low as 10^{-8}). The measured count-

rate spectrum is dominated by non-photopeak counts created when a >11 keV photon is photoelectrically absorbed in a germanium detector but the K-shell fluorescence photon (10 keV) escapes (Smith et al., 2002). Therefore, the incident photon spectrum below 5 or 6 keV is impossible to obtain with the attenuators in place.

(2) Difficulties in determining the correct background spectrum. Before analyzing the spectral data, we have to identify and subtract the background spectrum (Smith et al., 2002). When the flare duration is short (∼tens of minutes), this can be done by selecting data intervals just before and/or after the flare and subtracting the spectra in those intervals from the spectrum at the time of interest. But for a long-lasting flare, this can be inaccurate because the background can vary significantly over tens of minutes. Although there have been several ways proposed to handle the background subtractions (Smith et al., 2002), it is still difficult to determine the correct count-rate spectrum. This is especially important for energies at which the flare count rate is less than an order of magnitude above the non-flare rates, usually at the higher energies.

(3) Nonuniform target ionization. In the thick-target bremsstrahlung model used in Chapter 2, the plasma along the thick-target beam electron paths is assumed to be uniformly ionized. In fact, the ionization fraction decreases when the plasma temperature decreases in the lower solar atmosphere. The decrease of ionization with depth enhances the HXR bremsstrahlung efficiency, elevating the HXR spectrum by factors of up to 2.8 above that for a fully ionized target (Kontar, Brown & Mcarthur, 2002, and references therein). The nonuniform ionization produces a local spectral hardening around the photon energy which equals the minimum electron energy required to reach the near-neutral chromospheric layers of the flare. Therefore, the nonunifrom ionization effect has to be included in interpreting RHESSI spectra. However, it is still unclear to what extent it affects the spectra. Kontar, Brown & Mcarthur (2002) and Kontar et al. (2003) found that the nonthermal parts of RHESSI spectra in the five flares they analyzed deviated from a single power-law form, and the fit to the spectra is improved when the nonuniform ionization effect was taken into account.

(4) Albedo, or the Compton backscatter of the primary HXR flux. As summarized by Alexander & Brown (2002), deka-keV photons emitted downwards in the optically thin solar atmosphere undergo Compton backscatter in the low atmosphere and add to the total observed photon fluxes. These backscattered photons make a significant contribution to the observed HXR spectral fluxes over the RHESSI energy range. Alexander & Brown (2002) pointed out that the full correction of the albedo effect is nonlinear and "messy". With a first-order correction, they found that the albedo effect can produce "bulges" in the 30–100 keV range in both thin- and thick-target bremsstrahlung spectra, especially when the photon spectra are hard (power-law index of 2∼3). Although such "bulges" have never been reported in RHESSI spectra, this does not mean the albedo effect should not be included in the interpretation of the RHESSI data. The downward 'knees' often seen in RHESSI spectra in the deka-keV range (e.g., Kontar, Brown & Mcarthur, 2002) could be the middle and upper end of the bulges caused by the albedo. Moreover, the nonuniform ionization effect discussed above may counter the albedo effect in RHESSI spectra in some cases (Alexander & Brown, 2002).

(5) The forward-fitting method used by SPEX (Smith et al., 2002) has some limitations. When using the forward-fitting method, the user first specifies a model for the flare

spectrum, the software then multiplies this spectrum by the full 2-dimensional instrument response matrix, checks the goodness of fit to the observed count spectrum based on the reduced χ_r^2, and repeats the process, varying the parameters of the input model until the best fit is found. The obvious limitation of the method is that a model with a limited number of parameters has to be assumed before fitting the data. This assumed model will certainly restrict the interpretation of spectral data. Moreover, this forward-fitting technique has two other "potentially serious" problems (Fenimore et al., 1983; Loredo & Epstein, 1989). First, the photon spectrum obtained from the spectral fitting process is not unique. Two different model spectra may result in the same count spectra. This has been demonstrated in § 2.3 that different models could fit the same RHESSI spectrum of the flare on 2002 February 20. Second, the data points plotted for the photon spectra are variable because they depend on the mapping process from count spectrum to photon spectrum, which in turn depends on how well the model spectra fitted the observed count spectra over the full energy range. Fenimore et al. (1983) pointed out that the two problems combine to cause the data points to change their positions in the observed photon spectra to move toward the model-predicted spectra.

Another method currently being studied is to infer the electron spectrum by direct inversion of the photon spectrum (e.g., Piana et al., 2003). This inversion technique will avoid some of the problems with the forward-fitting method. Moreover, the inversion method does not assume any model, so we may get some features not accessible with the forward-fitting method (Piana et al., 2003). However, there are some disadvantages for the inversion method. For instance, in order to avoid amplifying data noise, photon spectra usually need to be smoothed during the inversion. The interpretation of new features in the inferred electron spectrum is sometimes difficult because of concerns of authenticity and lack of clear physical meaning. Therefore, at present, both forward-fitting and inversion methods should be used together for comparison purposes.

In addition, obtaining photon spectra of high accuracy also depends on knowledge of several other instrument-related factors, e.g., pulse pileup (Smith et al., 2002). Currently, intensive studies of these problems are being conducted by the RHESSI team and other people. I plan to investigate these problems in my future analysis of RHESSI spectra.

Bibliography

Alexander, D., & Metcalf, T. 1997, ApJ, 489, 442

Alexander, R. C., & Brown, J. C. 2002, Sol. Phys., 210, 407

Antiochos, S. K. 1998, ApJ, 502, 181

Antiochos, S. K., Devore, C. R., Klimchuk, J. A. 1999, ApJ, 510, 485

Antonucci, E., Dodero, M. A., & Martin, R. 1990, ApJ, Sup., 73, 147

Aschwanden, M. J., Hudson, H., Kosugi, T., & Schwartz, R. A. 1996, ApJ, 464, 985

Aschwanden, M. et al. 1995, ApJ, 455, 347

Aschwanden, M. J. 2002, Particle Acceleration and Kinematics in Solar Flares, Kluwer Academic Publishers

Aschwanden, M. J., Schmahl, E., the RHESSI Team, 2002, Sol. Phys., 210, 193

Aschwanden, M. J., Metcalf, T. R., Krucker, S.; Sato, J.; Conway, A. J.; Hurford, G. J., Schmahl, E. J. 2004, Sol. Phys. 219, 149

Aschwanden, M. J. 2004, Physics Of The Solar Corona, Praxis Publishing Ltd.

Benka, S. G., & Holman, G. D. 1992, ApJ, 391, 854

Benz, A., & Aschwanden, M. J. 1991, in Eruptive Solar Flares, eds. Svestka, Z., Jackson, B. V., & Machado, M. E., Vol 399 of LNP, p. 106

Brown, J. C. 1971, Sol. Phys., 18, 489

Brown, J. C. 1974. in Jr G. A. Newkirk (ed), Coronal Disturbances, IAU Symp. 57: 105

Brown, J. C., & Emslie, A. G. 1987, Sol. Phys., 110, 305

Bruzek, A. 1964, ApJ, 140, 746

Canfield, R. C., et al. 1996, ApJ, 462, 1016

Cargill, P. J., & Klimchuk, J. A. 1997, ApJ, 478, 799

Carmichael, H. 1964, In The Physics of Solar Flares, ed. W. N. Hess (NASA SP-50, Washington, DC:NASA), 451

Carreras, B. A., Hicks, H. R., Homes, J. A., & Waddell, B. V. 1980, Phys. Fluids, 23, 1811.

Christe, S., Krucker, S., Arzner, K., & Lin, R. P. 2003, Bulletin of the American Astronomical Society, 35 #3

Ciaravella, A., Raymond, J. C., Li, J., Reiser, P., Gardner, L. D., Ko, Y.-K., & Fineschi, S. 2002, ApJ, 575, 1116

Cheng, C. C. 1977, ApJ, 213, 558

Dennis, B. R. 1985, Sol. Phys., 100, 465

Dennis, B. R. 1988, Sol. Phys., 118, 49

Dennis, B. R., & Zarro, D. M. 1993, Sol. Phys., 146, 177

Dennis, B. R., Veronig, A., Schwartz, R. A., Sui, L., Tolbert, A. K., Zarro, D. M., and the RHESSI Team 2003, Adv. Space Res., Vol. 32, No. 12, 2459

Doschek, G. 1994, in Proc. Kofu Symp., A New Look at the Sun with Emphasis on Advance Observations of Coronal Dynamics and Flares, ed. S. Enome & T. Hirayama, NRO Report (Nobeyama Japan), 360

Dungey, J.W. 1953, Conditions for the occurrence of electrical discharges in astrophysical systems, Phil. Mag., 44, 725

Emslie, A. G., & Brown, J. C., 1980, ApJ, 237, 1015

Emslie, A. G. 2003, ApJ, 595, L119

Emslie, A. G. et al. 2004, J. Geophys. Res., 109, A10104

Fenimore, E. F., Klebesadel, R. W., & Laros, J. G. 1983, Adv. Space Res., 3, 207

Fletcher, L., A&A, 303, L9

Fletcher, L., & Martens, P. C. H. 1998, ApJ, 505, 418

Fletcher, L., & Hudson, H. S. 2002, Sol. Phys., 210, 307

Forbes, T. G., & Priest, E. R. 1984, Reconnection in solar flares. In: Butler, D.M., Papadopoulous, K. (Eds), Solar Terrestrial Physics: Present and Future, NASA, pp. 1-35.

Forbes, T. G., & Priest, E. R. 1995, ApJ, 446, 377

Forbes, T. G., & Acton, T. W. 1996, ApJ, 459, 330

Forbes, T. G., & Lin, J. 2000, J. of Atmos. and Sol.-Terr. Phys., 62, 1499

Furth, H. P., Killeen, J., & Rosenbluth, M. N. 1963, Finite-resistivity instabilities of a sheet pinch, Phys. Fluids, 6, 459

Gallagher, P. T., Dennis, B. R., Krucker, S., Schwartz, R. A., & Tolbert, A. K. 2002, Sol. Phys., 210, 341

Gan, W. Q. 2001, ApJ, 552, 858

Gan, W. Q., Li, Y. P., Chang, J., McTiernan, James M., 2002, Sol. Phys., 207, 137

Garcia, H. 1994, Sol. Phys., 154, 275

Gosling, J. T., Birn, J., & Hesse, M., Geophys. Res. L., 1995, 22, 869

Haug, E. 1997, Astron. Astrophys., 326, 417

Heyvaerts, J., Priest, E. R., and Rust, D. M. 1977, ApJ 216, 123

Hirayama, T. 1974, Sol. Phys., 34, 323

Hirose, S., Uchida, T., Uemura, S., Yamaguchi T., & Cable, S.B. 2001, ApJ, 551, 586

Holman, G. D. 1985, 293, 584

Holman, G. D., & Benka, S. G. 1992, ApJ, 400, L79

Holman, G. D. 1996, BAAS, 28, 939. Also see results at: http://hesperia.gsfc.nasa.gov/sftheory/loop.htm

Holman, G. D. 2003, ApJ, 586, 606

Holman, G. D., Sui, L., Schwartz, R. A., Emslie, A. G. 2003, ApJ, 595, L97

Hood, A.W., & Priest, E.R. 1979, Sol. Phys., 64, 303

Hori, K., Yokoyama, T., Kosugi, T., & Shibata, K. 1997, 489, 426

Hori, K., Yokoyama, T., Kosugi, T., & Shibata, K. 1998, 500, 492

Hudson, H. S. 1972, Sol. Phys., 24, 414

Hudson, H. S. 2000, ApJ, 531, L75

Hudson, H. S., & Ryan, J. 1995, Annu. Rev. Astron. Astrophys., 33, 239

Hundhausen A. J., 1999, Coronal Mass Ejections, AGU Geophysical Monograph 99, Eds: Nancy Crooker, Jo Ann Joselyn, Joan Feynman, P1-7

Hurford, G. J., et al. 2002, Sol. Phys., 210, 61

Hurford, G. J., Schwartz, R. A., Krucker, S., Lin, R. P., Smith, D. M., & Vilmer, N. 2003, ApJ, 595, L77

Ji, H., Wang, H., Goode, P. R., Jiang, Y., & Yurchyshyn, V. 2004, ApJ, 607, L55

Kasparova, J., Karlicky M., Schwartz, R. A., & Dennis, B. R. 2004, submitted to Solar Phys.

Ko, Y.-K., Raymond, J.C, Lin, J., Lawrence G., Li, J., Fludra, A. 2003, ApJ, 594, 1068

Kopp, R. A., & Pneuman, G. W. 1976, Sol. Phys., 50, 85

Kontar, E. P., Brown, J. C., & Mcarthur, G. K. 2002, Sol. Phys., 210, 419

Kontar, E. P., Brown, J. C., Emslie, A. G., Schwartz, R. A., Smith, D. M., & Alexander, R. C. 2003, ApJ, 595, L123,

Krucker, S., Hurford, G. J., Lin, R.P. 2003, ApJ, 595, L103

Kulsrud, R. M. 2001, Earth, Planets and Space, 53, 417

Lin, J., Forbes, T.G., Priest, E. R., & Bungey, T.N. 1995, Sol. Phys., 159, 275

Lin, J., & Forbes, T.G. 2000, J. Geophys. Res., 105, 2375

Lin, J. 2002, Chinese J. Astron. Astrophys., 2, 539

Lin, J. 2004, Sol. Phys., in press

Lin, J., Ko, Y.-K., Sui, L., Raymond, J. C., Stenborg, G. A., Jiang, Y., Zhao, S., & Mancuso, S. 2005, ApJ, in press

Lin, R. P., & Hudson, H. S. 1976, Sol. Phys., 50, 153

Lin, R.P., & Schwartz, R. A. 1987, ApJ, 312, 462

Lin, R. P., et al. 2002, Sol. Phys., 210, 3

Lin, R. P., et al. 2003a, ApJ, 595, L69

Lin, R. P., Krucker, S., Holman, G. D., Sui, L., Hurford, G. J., and Schwartz, R. A. 2003b, Proceedings of the 28th International Cosmic Ray Conference, University Academy Press, Kajita, T. et al. (Eds.), P. 3207-3210

Liu, W., Jiang, Y., Liu, S., & Petrosian, V. 2004, ApJ, 611, L53

Loredo, T. J., & Epstein, R. I., 1989, ApJ, 336, 896

Martens, P. C. H. 2003, Advances in Space Research, 32, 905

Masuda, S., Kosugi, T., Hara, H., Tsuneta, S., & Ogawara, Y. 1994, Nature, 371, 495

Masuda, S., Kosugi, T., Hara, H., Sakao, T., Shibata, K., & Tsuneta, S. 1995, Publ. Astron. Soc. Japan, 47, 677

Mewe, R., Gronenschild, E. H. B. M., van den Oord, G. H. J. 1985, Astro. & Astrophys. Suppl. Series, 62, 197-254

McTiernan, J. M., & Petrosian, V. 1990, ApJ, 359, 524

McKenzie, D.E. 2002, in Multi-Wavelength Observations of Coronal Structure and Dynamics, ed. Martens, P.C.H., Cauffman, D.P., 155

McKenzie, D. E., Hudson, H. S. 1999, ApJ, 519, L93

Miller, J. A., Emslie, G. A., Holman, G. D., Cargill, P. J., Dennis, B. R., LaRosa, T. N., Winglee, R. M., Benka, S. G., & Tsuneta, S. 1997, J. Geophys. Res., 102, 14631

Moore, R., McKenzie, D.L., Švestka, Z., Widing, K.G., & 12 co-authors 1980, in P.A. Sturrock (ed), Solar Flares, A Monograph from Skylab Solar Workshop II, p. 341

Moore, R.L., & Roumeliotis, G. 1992, in Eruptive Solar Flares, (Z. Svestka, G.V. Jackson, M.E. Machaodo, eds.), Lecture Notes in Physics, 399, 69

Neupert, W. M. 1968, ApJ, 153, L59

Nishio, M., Yaji, K., Kosugi, T., Nakajima, H., & Sakurai, T. 1997, ApJ, 489, 976

Nitta, N. V., Sato, J., Hudson, H.S. 2001, ApJ, 552, 821

Ohyama, M., & Shibata, K. 1998, ApJ, 499, 934

Parker, E. N. 1957, J. Geophys. Rev., 62, 509

Petrosian, V., & Liu, S. 2004, ApJ, 610, 550

Petrosian, V., Donaghy, T. Q.,& McTiernan, J. M. 2002, ApJ, 569, 459

Petschek, H. E. 1964, Magnetic field annihilation, in Physics of Solar Flares, ed. W. N. Hess (NASA SP-50, Washington, DC) pp. 425-439

Phillips, K. J. H. 1992, Guide to the Sun, Cambridge University Press

Phillips, K. J. H. 2004, ApJ, 605, 921

Phillips, K. J. H., Bhatia, A. K., Mason, H. E., & Zarro, D. M. 1996, ApJ, 466, 549

Piana, M., Massone, A. M., Kontar, E. P., Emsile, A. G., Brown, J. C., & Schwartz, R. A. 2003, ApJ, 595, L127

Porter, L. J., & Klimchuk, J. A. 1995, ApJ, 454, 499

Priest, E. R., & Forbes, T. G. 1990, Magnetic Reconnection: MHD Theory and Applications, Cambridge University Press, Cambridge, UK

Priest, E. R., & Forbes, T. G. 2000, Magnetic Reconnection, MHD Theory and Applications, Cambridge University Press, second edition, Cambridge, UK

Priest, E., & Forbes, T. 2002, Astron. Astrophys. Rev., 10, 313

Qiu, J., Wang, H., Cheng, C. Z., Gary, D. E., 2003, ApJ, 604, 900

Ramaty, R., Manzhavidze, N., Kozlovsky, B., & Murphy, R. 1995, ApJ, 455, L193

Reeves, K. K., Warren, H. P. 2002, ApJ, 578, 590

Sakao, T., Kosugi, T., & Masuda, S. 1998, in ASSL Vol. 229, Observational Plasma Astrophysics: Five Years of Yohkoh and Beyond, ed. T. Watanabe, T. Kosugi, & A. C. Sterling (Boston: Kluwer), 273

Sakao, T. 1994, Ph.D. thesis (University of Tokyo), Characteristics of solar flare hard X-ray sources as revealed with the Hard X-ray Telescope aboard the Yohkoh satellite.

Sakai, J. & de Jager, C. 1991, Sol. Phys., 134, 329

Saint-Hilaire, P., & Benz, A. O. 2002, Sol. Phys., 210, 287

Sato, J., Kosugi, T., and Makishima, K. 1999, Publ. of the Astronomical Society of Japan, 51, 127

Schmahl, E. J., & Hurford, G. J. 2002, Sol. Phys., 210, 273

Shibata, K., et al. 1992, ApJ, 44, L173

Shibata, K., Masuda, S., Shimojo, M., Hara, H., Yokoyama, T., Tsuneta, S., Kosugi, T., & Ogawara, Y. 1995, ApJ, 451, 83

Shibata, K. 1999, AP&SS, 264, 129

Shimojo, M., Shibata, K. 2000, ApJ, 542, 1100

Shimojo, M., Hashimoto, S., Shibata, K., Hirayama, Y., Hudson, H. S., & Acton, L. W. 1996, PASJ, 48, 123

Smith, D. M., et al. 2002, Sol. Phys., 210, 33

Spitzer, L. 1962, Physics of Fully Ionized Gases, 2nd edn, Interscience, New York

Strong, K. T., Harvey, K. L., Hirayama, T., Nitta, N., Shimizu, T. & Tsuneta, S. 1992, PASJ, 44, L161

Sturrock, P. A. 1966, Nature, 211, 695

Sturrock, P. A. 1987, Rapid Fluctuations in Solar Flars, eds. Dennis, B. R., Orwig, L. E. & Kiplinger A. L., p1

Sui, L., Holman, G. D., & Dennis, B. R. 2004, ApJ, 612, 546

Sui, L., Holman, G. D., White, S. M., & Zhang, J. 2005, ApJ, in prepration

Švestka, Z., Fontenla, J. M., Machado, M. E., Martin, S. T., Neidig, D. F. and Poletto, G. 1987, Sol. Phys., 169, 403

Švestka, Z. 1996, Sol. Phys., 108, 237

Sweet, P. A. 1958, The production of high-energy particles in solar flares, Nuovo Cimento Suppl. 8, Ser. X, 188-196.

Syrovatskii, S. I. 1971, Soviet Phys.-JETP lett., 33, 933

Syrovatskii, S. I. 1972, Critical problems of magnetospheric physics. In Dyer, E., editor, Solar Terrestrial Physics, p119. National Academy of Sciences

Tandberg-Hanssen, E., & Emsilie A. G. 1988, the Physics of Solar Flares, Cambridge University Press

Thomas, R. J., Crannell, C. J., and Starr, R. 1985, Sol. Phys., 95, 323

Tsuneta, S. 1996, ApJ, 456, 840

Tsuneta, S., Hara, H., Shimizu, T., Acton, L.W., Strong, K.T., Hudson, H.S., & Ogawara, Y. 1992, PASJ, 44, 63

Tsuneta, S., Masuda, A., Kosugi, T., & Sato, J. 1997, ApJ, 478, 787

Uchida, Y. 1996, Advances in Space Research, 17, 19

Uchida, Y., et al. 1999, AP&SS, 264, 145

Veronig, A. M., Brown, J. C. 2004, ApJ, 603, L117

Vilmer, N., MacKinnon, A. L. 2002, in Energy Conversion and Particle Acceleration in the Solar Corona, Ed. by Karl-Ludwig Klein, p.127

Vourlidas, A., Subramanian P., Dere, K. P., & Howard, R. A. 2000, ApJ, 534, 456

Wang, H., Spirock, T. J., Qiu, J., Ji, H., Yurchyshyn, V., Moon, Y., Denker, C., & Goode, P. R., 2002, ApJ, 576, 497

Webb, D. F., Burkepile, J., Forbes, T. G., & Riley P. 2003, J. Geophys. Rev., V108, Issue A12, pp. SSH 6-1

Wheatland, M. S., & Melrose, D. B. 1995, Sol. Phys., 158, 283

White, S. M., Krucker, S., Shibasaki, K., Yokoyama, T., Shimojo, M., & Kundu, M. R. 2003, 595, L111

White, S. M., Thomas, R. J., Schwartz, R. A. 2004, submitted to Solar Phys.

Winglee, R. M. et al. 1991, ApJ, 375, 366

Young, P. R., Del Zanna, G., Landi, E., Dere, K. P., Mason, H. E., Landini, M. 2003, Astro. J. Suppl. Series, 144, 135-152

Yokoyama, T., & Shibata, K. 1995, Nature, 375, 42

Yokoyama T., Akita, K., Morimoto, T., Inoue, K., & Newmark, J. 2001, ApJ, 546, 69

Zirin, H. 1988, Astrophysics of the Sun, Cambridge University Press